Monthly Notices
of the
ROYAL ASTRONOMICAL SOCIETY

MNRAS **536,** 988–1016 (2025) https://doi.org/10.1093/mnras/stae2633
Advance Access publication 2024 November 26

Elevated UV luminosity density at Cosmic Dawn explained by non-evolving, weakly mass-dependent star formation efficiency

Robert Feldmann ,[1]★ Michael Boylan-Kolchin ,[2] James S. Bullock ,[3] Onur Çatmabacak ,[1] Claude-André Faucher-Giguère ,[4] Christopher C. Hayward ,[5] Dušan Kereš,[6] Alexandres Lazar ,[3] Lichen Liang ,[7] Jorge Moreno ,[8,9] Pascal A. Oesch ,[10,11] Eliot Quataert ,[12] Xuejian Shen [13] and Guochao Sun [4]

[1] *Department of Astrophysics, University of Zurich, Zurich CH-8057, Switzerland*
[2] *Department of Astronomy, The University of Texas at Austin, 2515 Speedway Stop C1400, Austin, TX 78712, USA*
[3] *Department of Physics and Astronomy, University of California, Irvine, CA 92697, USA*
[4] *CIERA and Department of Physics and Astronomy, Northwestern University, 1800 Sherman Avenue, Evanston, IL 60201, USA*
[5] *Center for Computational Astrophysics, Flatiron Institute, 162 5th Avenue, New York, NY 10010, USA*
[6] *Center for Astrophysics and Space Sciences, University of California San Diego, San Diego, CA 92093, USA*
[7] *Canadian Institute for Theoretical Astrophysics, University of Toronto, Toronto, ON M5S 3H8, Canada*
[8] *Department of Physics and Astronomy, Pomona College, Claremont, CA 91711, USA*
[9] *The Observatories of the Carnegie Institution for Science, 813 Santa Barbara Street, Pasadena, CA 91101, USA*
[10] *Department of Astronomy, University of Geneva, Chemin Pegasi 51, 1290 Versoix, Switzerland*
[11] *Cosmic Dawn Center (DAWN), Niels Bohr Institute, University of Copenhagen, Jagtvej 128, København N, DK-2200, Denmark*
[12] *Department of Astrophysical Sciences, Princeton University, Princeton, NJ 08544, USA*
[13] *Department of Physics & Kavli Institute for Astrophysics and Space Research, Massachusetts Institute of Technology, Cambridge, MA 02139, USA*

Accepted 2024 November 22. Received 2024 October 22; in original form 2024 July 10

ABSTRACT

Recent observations with *JWST* have uncovered unexpectedly high cosmic star formation activity in the early Universe, mere hundreds of millions of years after the big bang. These observations are often understood to reflect an evolutionary shift in star formation efficiency (SFE) caused by changing galactic conditions during these early epochs. We present FIREbox^{HR}, a high-resolution, cosmological hydrodynamical simulation from the *Feedback in Realistic Environments* (FIRE) project, which offers insights into the SFE of galaxies during the first billion years of cosmic time. FIREbox^{HR} re-simulates the cosmic volume ($L = 22.1$ cMpc) of the original FIREbox run with eight times higher mass resolution ($m_\mathrm{b} \sim 7800\, M_\odot$), but with identical physics, down to $z \sim 6$. FIREbox^{HR} predicts ultraviolet (UV) luminosity functions in good agreement with available observational data. The simulation also successfully reproduces the observed cosmic UV luminosity density at $z \sim 6$–14, demonstrating that relatively high star formation activity in the early Universe is a natural outcome of the baryonic processes encoded in the FIRE-2 model. According to FIREbox^{HR}, the SFE–halo mass relation for intermediate mass haloes ($M_\mathrm{halo} \sim 10^9$–$10^{11}$ M$_\odot$) does not significantly evolve with redshift and is only weakly mass-dependent. These properties of the SFE–halo mass relation lead to a larger contribution from lower mass haloes at higher z, driving the gradual evolution of the observed cosmic UV luminosity density. A theoretical model based on the SFE–halo mass relation inferred from FIREbox^{HR} allows us to explore implications for galaxy evolution. Future observations of UV faint galaxies at $z > 12$ will provide an opportunity to further test these predictions and deepen our understanding of star formation during Cosmic Dawn.

Key words: methods: numerical – galaxies: evolution – galaxies: high-redshift – galaxies: luminosity function, mass function – galaxies: star formation.

1 INTRODUCTION

The first billion years of cosmic time were a pivotal epoch in the history of our Universe that witnessed the formation of the first galaxies, the rapid growth of supermassive black holes, and the reionization of intergalactic hydrogen (Stark 2016; Dayal 2019; Inayoshi, Visbal & Haiman 2019; Robertson 2022). Before the launch of the *JWST*, the ultraviolet (UV) luminosity and star formation rate (SFR) of galaxies at high redshifts were primarily constrained by observations from the *Hubble Space Telescope* (*HST*) and ground-based facilities. These observations provided crucial insights into the galaxy population up to $z \sim 10$, revealing a steep faint-end slope of the UV luminosity

---

★ E-mail: robert.feldmann@uzh.ch

★ †Authors listed in alphabetical order.

function (LF) and a fast decline in their overall normalization with increasing redshift (e.g. McLure et al. 2013; Bouwens et al. 2015; Finkelstein et al. 2015; Oesch et al. 2018; Bouwens et al. 2022). However, the number densities and properties of galaxies at $z \gtrsim 9$ were not well constrained with challenges arising from, e.g. low number statistics and lensing uncertainties (Bouwens et al. 2017; Atek et al. 2018).

The advent of *JWST* has transformed our understanding of high-redshift galaxy evolution, thanks to its excellent sensitivity, resolution, and wavelength coverage. Among many other findings, *JWST* revealed a higher-than-expected density of UV-bright galaxies at high z (Finkelstein et al. 2022; Naidu et al. 2022; Finkelstein et al. 2023; Labbé et al. 2023; Casey et al. 2024), confirmed spectroscopically the presence of galaxies up to $z \sim 14$ (Curtis-Lake et al. 2023; Robertson et al. 2023; Carniani et al. 2024; Castellano et al. 2024; Harikane et al. 2024), and uncovered the population of galaxies most likely responsible for reionization (Atek et al. 2024). Furthermore, *JWST*-based studies showed an elevated UV luminosity density $\rho_{\rm UV}$ at $z > 10$ compared with both previous observational estimates and modelling predictions (Finkelstein et al. 2023; Harikane et al. 2023; Donnan et al. 2023a; Bouwens et al. 2023b; Donnan et al. 2023b; Chemerynska et al. 2024; Conselice et al. 2024; Harikane et al. 2024), suggesting that an important component of galaxy theory is either missing or not sufficiently understood. Solving this conundrum is critical, not only to gain a better understanding of the physical processes driving galaxy evolution at high z but also to constrain the impact of galaxies on cosmic reionization.

The elevated UV luminosity density may arise from an increase in the star formation efficiency (SFE)[1] of galaxies at higher redshift (e.g. Ceverino et al. 2024; Chakraborty & Choudhury 2024; Harikane et al. 2024). Two main arguments support this statement.

First, models with a non-evolving SFE–halo mass relation match the observed UV luminosity density at $z \sim 6 - 10$ but underpredict $\rho_{\rm UV}$ at $z > 10$ (e.g. Mason, Trenti & Treu 2015; Tacchella et al. 2018; Harikane et al. 2022). This argument is further strengthened by many empirical or semi-analytical models appearing to favour significant evolution to match observations (Sun & Furlanetto 2016; Behroozi et al. 2019; Sabti, Muñoz & Blas 2022; Qin, Balu & Wyithe 2023; Chakraborty & Choudhury 2024; Sipple & Lidz 2024; Wang et al. 2024). Cosmological hydrodynamical simulations targeting galaxies at $z > 10$ have not fully resolved this issue as they yield significantly varying predictions for the UV luminosity density (e.g. Wilkins et al. 2022; Kannan et al. 2023; Ceverino et al. 2024), perhaps indicating gaps in our understanding of the physics during the Cosmic Dawn. Intriguingly, recent simulations analysing $z = 8$–12 suggest that this tension could be resolved with standard astrophysical modelling (Sun et al. 2023c).

Secondly, the observation of massive, luminous galaxies suggests that at least some galaxies are efficient in converting accreted baryonic matter into stars (Boylan-Kolchin 2023; Labbé et al. 2023; Casey et al. 2024), potentially pointing to a failure of feedback processes limiting star formation (Bassini et al. 2023; Dekel et al. 2023; Li et al. 2024; Mirocha & Furlanetto 2023). We note, however, that some observational studies suggest a mild to absent evolution in the SFE of galaxies at high redshift (Stefanon et al. 2021; Harikane et al. 2022). Moreover, the presence of UV bright galaxies may also be explained in other ways, e.g. via a highly stochastic star formation activity (Pallottini & Ferrara 2023; Shen et al. 2023a; Sun et al. 2023a, c; Kravtsov & Belokurov 2024), low-dust attenuation (Ferrara, Pallottini & Dayal 2023), active galactic nucleus (AGN) contamination (Hegde, Wyatt & Furlanetto 2024), or a top-heavy stellar initial mass function (IMF) that increases the UV luminosity per SFR (Harikane et al. 2023).

In this work, we analyse the SFE of UV faint galaxies and address the origin of the elevated cosmic UV luminosity density with the help of FIREbox^{HR}, a novel hydrodynamical, cosmological simulation from the *Feedback in Realistic Environment s* (FIRE) project[2] (Hopkins et al. 2014). This simulation is a re-run of the original FIREbox cosmological volume simulation (Feldmann et al. 2023) to $z = 6.3$ but with eight times more particles (2×2048^3) and at the numerical resolution of standard FIRE zoom-in runs. FIREbox^{HR} is well suited to analyse the cosmic UV luminosity given its accurate modelling of baryonic processes with the FIRE-2 physics model (Hopkins et al. 2018) and its high numerical resolution, which enables it to properly resolve UV faint galaxies and their interstellar medium (ISM). FIREbox^{HR} also extends previous zoom-in studies with FIRE-2 physics focusing on the SFE and stellar mass–halo mass relation of high-redshift galaxies (Ma et al. 2018, 2019; Sun et al. 2023c), as it covers a much larger volume thus improving statistics. Crucially, many properties of galaxies simulated with FIRE-2 physics, such as their masses, SFRs, morphologies, and ISM compositions, have already been validated against observations over a broad range in redshift (e.g. Wetzel et al. 2016; Chan et al. 2018; Hopkins et al. 2018; Garrison-Kimmel et al. 2019; Ma et al. 2019; Feldmann et al. 2023; Gensior et al. 2023; Bassini et al. 2024; Liang et al. 2024; Marszewski et al. 2024), i.e. the results of FIREbox^{HR} are genuine predictions and not the result of tuning to high-redshift observations.

As we will demonstrate in this work, the above arguments in favour of a strongly evolving SFE–halo mass relation are not substantiated by FIREbox^{HR}. Instead, the simulation predicts a non-evolving SFE–halo mass relation and, yet, well reproduces both the UV LFs and the UV luminosity density evolution at $z \sim 6 - 14$, suggesting that no fundamentally new physics is involved in setting the UV luminosities of galaxies of low-to-intermediate mass at these redshifts.

This paper is structured as follows. In Section 2, we introduce the FIREbox^{HR} simulation and describe our data analysis. The UV LFs and the UV luminosity density in the simulation are discussed in Section 3.1. We measure the SFE–halo mass relation for different SFR tracers in Section 3.2 and link these results to the stellar-to-halo mass relation (SHMR) in Section 3.3. A theoretical model based on the measured SFE–halo mass relation is presented in Section 3.4. Its implications for the UV luminosity density evolution and the cosmic reionization history are explored in Sections 3.5 and 3.6. Caveats are addressed in Section 3.7. Finally, we summarize our main findings and conclude in Section 4.

2 METHODOLOGY

2.1 Simulation set-up and included physics

The simulation introduced in this work, FIREbox^{HR}, is a re-run of the original FIREbox simulation presented in Feldmann et al. (2023) at a higher numerical resolution but with otherwise identical physics. FIREbox^{HR} traces the evolution of gas, stars, and dark matter in a cubic volume with a $L = 22.1$ cMpc side length and periodic boundary conditions from the initial redshift $z_{\rm init} = 120$ down to $z = 6.3$. Initial

---

[1] The SFE, as used here, is a dimensionless quantity that measures the SFR in a galaxy relative to the growth rate of its host halo (see Section 3.2).

[2] https://fire.nort hwestern.edu

conditions for the simulation were created with the MUlti-Scale Initial Conditions (MUSIC[3]) code (Hahn & Abel 2011) for Planck 2015 cosmological parameters ($h = 0.6774$, $\Omega_{\rm m} = 0.3089$, $\Omega_{\rm b} = 0.0486$, $\Omega_\Lambda = 0.6911$, $\sigma_8 = 0.8159$, $n_{\rm s} = 0.9667$; Ade et al. 2016) and with a transfer function calculated by the Code for Anisotropies in the Microwave Background (CAMB[4]; Lewis, Challinor & Lasenby 2000). These initial conditions are identical to those of the original FIREbox run except that they include additional high wavenumber modes. Gas particles are assigned an initial metallicity of 2×10^{-6} and a temperature of 201.95 K/μ, where μ is the mean molecular weight.

The simulated volume consists initially of 2048^3 gas particles with a mass of 7823 $M_\odot$ and the same number of dark matter particles with a mass of 41899 $\mathrm{M}_\odot$. The force softening lengths (Plummer equivalent) of gas particles are adaptive and tied to the gas interparticle separation, with a minimum value of 0.5 proper pc at $z \leq 9$ and 5 comoving pc at $z \geq 9$. Softening lengths of dark matter particles (star particles) are held fixed at 40 proper pc (4 proper pc) at $z \leq 9$ and at 400 comoving pc (40 comoving pc) at $z \geq 9$.

Starting from the initial conditions, the evolution of the matter components in the cosmic volume is followed numerically with GIZMO.[5] Gravitational forces are calculated with a tree gravity solver (Springel 2005; Springel et al. 2008), while the equations of fluid dynamics are solved with the meshless-finite-mass method (Hopkins 2015). The FIRE-2 model, an updated version of FIRE, is used to account for baryonic processes and we refer the reader to Hopkins et al. (2018) for details. Specifically, heating and cooling rates include terms arising from, e.g. free-free, photoelectric, photoionization/recombination, metal-line, fine-structure, and molecular processes (Katz, Weinberg & Hernquist 1996; Verner & Ferland 1996; Ferland et al. 1998; Wiersma, Schaye & Smith 2009). Radiative effects from sources in the simulation volume are calculated in the LEBRON approximation Hopkins et al. (2018). Photoionization and photoheating from a spatially uniform, but time-dependent, UV background is also included starting at $z = 10.6$ (Faucher-Giguère et al. 2009). A Sobolev-length like approximation is used to calculate the shield-shielding from local sources and the UV background (Gnedin, Tassis & Kravtsov 2009; Faucher-Giguère et al. 2010; Rahmati et al. 2013). A total of 15 species (hydrogen, helium, nine metal species, and 4 tracer field for different r-process models) are followed in the baryonic components. Metal diffusion from unresolved turbulence is included following Su et al. (2017). Stars may form only in dense (> 1000 cm^{-3}), self-gravitating, Jeans unstable gas at a volumetric rate of $\rho_{\rm SFR} = f_{\rm H2}\,\rho_{\rm gas}/t_{\rm ff}$, where $t_{\rm ff}$ is the local free-fall time and $f_{\rm H2}$ is the molecular gas fraction. The latter is calculated as described in Krumholz & Gnedin (2011). Star formation is implemented in a stochastic fashion, whereby individual gas particles transform into star particles, inheriting attributes such as position, mass, momentum, and metallicity in the process. Feedback from stellar sources include mass, momentum, metal, and energy (kinetic, thermal, and radiative) injections as a result of stellar winds and supernovae (types II and Ia). Feedback from AGNs is not included in FIREbox^{HR}.

A total of 97 simulation save-points are stored covering redshifts $z = 99$ to $z = 6.3$ with an average spacing of ~ 9 Myr. These include 28 full data snapshots (levels 0 and 1) as well as 69 'snipshots' (level 2) that store only the most relevant subset of the full data; see Feldmann et al. (2023) for details on the content of snapshot and snipshots. A snapshot takes up about 600–700 GB, while a snipshot requires about 230–260 GB, adding to a grand total of about 35 TB to store FIREbox^{HR}. Advancing the simulation from the initial state to $z = 6.3$ took 5.04 million core hours and a wall-clock time of 20.6 d.

2.2 Post-processing

We use the AMIGA halo finder (AHF; Gill, Knebe & Gibson 2004; Knollmann & Knebe 2009) to identify dark matter (sub-)haloes and the galaxies at their centres. Halo masses and sizes are defined using the virial overdensity criterion by Bryan & Norman (1998). Haloes with 300 or more dark matter particles ($M_{\rm halo} \gtrsim 10^7\,\mathrm{M}_\odot$) are analysed, resulting in about 2.6×10^4 (9.8×10^4, 2.1×10^5, 3.6×10^5, 4.4×10^5) haloes at $z = 15$ ($z = 12$, $z = 10$, $z = 8$, $z = 6.3$). Physical galaxy properties such as stellar masses and SFRs are measured within spherical apertures with a 3 proper kpc radius from the halo centre. This radius is reduced to the virial radius (for main haloes) or the tidal radius (for proper sub-haloes) if those are smaller than 3 kpc. The aperture size is motivated by *JWST* observations which show that two-dimensional aperture diameters of 0.3 and 0.7 arcsec (1.8 and 4 kpc at $z = 6$) typically contain 70–80 per cent and 85–90 per cent of the total flux (Naidu et al. 2022; Finkelstein et al. 2023; Tacchella et al. 2023; Donnan et al. 2023a; Adams et al. 2024). However, our results are not very sensitive to the exact choice of this radius. Unless explicitly stated otherwise, satellite galaxies and subhaloes are included in the analysis, except for those objects that are within 3 proper kpc of their parent central galaxy and main halo to avoid double counting.

UV magnitudes of galaxies are calculated with the help of the radiative transfer code SKIRT version 9 (Camps & Baes 2020), accounting for dust attenuation, or with a simpler approach described further below in the dust-free approximation. Either method employs the Binary Population and Spectral Synthesis (BPASS; Eldridge & Stanway 2009) library version 2.2.1 (Stanway & Eldridge 2018) that includes binary stellar systems and with a Chabrier (2003) stellar IMF, exponential cut-off below 1 $\mathrm{M}_\odot$, high-mass slope of -2.3, and a maximum mass of 300 $\mathrm{M}_\odot$. The input to SKIRT are the positions, velocities, initial masses (set to $m_{\rm b}$), metallicities, and ages of all star particles within the virial radius of a given halo. We also provide the distance to the 32th nearest star particle neighbour as a smoothing length, thus adaptively spreading out the light distribution of each star particle to reduce particle noise. Furthermore, we provide positions, velocities, masses, smoothing lengths, metallicities, and temperatures of all gas particles in the halo. The dust-to-metal ratio is set to 0.4 (Dwek 1998; Draine et al. 2007; Watson 2011; Li, Narayanan & Davé 2019) and a Milky-Way grain-size distribution is adopted with $R_{\rm V} = 3.1$ and $b_{\rm c} = 6 \times 10^{-5}$ (Weingartner & Draine 2001). For this dust model, FIRE galaxies reproduce the observed IRX-β relation and the $L_{\rm IR}$–SFR relation (Liang et al. 2021, 2024). However, as will be shown later, the main findings of this paper are not strongly affected by the presence of dust. We defer a more thorough exploration of dust models to future work. To reduce computational cost, we consider only two camera angles per galaxy, face-on and edge-on based on the angular momentum vector of star particles in the central 1 kpc. Each voxel in the data cube output by SKIRT stores νf_ν, where $f_\nu(x, y, \nu)$ is the specific intensity (spectral radiance), for a projected two-dimensional spatial position (x, y) and frequency ν. Subsequently, the rest-frame specific intensity is averaged over the spectral dimension using a boxcar filter B centred on 0.15 µm with a width of 0.02 µm, resulting in the map $f_{\rm UV}(x, y) = \int {\rm d}\nu\, f_\nu(x, y, \nu) B(\nu)/\nu / \int {\rm d}\nu\, B(\nu)/\nu$. Next, the map $f_{\rm UV}$ is integrated over a circle with a 3 proper kpc radius centred

---

[3] https://www-n.oca.eu/ohahn/MUSIC

[4] https://www.camb.info

[5] http://www.tapir.caltech.edu/~phopkins/Site/GIZMO.html

on the galaxy, resulting in an estimate of the spectral flux density. The latter is converted into an absolute magnitude in the AB system (Oke & Gunn 1983) via $M_{\rm UV} = -2.5\lg f_{\rm UV} - 48.6$. While this first method accurately accounts for the effects of dust-radiative transfer, it also incurs a high computational cost.

An alternative, computationally cheaper approach is to calculate UV magnitudes of galaxies in the dust-free limit by summing the luminosities of their star particles. To this end, we bi-linearly interpolate the spectral luminosities (per unit stellar mass) provided by the BPASS library for the given ages and metallicities of all star particles within a 3 proper kpc ball from the centre of the galaxy. After multiplying with the initial stellar mass we calculate the spectral UV luminosity of a given star particle by averaging of the 0.15 µm UV filter band as described above for the SKIRT analysis. We finally sum the spectral UV luminosities and convert them into absolute UV magnitudes.

In this work, we combine both approaches to obtain accurate UV luminosities at a lower computational cost. Specifically, we employ the first method for the nth most massive haloes at a given snapshot and the second approach for the remaining haloes. Here, n is in the range of 51–1001 depending on snapshot. It is chosen to conservatively include all haloes with $M_{\rm halo} \geq 5\times10^8\,{\rm M}_\odot$ at $z \geq 13$, with $M_{\rm halo} \geq 10^9\,{\rm M}_\odot$ at $z\sim 10$–12, and with $M_{\rm halo} \geq 3\times10^9\,{\rm M}_\odot$ at $z \leq 9$. As demonstrated by Fig. A1 in the Appendix, the importance of dust attenuation depends strongly on halo mass but not redshift. For haloes less massive than $3\times10^9\,{\rm M}_\odot$, the magnitude difference is lower than 0.05 mag on average, allowing us to replace the radiative transfer calculation with the simpler, dust-free estimate in the interest of reducing the computational cost.

Uncertainties for most estimates are calculated via bootstrapping with the help of PYTHON's SCIPY.STATS.BOOTSTRAP routine. Parametrized fitting uses PYTHON's SCIPY.OPTIMIZE.CURVE_FIT function with weights usually set to the 1σ uncertainties obtained via bootstrapping.

3 RESULTS

3.1 UV LF and luminosity density in FIREbox^{HR}

Because of its high dynamic range, FIREbox^{HR} includes galaxies with a wide range of properties, including low-mass, UV faint galaxies below current observational limits as well as moderately luminous galaxies with significant levels of dust attenuation. For instance, the simulation volume contains about 2300 (540) galaxies with UV magnitudes brighter than −14 at $z = 6.3$ ($z = 10$) as well as a smaller number of luminous galaxies with UV magnitudes reaching up to −21 at $z\sim 6$–7, −20 at $z\sim 8-11$, and −18 at $z\sim 12$–15. To put this in perspective, $z\sim 8$ galaxies with a rest-frame, dust-attenuated UV magnitude of −14 (−20) have stellar masses of the order of $10^6\,{\rm M}_\odot$ ($3\times10^8\,{\rm M}_\odot$) and halo masses of $10^9\,{\rm M}_\odot$ ($5\times10^{10}\,{\rm M}_\odot$; see Fig. B1 in the Appendix). Consequently, FIREbox^{HR} allows us to both probe the shape of the UV LF and to explore the evolution of the cosmic UV luminosity density from the end of Cosmic Dawn to the final stages of hydrogen reionization.

According to Fig. 1, the UV LFs predicted by FIREbox^{HR} are in good agreement with observational estimates from *JWST* and *HST* at $z\sim 6-14$ (McLure et al. 2013; Bouwens et al. 2022; Harikane et al. 2022, 2023; Naidu et al. 2022; Pérez-González et al. 2023; Donnan et al. 2023a, 2024; Robertson et al. 2024; Bouwens et al. 2023b; Adams et al. 2024; Atek et al. 2024; Finkelstein et al. 2024). In particular, the LFs follow closely the observed double-power-law or Schechter function parametrization over a broad range in UV luminosity and with a normalization that decreases towards higher redshifts.

The simulations suggest a subtle change (‘turn-over’) in the LF at UV magnitudes just below that of the current observational threshold (around −14 to −15) at $z\sim 6$–8, where they diverge from the Schechter function extrapolation to faint magnitudes based on observed data. Interestingly, a turn-over at such UV magnitudes appears to be required to avoid producing too many satellites around Milky-Way like galaxies in today's Universe (Boylan-Kolchin, Bullock & Garrison-Kimmel 2014; Boylan-Kolchin et al. 2015). The turn-over in the UV LFs of FIREbox^{HR} appears at $z \lesssim 10$, pointing to reionization as its physical origin (e.g. Wu & Kravtsov 2024). At earlier cosmic time, the faint end of the UV LFs resembles a power law. We caution, however, that the faint end is dominated by low-mass galaxies some of which are only marginally resolved in FIREbox^{HR}. To illustrate the role of numerical resolution, we also show UV LFs once we restrict our sample to galaxies with $M_{\rm star} > 10^5\,{\rm M}_\odot$ (12–15 star particles) and $M_{\rm star} > 10^{5.5}\,{\rm M}_\odot$ (35–50 star particles).

Furthermore, at $z = 15$ the figure shows a flattening of the UV LF at the luminous end. We caution the reader, however, that low number statistics, star formation variability, and cosmic variance significantly affect our results at the luminous end and at the earliest cosmic times, while effects related to numerical resolution could potentially have an impact on the predicted faint-end of the UV LF in FIREbox^{HR}.

The role of dust attenuation is limited to the bright end of our UV LFs. For instance, the number density of galaxies at $z = 6.3$–10 with a UV magnitude of −18.5 increases by about 0.1–0.3 dex if we consider intrinsic, i.e. not dust-attenuated UV luminosities, while the LF at UV magnitudes fainter than −17.5 is unchanged. The presence or absence of dust also has no impact on our UV LFs at $z > 10$ given the dearth of massive, bright galaxies in the simulation at those redshifts. The limited dust attenuation in FIREbox^{HR} galaxies reflects their low stellar masses and, consequently, low gas-phase metallicities. For a detailed analysis of the mass–metallicity relation in high-redshift galaxies with FIRE-2 physics, see Marszewski et al. (2024).

In this work, we calculate the cosmic UV luminosity density by adding the UV luminosities of all galaxies brighter than a given UV magnitude limit $M_{\rm UV,lim}$ and then dividing the total luminosity by the simulation volume. This direct approach is feasible since FIREbox^{HR} reproduces the number and luminosities of galaxies dominating the cosmic UV luminosity density. Specifically, as evidenced by Fig. 2, half the dust-attenuated UV luminosity density in galaxies brighter than $M_{\rm UV,lim} = -17$, denoted as $M_{\rm UV,50\ per\ cent}$, arises from the subset of galaxies fainter than −18.4 at $z = 6.3$ and fainter than about −18 at $z = 10$. These UV luminosities correspond to galaxies with typical stellar masses of $M_{\rm star}\sim 10^{7.5}$–$10^8\,{\rm M}_\odot$ that reside in haloes with $M_{\rm halo}\sim 10^{10}$–$10^{10.5}\,{\rm M}_\odot$ (see Fig. B1 in the Appendix). These stellar masses are in line with observations, e.g. Endsley et al. (2023a) find that galaxies with $M_{\rm UV}\sim -18.4$ have typical stellar masses of $M_{\rm star}\sim 10^{7.5}$–$10^8\,{\rm M}_\odot$ at $z\sim 6-7$.

A linear regression provides the following estimate of $M_{\rm UV,50\ per\ cent}$ for redshifts in the range ~ 6–12

$$M_{\rm UV,50\ per\ cent} = 0.12(z-6) - 18.52. \quad (1)$$

Our predictions are comparable to measured values based on integrating the observed UV LFs at $z\sim 6$–11. For instance, we obtain $M_{\rm UV,50\ per\ cent} = -18.76$ based on the $z = 7$ double-power-law UV LF by Harikane et al. (2022) and $M_{\rm UV,50\ per\ cent}\sim -18.1$ for the $z = 10$ UV LF by Bouwens et al. (2023a). According to these UV LFs, UV bright ($M_{\rm UV} < -20$) galaxies contain less than 18 per cent and ∼ 10 per cent of the total UV luminosity density at $z = 7$ and

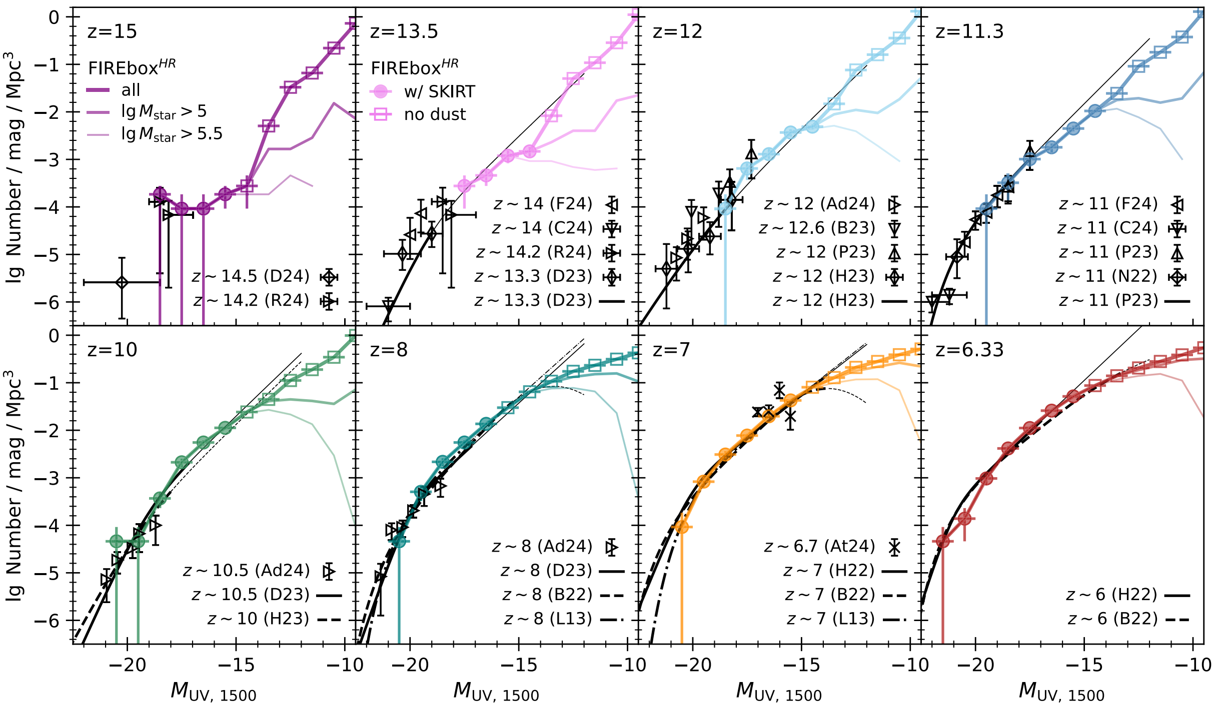

Figure 1. Rest-frame UV LFs of galaxies in FIREbox^{HR} at $z\sim 6-15$ (coloured circles, squares, and lines) and comparison with observational data (black symbols and thick lines; thin black lines show extrapolations of the observed UV LFs to faint magnitudes): McLure et al. 2013 (L13), Harikane et al. 2022 (H22), Naidu et al. 2022 (N22), Bouwens et al. 2022 (B22), Bouwens et al. 2023b (B23), Donnan et al. 2023a (D23), Harikane et al. 2023 (H23), Pérez-González et al. 2023 (P23), Adams et al. 2024 (Ad24), Atek et al. 2024 (At24), Casey et al. 2024 (C24), Donnan et al. 2024 (D24), Finkelstein et al. 2024 (F24), and Robertson et al. 2024 (R24). The UV luminosities are calculated with the dust-radiative transfer code SKIRT for the more massive galaxies (filled circles) and in an optically thin approximation for the remaining, largely dust-free, galaxies (empty circles). Vertical error bars of the UV LFs in FIREbox^{HR} are obtained via bootstrapping, while horizontal error bars indicate bin-widths. Thinner coloured lines indicate the UV LFs when galaxies with stellar masses below 10^5 M$_\odot$ ($\sim$ 12–15 star particles) or below 3×10^5 M$_\odot$ ($\sim 35-50$ star particles) are excluded. FIREbox^{HR} reproduces the observed UV LFs at moderate to low luminosities and their evolution over $z\sim$ 6–14.

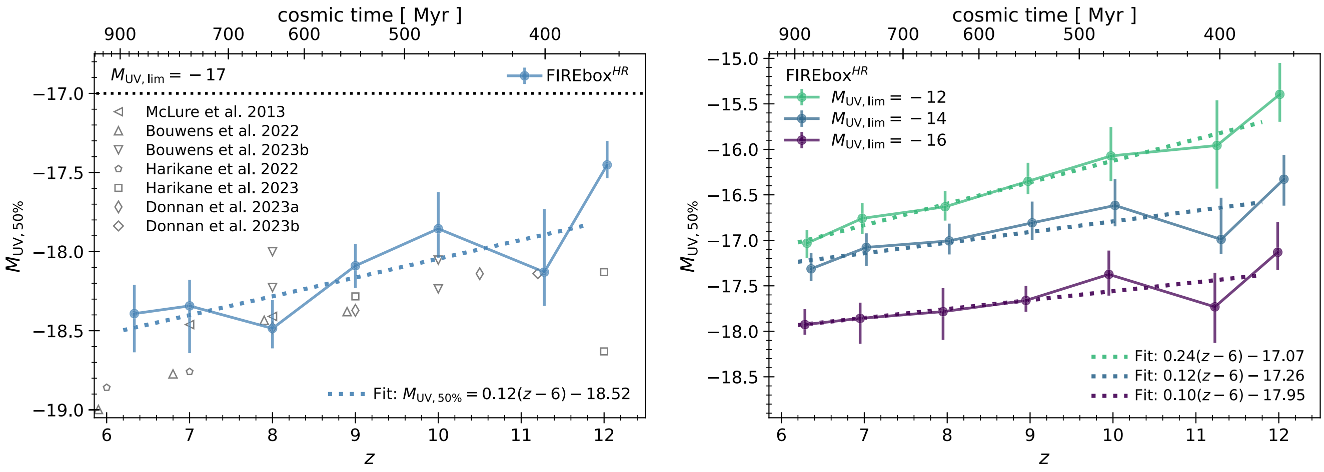

Figure 2. Typical rest-frame UV) magnitude, $M_{\rm UV,\,50\ per\ cent}$, of galaxies dominating the cosmic UV luminosity density as function of redshift. By definition, galaxies brighter than $M_{\rm UV,\,50\ per\ cent}$ produce the same luminosity density as galaxies with UV magnitudes between $M_{\rm UV,\,50\ per\ cent}$ and the threshold value $M_{\rm UV,lim}$. Left: Simulation results (blue circles and error bars) are calculated from the cumulative UV luminosity distribution of all galaxies in the simulation volume with $M_{\rm UV}\leq -17$ (including dust attenuation). Error bars are obtained via bootstrapping. The dotted line shows the result of a linear fit to the simulation data at $z<11.5$. Grey symbols show estimates based on integrating UV LFs from the literature down to $M_{\rm UV}=-17$ including both Double-power-law and Schechter function fits (McLure et al. 2013; Harikane et al. 2022, 2023, Bouwens et al. 2023a; Donnan et al. 2023a, b). For $M_{\rm UV,lim}=-17$, galaxies with UV magnitudes fainter than -18.5 (and with $M_{\rm halo}<3\times 10^{10}$ M$_\odot$, see Fig. B1) dominate the cosmic UV luminosity density at $z\sim$ 6–12. Right: Analogous to left panel but showing predictions for $M_{\rm UV,\,50\ per\ cent}$ for different choices of $M_{\rm UV,lim}$. The cosmic UV luminosity density in FIREbox^{HR} at $z\sim$ 6–11 is dominated by faint galaxies (-16 to -17 for $M_{\rm UV,lim}=-12$).

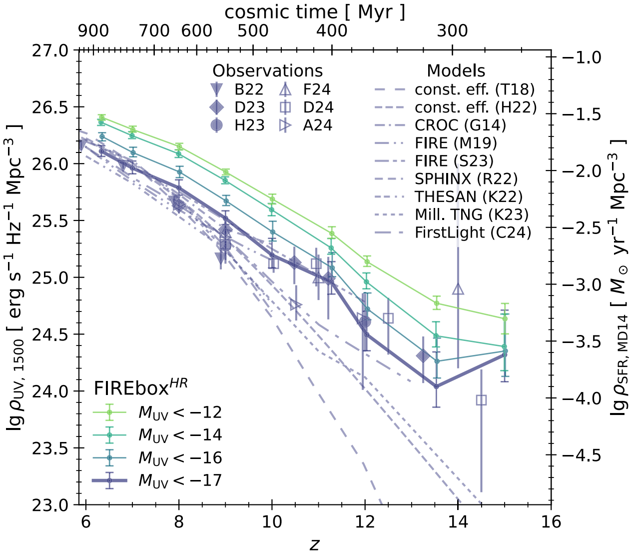

Figure 3. Evolution of the dust-attenuated UV luminosity density in FIREbox^{HR} at $z \sim 6$–15 for different values of the UV magnitude limit. Uncertainties (16–84 per cent) in the UV luminosity density are estimated via bootstrapping. The simulation data are compared with observational data by Bouwens et al. (2022), Donnan et al. (2023a, b), Harikane et al. (2023), Adams et al. (2024), Finkelstein et al. (2024), and Donnan et al. (2024), as well as with theoretical predictions based on the empirical models by Tacchella et al. (2018) and Harikane et al. (2022), the cosmic re-ionization on computers (CROC) simulation suite (Gnedin 2014), FIRE-2 zoom-in simulation suites by Ma et al. (2019) and Sun et al. (2023c), the SPHINX^{20} simulation (Rosdahl et al. 2022), the THESAN-1 simulation (Kannan et al. 2022), the Millennium-TNG simulation (Kannan et al. 2023), and the FirstLight zoom-in suite (Ceverino et al. 2024). A UV magnitude limit of −17 is adopted for all literature data. Small horizontal shifts ($\Delta z < 0.05$) are applied to some data points to increase readability. The treatment of dust attenuation in the various models is discussed in the text. The UV luminosity density predicted by FIREbox^{HR} agrees well with observational data, in particular those based on recent *J WST* observations, and it evolves more gradually at high redshift than predicted by many previous models.

$z = 10$ for $M_{\rm UV,lim} = -17$. We conclude that the SFE of massive, UV bright ($M_{\rm UV} < -20$) galaxies has little bearing on the evolution of the cosmic UV luminosity density for $M_{\rm UV,lim} = -17$.

Fig. 2 also explores how $M_{\rm UV,50\ per\ cent}$ changes if the UV magnitude limit is raised to include fainter galaxies. As expected, a fainter UV magnitude limit results in a fainter value for $M_{\rm UV,50\ per\ cent}$. In addition, $M_{\rm UV,50\ per\ cent}$ shows a stronger redshift evolution for $M_{\rm UV,lim} \geq -12$. For this faint UV magnitude limit, the cosmic UV luminosity density in FIREbox^{HR} is dominated by galaxies with $M_{\rm UV,\,50\ per\ cent}$ near −16 to −16.5 ($z \sim 8 - 11$) and −17 ($z \sim 6 - 7$), in qualitative agreement with observational estimates (Atek et al. 2024; Mascia et al. 2024). Typical stellar and halo masses of such galaxies are $M_{\rm star} \sim 10^{6.8}$–$10^{7.5}\,{\rm M}_{\odot}$ and $M_{\rm halo} \sim 10^{9.4} - 10^{10}\,{\rm M}_{\odot}$ (see Fig. B1). Such galaxies also tend to have low-dust attenuation (see Fig. A1).

Fig. 3 shows the cosmic UV luminosity density in FIREbox^{HR} calculated as described above for different choices of $M_{\rm UV,lim}$. We compare the simulation predictions to observational data from *JWST* and *HST* for the common choice of $M_{\rm UV,lim} = -17$ (Bouwens et al. 2015; Harikane et al. 2023; Donnan et al. 2023a, b; Adams et al. 2024; Donnan et al. 2024; Finkelstein et al. 2024) finding overall good agreement. At $z \sim 10 - 11$, the predicted UV luminosity density is in line with Donnan et al. (2023a, b, 2024) and Finkelstein et al. (2024) but higher (~ 0.3 dex) than the results reported by Adams et al. (2024). The apparent upturn at $z = 15$ in FIREbox^{HR} is a result of low number statistics combined with a burst of star formation a few Myr earlier boosting UV luminosity.

The figure also shows predictions for UV magnitude limits fainter than −17. At $z \lesssim 10$, the cosmic UV luminosity density is not very sensitive to the choice of the limiting magnitude provided the latter is chosen to be fainter than about −14. For instance, the UV luminosity density at $z = 8$ increases by 0.06 dex (0.30 dex) if $M_{\rm UV,lim}$ is increased from −14 to −12 (from −17 to −14). We attribute the insensitivity of the cosmic UV luminosity to the UV magnitude limit at $z \lesssim 10$ to the shallow slope (turnover) of the faint end of the UV LFs shown in Fig. 1. In contrast, at $z \gtrsim 11$, i.e. before the onset of reionization, the cosmic UV luminosity depends much more noticeably on the chosen UV magnitude limit. For example, at $z = 13.5$, the cosmic UV luminosity density changes by 0.29 dex if $M_{\rm UV,lim}$ is raised from −14 to −12.

Dust attenuation has a generally limited impact on UV luminosity density that further decreases as redshift increases. For $M_{\rm UV,lim} = -17$, the intrinsic UV luminosity density is higher than the dust-attenuated one by 0.22 dex at $z = 6.3$, by 0.15 dex at $z = 10$, and by less than 0.08 dex at $z = 13.5$. The importance of dust attenuation is also reduced for fainter UV magnitude limits, e.g. for $M_{\rm UV,lim} = -14$ the shift is 0.13 (0.07, 0.03) dex at $z = 6.3$ ($z = 10$, $z = 13.5$).

Fig. 3 also includes the UV luminosity density predicted by constant (i.e. non-evolving) efficiency models (Tacchella et al. 2018; Harikane et al. 2022), the Cosmic reionization on computers (CROC) simulation suite (Gnedin 2014), suites of zoom-in FIRE simulations by Ma et al. (2019) and Sun et al. (2023c), the SPHINX^{20} simulation (Rosdahl et al. 2022), the THESAN-1 simulation (Kannan et al. 2022), the Millenium-TNG simulation (Kannan et al. 2023), and the FirstLight zoom-in suite (Ceverino et al. 2024), all for $M_{\rm UV,lim} = -17$. The FLARES simulation (Lovell et al. 2020; Wilkins et al. 2022) reports results only for galaxies brighter than about −18 and is not included in this comparison.

We convert the estimates of the cosmic SFR density by Tacchella et al. (2018) and Harikane et al. (2022) to a luminosity density with the help of the Madau & Dickinson (2014) conversion factor. To account for dust attenuation, we first calculate the typical UV magnitude of galaxies contribution to the cosmic luminosity density via equation (1). We then follow Tacchella et al. (2018) to derive the expected $A_{\rm V}$ of such galaxies via the method proposed by Smit et al. (2012) and reduce the UV luminosity density accordingly. This dust correction primarily affects results for $z \leq 7$. For the CROC suite, we numerically integrate the UV LF functions shown in their Fig. 1 to a magnitude limit of −17. These LFs account for dust attenuation in an approximate fashion based on the overall stellar metallicity each galaxy and a redshift dependent dust column density calibrated against observations (Bouwens et al. 2009). The luminosity densities for SPHINX and THESAN are obtained similarly by sampling the provided UV LFs and integrating them to a magnitude limit of −17. The LFs in THESAN account for dust attenuation in a similar way as Gnedin (2014) but with the redshift-dependent dust-to-metal ratio from Vogelsberger et al. (2020), while those from SPHINX are calculated with dust-radiative transfer. The UV luminosity density provided by Ma et al. (2019) accounts for dust attenuation by post-processing with SKIRT. The results of Sun et al. (2023c) are based on integrating their fitted UV LFs at $z = 8$–12 over the UV magnitude range −26 and −17 with dust attenuation calculated as described in their article, i.e. by combining the $A_{\rm UV}$–$\beta_{\rm UV}$ relation by Fudamoto et al. (2020) with the $\beta_{\rm UV} - M_{\rm UV}$ relation by Cullen et al. (2023). Similarly, we obtain an estimate of the UV luminosity density in

Millennium-TNG by integrating the provided Schechter functions fits of the dust-attenuated UV LFs over the UV magnitude range -26 and -17. Kannan et al. (2023) employ an empirical dust-attenuation model fitted to ALMA observations of galaxies at $z \sim 4-7$ by Bouwens et al. (2016b). Finally, Ceverino et al. (2024) adopt an empirical dust correction based on the observed relation between UV continuum slope and UV magnitude at $z \sim$ 6–9 (Bouwens et al. 2014; Atek et al. 2023).

While these models all predict a UV luminosity density in approximate agreement with both FIREbox^{HR} and observational data at $z \sim$ 6–9, most of them increasingly underestimate the UV luminosity density towards higher redshift. Exceptions are the SPHINX^{20} simulation (Rosdahl et al. 2022), which matches the predictions of FIREbox^{HR} at $z = 10$ but does not provide estimates for higher redshifts, the FIRE-2 zoom-in suites by Ma et al. (2019) and Sun et al. (2023c), which match FIREbox^{HR} out to $z = 10$ and $z = 12$, respectively, and the FirstLight suite (Ceverino et al. 2024), which underpredicts the observed UV luminosity density at $z \sim$ 10–11 with respect to Donnan et al. (2023a, b, 2024) and Finkelstein et al. (2024), but is in approximate agreement with observations at $z \sim$ 12–13.

3.2 The SFE of galaxies

The SFE is a dimensionless quantity that links the star formation activity of a galaxy to the mass growth rate[6] of its halo. In this work we consider both time-averaged SFRs as well as effective SFRs, derived from both the intrinsic and the dust-attenuated UV luminosity, to quantify star formation activity. Average halo growth rates are calculated based on the current halo mass, using the approximation by Behroozi & Silk (2015), both for simplicity and to allow for a better comparison with the literature. The goal of this section is to characterize the SFE as function of halo mass and redshift as predicted by FIREbox^{HR}.

It is well known that the SFE depends on halo mass, with low-mass haloes generally forming fewer stars per unit accreted halo mass (e.g. Tacchella et al. 2018; Harikane et al. 2022). Consequently, low-mass haloes tend to harbour galaxies with a low stellar mass to halo mass ratio (e.g. Behroozi et al. 2019), see Section 3.3. 'Constant efficiency' models make the ansatz that the SFE–halo mass relation does not evolve with redshift. These models match the observed evolution of the UV luminosity density at $z \sim 4-8$ but seemingly predict too steep an evolution at the highest redshifts, see Fig. 3. An increase of SFE with redshift at such early epochs has been suggested as a potential explanation for this discrepancy (e.g. Harikane et al. 2023; Ceverino et al. 2024; Sipple & Lidz 2024). Given that FIREbox^{HR} reproduces observational constraints at $z \sim$ 6–15, we can use the simulation to test this hypothesis.

Fig. 4 shows the SFE–halo mass relation as function of redshift for galaxies in FIREbox^{HR} using four different approaches. The first approach mimics the observational procedure by Harikane et al. (2022). Galaxies are grouped in bins of their dust-attenuated, rest-frame UV luminosities and for each bin we calculate both the average halo mass and the average intrinsic UV luminosity. The latter is obtained from the dust-attenuated luminosities following the procedure by Smit et al. (2012). The intrinsic UV luminosity is then converted into an SFR via a conversion factor $\kappa = 1.15 \times 10^{-28}\,\mathrm{M}_{\odot}\,\mathrm{yr}^{-1}\,\mathrm{erg}^{-1}\,\mathrm{s\,Hz}$ (Madau & Dickinson 2014). This conversion factor is a compromise value derived for a Salpeter (1955) IMF and for a variety of assumed star formation and enrichment histories. In contrast, our luminosities are calculated for a Chabrier (2003) IMF and for galaxies based on their actual star formation histories and stellar metallicities as predicted by the simulation. While we consequently find that a lower conversion factor of $6 \times 10^{-29}\,\mathrm{M}_{\odot}\,\mathrm{yr}^{-1}\,\mathrm{erg}^{-1}\,\mathrm{s\,Hz}$ better describes the mapping between spectral UV luminosity and SFR for FIREbox^{HR} galaxies, we stick with the Madau & Dickinson (2014) convention for simplicity. The so-derived SFRs may thus be better understood as renormalized UV luminosities.

Before comparing predictions by FIREbox^{HR} with the observational data from Harikane et al. (2022), we note the narrow overlap in halo mass and redshift. Specifically, while FIREbox^{HR} analyses the SFE for $M_{\rm halo} < 10^{11}\,\mathrm{M}_{\odot}$ haloes at $z > 6$, Harikane et al. (2022) studies $\gtrsim 10^{11}\,\mathrm{M}_{\odot}$ haloes at $z < 7$. At face value, FIREbox^{HR} suggests an SFE in $\sim 10^{11}\,\mathrm{M}_{\odot}$ haloes at $z \sim 6$ that is slightly higher (0.2 dex) than the estimates by Harikane et al. (2022). More importantly, however, is the different scaling of the SFE with halo mass. In FIREbox^{HR}, the SFE declines only weakly with decreasing halo mass (for $M_{\rm halo} \sim 10^{9.5} - 10^{11}\,M_{\odot}$). As a consequence, such haloes have a much higher SFE than would be expected from a low-mass extrapolation of the Harikane et al. (2022) result. We will discuss the implications of this result for the evolution of the UV luminosity density in Section 3.5.

The figure also shows that the SFE–halo mass relation evolves little, if at all, with redshift for $M_{\rm halo} > 10^{9.5}\,M_{\odot}$ haloes. At $M_{\rm halo} < 10^{9.5}\,M_{\odot}$ and $z \gtrsim 10$ some evolution is apparent, which we attribute to the scatter in halo mass at fixed UV luminosity combined with the evolution of the halo mass function. Because of this scatter, haloes with a wide range of masses can produce galaxies of a given luminosity. At high z, more massive haloes become increasingly rare in the simulation volume, resulting in a smaller average halo mass at fixed UV luminosity.

In the second method galaxies are binned in halo mass and not in dust-attenuated UV luminosity. SFEs estimated this way provide a direct link between the evolution of the cosmic luminosity or SFR and the evolution of the halo mass function (Trenti et al. 2010; Tacchella, Trenti & Carollo 2013; Mason et al. 2015; Ferrara et al. 2023). In this method, we also derive SFRs via the Madau & Dickinson (2014) conversion factor but this time from the *intrinsic* UV luminosity of galaxies in FIREbox^{HR} to remove another source of uncertainty. SFEs are then calculated for each viewing angle of each galaxy and averaged in the given halo mass bin. The figure shows the common logarithm of the bin-averaged SFE. Overall, we find that the SFE–halo mass relation estimated this way is similar to the one obtained from the first method. The SFE increases with increasing halo mass for $M_{\rm halo} \sim 10^{8.5} - 10^{11}\,\mathrm{M}_{\odot}$ haloes. Furthermore, the SFE–halo mass relation does not significantly evolve with redshift in haloes with $M_{\rm halo} > 10^{9}\,\mathrm{M}_{\odot}$. In contrast to the results from the first method, the efficiency decreases with increasing redshift at the lowest halo masses ($M_{\rm halo} < 10^{9}\,\mathrm{M}_{\odot}$). Clearly, the binning strategy matters for low-mass haloes as they show large variations in the average SFEs with z as well as a high scatter–the standard deviation of lg SFE is in the range $\sim$ 0.4–0.8. The SFE scatter is considerably lower ($\sim$ 0.3–0.4 dex) in haloes with $M_{\rm halo} \sim 10^{10}$–$10^{11}\,\mathrm{M}_{\odot}$.

The third method is similar to the second one but uses the actual time-averaged SFR of galaxies in FIREbox^{HR}. Here, $\mathrm{SFR}_{20\,\mathrm{Myr}}$ is defined as the initial mass in stars formed in the last 20 Myr divided by 20 Myr. The resulting SFEs–halo mass relation has the same shape as in the second method but is shifted downwards by about 0.3 dex because of the use of the Madau & Dickinson (2014) conversion

---

[6] The SFE is sometimes defined relative to the *baryonic* accretion rate of haloes. In this case, the SFE is larger by a factor $1/f_{\rm bar,uni}$ ($\sim$ 0.8 dex) compared to the definition used in this work, where $f_{\rm bar,uni} \sim 0.157$ is the universal baryon fraction.

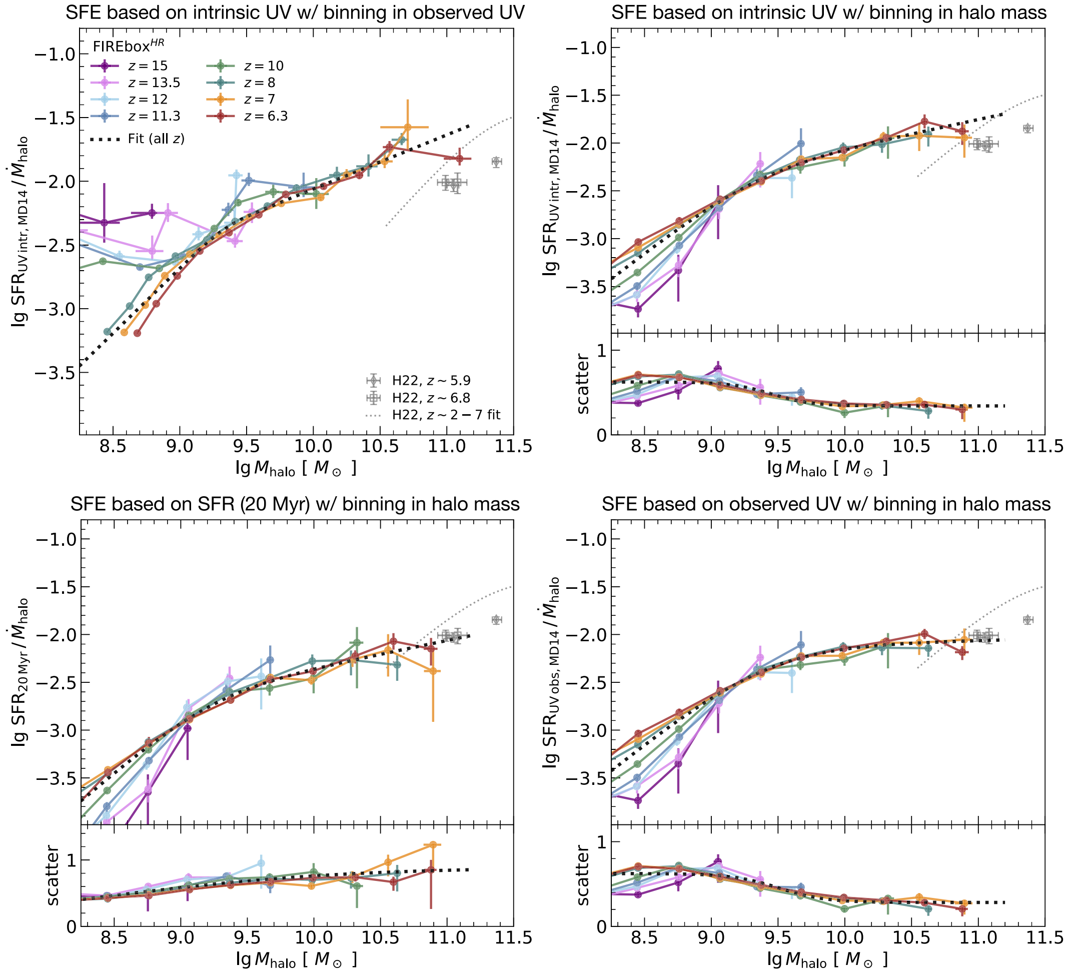

Figure 4. SFE, the ratio of SFR and average halo growth rate, in FIREbox^{HR} as function of redshift and for different halo masses calculated in four different ways. In all panels, the halo growth rate is estimated from the halo mass via the fitting function by Behroozi & Silk (2015). UV luminosities and SFRs are measured within 3 proper kpc from the halo centre, see Section 2.2. Simulation results are shown by coloured symbols and lines. Dotted lines show fits to the FIREbox^{HR} results for the combined redshift range with fit parameters provided in Tables 1 and 2. Grey symbols and lines reproduce the empirical SFE estimates by Harikane et al. (2022). Top left: Estimate of the SFE mimicking the observational approach by Harikane et al. (2022). The average halo mass is calculated in bins of the observed UV luminosity. SFRs are obtained from the intrinsic UV luminosity via a constant conversion factor (Madau & Dickinson 2014), with the intrinsic UV luminosity being derived from the observed UV luminosity of FIREbox^{HR}galaxies based on the $A_{\mathrm{UV}}(\beta)$ relation by Meurer, Heckman & Calzetti (1999) and the $\beta(M_{\mathrm{UV}}, z)$ relation by Bouwens et al. (2014). Top right: Logarithm of the average SFE and the standard deviation ('scatter') of lg SFE calculated from the intrinsic UV luminosity of galaxies in FIREbox^{HR} in bins of halo mass and for different z. The scatter of lg SFE is ~ 0.3 in $M_{\mathrm{halo}} \sim 10^{11}$ $\mathrm{M}_\odot$ haloes and ~ 0.6–0.7 in $M_{\mathrm{halo}} \sim 10^9$ $\mathrm{M}_\odot$ haloes. This scatter measures the variability of the intrinsic UV luminosity at fixed halo mass and does not include contributions from a variability in the halo growth rates. Bottom left: Same as top right except the SFE is calculated from the time-averaged SFR of FIREbox^{HR} galaxies over the past 20 Myr. Galaxies with zero SFRs are excluded from the calculation of the scatter. Bottom right: Same as top right except that the observed, not the intrinsic, UV luminosity is converted into SFR via the constant conversion factor by Madau & Dickinson (2014). All approaches to estimating the SFE are consistent with a largely non-evolving SFE–M_{halo} relation, albeit with significant scatter, in $M_{\mathrm{halo}} > 10^9$ $\mathrm{M}_\odot$ haloes at $z \sim 6$–15.

factor in the previous methods. The scatter in the relation is somewhat larger (~ 0.6–0.7 dex) and almost independent of halo mass over the $M_{\mathrm{halo}} \sim 10^9$–$10^{11}$ $\mathrm{M}_\odot$ range. Results for different choices of the averaging time-scale are shown in Fig. C1 in the Appendix. They are qualitatively identical to the one for a 20 Myr averaging time aside from the reduction in scatter, and the small downward shift in normalization, with increasing SFR averaging time.

The fourth and final method is similar to the second method but SFRs are derived from dust-attenuated, not intrinsic, UV luminosities with the help of the Madau & Dickinson (2014) conversion factor. The SFE–halo mass relation obtained this way can be combined with the halo mass function to predict the dust-attenuated UV LF and density. This fourth method results in an SFE–halo mass relation that is slightly lower in more massive haloes, a consequence of the dust-attenuation in such haloes, but is virtually identical to the one obtained by the second method for low-mass haloes.

We fit the average SFE–halo mass relation over the mass range $10^{8.2}$ $\mathrm{M}_\odot$ $< M_{\mathrm{halo}} < 10^{11.2}$ $\mathrm{M}_\odot$ with a broken power law

$$\lg \mathrm{SFE}(x) = A + \alpha_1 (x - x_{\mathrm{b}}) + (\alpha_2 - \alpha_1)\,\Delta \left[\ln\left(1 + e^{\frac{x - x_{\mathrm{b}}}{\Delta}}\right) - \ln 2 \right], \tag{2}$$

with $x = \lg M_{\mathrm{halo}}$, and five free parameters that specify the pivot log halo mass x_{b}, the amplitude A of the relation at x_{b}, the low-mass slope α_1, the high-mass slope α_2, and the smoothness of the slope change Δ. The fit is based on the binned, average SFE–halo mass relation shown in Fig. 4, combining $z \sim 6$–15, and accounts for the

Table 1. Parametrization of the average SFE–halo mass relation predicted by FIREbox^{HR} for $z \sim 6$–15. The first column denotes whether galaxies are binned in halo mass or in observed (i.e. dust-attenuated) UV luminosity. The SFE–halo mass relation is obtained by fitting equation (2) to the bin-averaged SFEs and halo masses. The entry in the second column refers to the tracer of SFR which can either be the actual intrinsic UV luminosity (‘UV intr’), the intrinsic UV luminosity inferred from the observed UV luminosity via the method by Smit et al. (2012) (‘UV intr ($\beta_{\rm UV}$)’), the observed UV luminosity (‘UV obs’), or the time-averaged SFR. Columns 3–7 list the parameters of the broken power-law fitting function given by equation (2). Use of the fitting functions should be limited to $M_{\rm halo} \lesssim 10^{11.2}$ M$_\odot$ as more massive haloes are not probed by FIREbox^{HR}. The fitting functions shown in the top left, top right, bottom left, and bottom right panels of Fig. 4 correspond to rows 7, 3, 5, and 1.

Binning	SFR tracer	A	$x_{\rm b}$	Δ	α_1	α_2
$M_{\rm halo}$	UV obs	−2.370	9.406	0.341	1.127	0.032
$M_{\rm halo}$	UV intr ($\beta_{\rm UV}$)	−2.418	9.321	0.207	1.039	0.229
$M_{\rm halo}$	UV intr	−2.420	9.311	0.295	1.092	0.299
$M_{\rm halo}$	SFR (100 Myr)	−2.767	9.326	0.108	1.015	0.372
$M_{\rm halo}$	SFR (20 Myr)	−2.752	9.216	0.286	1.204	0.285
$M_{\rm halo}$	SFR (5 Myr)	−2.629	9.384	0.318	1.057	0.287
$M_{\rm UV}$	UV intr ($\beta_{\rm UV}$)	−2.377	9.331	0.078	1.020	0.425

uncertainties of the SFE in each bin. Bins with fewer than three galaxies are excluded from the analysis. The fit is carried out with the `scipy.optimize.curve_fit` function and the resulting fit parameters are provided in Table 1.

All methods infer an average SFE–halo mass relation with the same qualitative properties, but with some differences in detail. First, the normalization is lower by 0.2–0.3 dex when the SFE is calculated based on the actual SFR instead of the UV luminosity. This difference is largely a result of using the Madau & Dickinson (2014) conversion factor which is about 0.28 dex too high given the specific star formation histories and metallicities of galaxies in FIREbox^{HR}. Secondly, using the observed UV luminosity instead of the intrinsic one as an SFR tracer results in a flatter high-mass slope (~ 0.03 versus ~ 0.3) as a result of dust extinction affecting preferentially galaxies in more massive haloes. Finally, binning in UV luminosity results in a moderately steeper high-mass slope.

In a similar fashion, we fit the mass dependence of the scatter of the SFE, i.e. the standard deviation of lg SFE, with a sigmoid function

$$\mathrm{std}(\lg \mathrm{SFE})(x) = c_1 + (c_2 - c_1)\left[1 + e^{-\frac{x - x_{\rm b}}{\Delta}}\right]^{-1}, \tag{3}$$

with $x = \lg M_{\rm halo}$. The four fit parameters are the scatter c_1 and c_2 in the limit of low-mass and high-mass haloes, the smoothness of the transition Δ, and the log halo mass at the transition $x_{\rm b}$. Fit parameters can be found in Table 2.

Table 2. Mass dependence of the scatter of the SFE–halo mass relation predicted by FIREbox^{HR} for $z \sim 6$–15. The scatter of the SFE as defined in this work measures the standard deviation of the logarithm of the UV luminosity or SFR, depending on tracer, at fixed halo mass. The first two columns are the same as in Table 1. The final four columns provide the parameters of the sigmoid fitting function given by equation (3).

Binning	SFR tracer	$x_{\rm b}$	Δ	c_1	c_2
$M_{\rm halo}$	UV obs	9.507	0.176	0.624	0.282
$M_{\rm halo}$	UV intr ($\beta_{\rm UV}$)	9.428	0.138	0.623	0.329
$M_{\rm halo}$	UV intr	9.452	0.153	0.624	0.342
$M_{\rm halo}$	SFR (100 Myr)	9.851	0.101	0.484	0.384
$M_{\rm halo}$	SFR (20 Myr)	8.427	0.909	0.000	0.894
$M_{\rm halo}$	SFR (5 Myr)	8.496	0.686	0.000	0.836

The scatter of the relation is of moderate size (~ 0.3–0.7 dex). For UV based estimates, we find a comparably small scatter (~ 0.3 dex) for massive haloes ($M_{\rm halo} \sim 10^{11}$ M$_\odot$) and a higher scatter at lower masses (e.g. $\sim 0.6 - 0.7$ dex for $M_{\rm halo} \sim 10^{8.5}\,M_\odot$). For an SFR averaging-time of 100 Myr the scatter is approximately constant ($\sim$ 0.4 dex) over the same mass range, see also Fig. C1 in the appendix. Shorter SFR averaging-times result generally both in higher scatter and a reversed mass dependence, e.g. for a 20 Myr averaging time-scale the scatter is ~ 0.8 dex at $M_{\rm halo} \sim 10^{11}$ M$_\odot$ and 0.4 dex at $M_{\rm halo} \sim 10^{8.5}$ M$_\odot$. While averaging times of $\sim$ 10–100 Myr are often used to mimic SFR tracers based on far UV (Feldmann, Gnedin & Kravtsov 2012; Leroy et al. 2012; Flores Velázquez et al. 2021), the different halo mass dependence of the scatter shows that the variability of the UV luminosities of galaxies is not fully captured by averaging SFRs over fixed time-intervals.

In summary, all four approaches of quantifying the SFE of galaxies reveal a well-defined SFE–halo mass relation with a moderate amount of scatter (Fig. 4). The SFE–halo mass relation is approximately redshift independent for haloes of intermediate mass ($M_{\rm halo} \sim 10^9$–10^{11} M$_\odot$) at $z \sim 6$–10 and our results are consistent with an extension of this redshift independence to higher z. We cannot rule out, however, potential changes in $M_{\rm halo} > 10^{10}$ M$_\odot$ haloes at $z > 11$, given the limitations in the number of massive haloes at high redshift in FIREbox^{HR}. Furthermore, we find that the SFE–halo mass relation is monotonically increasing with mass for low- to intermediate-mass haloes ($M_{\rm halo} \lesssim 10^{11}$ M$_\odot$). The SFE of galaxies residing in these haloes thus increases as the haloes themselves grow over cosmic time, i.e. the SFEs of individual galaxies tend to *decrease* with increasing redshift.

How can we understand that the average SFE–halo mass relation is approximately independent of redshift and only weakly evolving with halo mass for intermediate mass haloes? A speculative but intuitive explanation is based on the ansatz that the average SFR scales as

$$\mathrm{SFR} = \epsilon \frac{M_{\rm halo}}{t_{\rm ff}}, \tag{4}$$

where ϵ is a (mass dependent) efficiency factor and $t_{\rm ff} \approx 0.06\,H^{-1}(z)$ is the halo free fall time (Ferrara et al. 2023; Ferrara 2024). We can motivate this equation on dimensional grounds and via the equilibrium ansatz (Bouché et al. 2010; Davé, Finlator & Oppenheimer 2012) balancing gas inflow into galaxies with star formation and outflows from galaxies. In equilibrium, $\dot{M}_{\rm gas,in} = (1 - R + \eta)\,\mathrm{SFR}$, where $\dot{M}_{\rm gas,in}$ is the gas inflow rate into galaxies, R is the mass return fraction from evolving stellar populations in the instantaneous recycling approximation, and η is the mass loading factor of galactic outflows. Provided the gas inflow rate into galaxies scales proportional to $M_{\rm halo}/t_{\rm ff}$, we recover equation (4) with $\epsilon \propto 1/(1 - R + \eta) \sim 1/\eta$ for low-mass galaxies. The alternative choice $\dot{M}_{\rm gas,in} \propto \dot{M}_{\rm halo}$ is discussed further below.

In FIRE-2, gas ejection from high redshift galaxies of moderate mass is approximately ‘energy-driven’ ($\eta = V_{\rm halo}^{-2}$) (Pandya et al. 2021). Equivalently, we can equate the efficiency ϵ with the gas ejection efficiency (Dayal et al. 2014) which scales proportional to the square of the escape velocity in the mass range of interest. Physically, this scaling arises from (supernova) feedback expelling gas from galaxies thus reducing their star formation activity. Since $V_{\rm halo}^2 \propto (1+z)M_{\rm halo}^{2/3}$ and $H(z) \propto (1+z)^{3/2}$ at $z \sim 6 - 15$, equation (4) predicts

$$\mathrm{SFR} \propto M_{\rm halo}^{5/3}(1+z)^{5/2}. \tag{5}$$

The halo growth rate can be approximated as a power law of the halo mass and redshift (Krumholz & Dekel 2012),

$$\dot{M}_{\rm halo} \propto M_{\rm halo}^{1.14}(1+z)^{2.4}. \tag{6}$$

This expression is less accurate than the halo accretion rate formula by Behroozi & Silk (2015) used in this work but useful here for illustrating purposes.

Combining (5) with (6), and using our definition of the SFE as SFR/$\dot{M}_{\rm halo}$, we obtain

$$\text{SFE} \propto M_{\rm halo}^{0.53}(1+z)^{0.1}. \tag{7}$$

This simple model thus reproduces, at least qualitatively, the effective redshift independence of the SFE in FIREbox^{HR} and the weak scaling of SFE with halo mass. The weak halo mass dependence is a consequence of the near halo mass independence of the specific halo growth rate $\dot{M}_{\rm halo}/M_{\rm halo}$ and the weak halo mass scaling of $\epsilon \propto V_{\rm halo}^2$. The redshift independence of the SFE arises from the canceling of the various redshift scalings of $t_{\rm ff}$, $\dot{M}_{\rm halo}$, and ϵ. An alternative model assuming $\dot{M}_{\rm gas,in} \propto \dot{M}_{\rm halo}$ (Furlanetto et al. 2017) predicts SFE $\propto \epsilon \propto V_{\rm halo}^2 \propto M_{\rm halo}^{2/3}(1+z)$, i.e. a similar scaling of the SFE with halo mass but a slightly stronger evolution with redshift (~ 0.3 dex over $z \sim 6-14$).

3.3 The stellar mass–halo mass relation

The stellar mass–halo mass relation (SHMR) is a fundamental diagnostic of galaxy evolution that can in principle be constrained, e.g. via abundance matching (Kravtsov et al. 2004; Vale & Ostriker 2004; Behroozi, Conroy & Wechsler 2010; Moster et al. 2013) and empirical modelling (e.g. Moster et al. 2018; Behroozi et al. 2019). However, the scaling and redshift evolution of the SHMR at high z is still debated with some observational and theoretical constraints pointing towards strong redshift evolution (e.g. Harikane et al. 2016; Sun & Furlanetto 2016; Behroozi et al. 2019; Ceverino et al. 2024) and others suggesting weak or no evolution (e.g. Feldmann et al. 2017; Ma et al. 2018; Tacchella et al. 2018; Ma et al. 2019; Stefanon et al. 2021).

Fig. 5 plots the SHMR in FIREbox^{HR} for $M_{\rm halo} \sim 10^{8.2}$–$10^{11.2}$ M$_\odot$ haloes at $z \sim 6$–15. In agreement with previous results from FIRE-2 zoom-in simulations covering the $z \sim 5-12$ redshift range (Ma et al. 2018, 2019), the SHMR in FIREbox^{HR} does not strongly evolve at such early cosmic epochs. Weak trends include an increase in the stellar mass with redshift (especially at $z > 11$) in $M_{\rm halo} \sim 10^9$–10^{10} M$_\odot$ haloes and a slight decrease of the scatter with redshift at the lowest masses. The SHMR in FIREbox^{HR} at $z > 6$ differs significantly, however, from the SHMR in FIRE-2 simulations at low redshift (Hopkins et al. 2018). Because of the much flatter slope of the relation at $z > 6$ in FIREbox^{HR}, galaxies residing in haloes with $M_{\rm halo} < 10^{11}$ M$_\odot$ at early cosmic time have higher stellar masses compared with $z = 0$ galaxies in haloes of the same mass (Moster et al. 2013). The empirical model by Behroozi et al. (2019) also suggests a comparably flat slope, roughly in line with FIREbox^{HR}, but predicts an evolution in the normalization at $z > 6$. We caution that the SHMR at high z is yet to be fully constrained observationally (see e.g. Sun & Furlanetto 2016; Rodríguez-Puebla et al. 2017; Moster et al. 2018).

The redshift-combined relation between average stellar mass and halo mass in FIREbox^{HR} is well fit by a (broken) power law function, see equation (2) with SFE replaced by $M_{\rm star}$, with the following parameters: $A = -2.787, x_{\rm b} = 9.563, \Delta = 0.003, \alpha_1 = 0.617, \alpha_2 = 0.496$, i.e. it is close to a single power law with a slope of ~ 0.5–0.6. The scatter of the relation is ~ 0.2–0.4 dex and it increases weakly with decreasing halo mass over the considered mass range. The halo mass scaling of the scatter is approximated by a sigmoid function analogous to equation (3) with parameters $x_{\rm b} = 10.827$, $\Delta = 0.083$, $c_1 = 0.308$, and $c_2 = 0.165$.

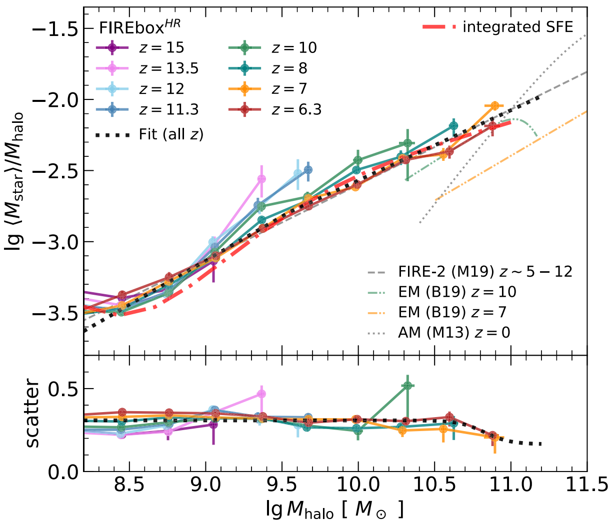

Figure 5. SHMR in FIREbox^{HR} at $z \sim 6$–15 (symbols and solid lines). The upper panel shows the average stellar mass per halo mass in bins of the latter, while the lower panel reports the standard deviation of lg $M_{\rm star}$ for each halo mass bin (the 'scatter'). Haloes that do not contain star particles (< 1 per cent of selected haloes with $M_{\rm halo} \sim 10^{8.5}$ M$_\odot$ at $z = 6.3$, and lower fractions at higher z) are excluded from the figure. Stellar masses are measured within radii of 3 proper kpc from the respective halo centre. The dashed line reproduces the SHMR for a suite of FIRE-2 zoom-in simulations reported by Ma et al. (2019) (M19). Double-dot–dashed lines show predictions of the UNIVERSEMACHINE empirical model by Behroozi et al. (2019) (B19) for $z = 7$ and $z = 10$. For comparison, we also include the abundance matching prediction for the SHMR in today's Universe by Moster, Naab & White (2013) (M13), which agrees well with FIRE-2 predictions at $z = 0$ (Hopkins et al. 2018). The SHMR for intermediate mass haloes does not appear to evolve strongly with redshift at $z > 6$ but differs from the SHMR in the local Universe. Dotted lines show fits to the FIREbox^{HR} results for the combined redshift range (see the text). The SHMR obtained from integrating the SFE–halo mass relation (red-dot–dashed line) agrees well with the actual SHMR in FIREbox^{HR}.

The SFE−halo mass relation is closely linked to the stellar mass−halo mass relation. If we assume that the change in stellar mass is $\dot{M}_{\rm star} = (1 - R)\,$SFR, where R is the mass return fraction in the instantaneous recycling approximation (e.g. Bouché et al. 2010; Lilly et al. 2013; Feldmann 2015), we obtain $\dot{M}_{\rm star} = (1 - R)\,$SFE $\dot{M}_{\rm halo}$ for an SFE defined in terms of SFR and halo growth rate $\dot{M}_{\rm halo}$. This equation can be easily integrated for a non-evolving SFE, resulting in

$$M_{\rm star}(M_{\rm halo}) = M_{\rm star,min} + (1-R)\int_{M_{\rm halo,min}}^{M_{\rm halo}} \text{SFE}(M'_{\rm halo}){\rm d}M'_{\rm halo}, \tag{8}$$

where $M_{\rm halo,min}$ is a chosen halo mass and $M_{\rm star,min} = M_{\rm star}(M_{\rm halo,min})$ is the average stellar mass of galaxies in haloes of mass $M_{\rm halo,min}$. Since the fit of the SFE−halo mass relation if obtained from haloes with masses $10^{8.2}$–$10^{11.2}$ M$_\odot$, we adopt $M_{\rm halo,min} = 10^{8.2}$ M$_\odot$ and set $M_{\rm star,min} = 3.5 \times 10^{-4}\, M_{\rm halo,min} \sim 10^{4.7}$ M$_\odot$. The alternative choice of setting $M_{\rm halo,min} = M_{\rm star,min} = 0$ lowers the predicted stellar mass in $\sim 10^{8.5}$ M$_\odot$ haloes by about 0.26 dex and has a negligible effect ($\lesssim 0.05$ dex) on the stellar mass in $M_{\rm halo} \gtrsim 10^9$ M$_\odot$ haloes.

In Fig. 5, we show the stellar fraction obtained by integrating the SFE in FIREbox^{HR} via equation (8) for a 5 Myr SFR averaging time (row 6 in Table 1). A short past averaging time is selected to reduce the bias in estimating the SFRs while the latter are quickly rising (e.g. Tacchella et al. 2018). Given the low masses and young stellar ages of many of the galaxies in our sample, we set $R = 0.1$ which corresponds to the return fraction of a 20 Myr old single stellar population with $Z \lesssim 0.007$ in the FIRE-2 model. The predicted SHMR from equation (8) closely matches the fit to the actual SHMR in FIREbox^{HR}, differing by less than ~ 0.1 dex.

One interesting aspect is the scaling of this predicted stellar fraction with halo mass at the massive end. Provided $M_{\rm star,min} \ll M_{\rm star}$, the halo mass scaling of the SFE is closely related to the scaling of the SHMR. Specifically, for a power-law SFE $\propto M_{\rm halo}^{\alpha}$ (with $\alpha > -1$), $M_{\rm star} \propto M_{\rm halo}^{1+\alpha}$ and the stellar fraction $f_{\rm star} = M_{\rm star}/M_{\rm halo} \propto M_{\rm halo}^{\alpha}$, i.e. the 'integrated SFE' $f_{\rm star}$ has the same scaling with halo mass as the instantaneous SFE. A broken power-law fit to the $f_{\rm star}$–halo mass relation obtained via equation (8) returns a high-mass slope of 0.33, in line with the expectation from the halo mass scaling of the SFE in FIREbox^{HR} (see Table 1). This slope is, however, lower than the high-mass slope (~ 0.50) of the actual $f_{\rm star}$–halo mass relation in FIREbox^{HR}.

Several factors could account for this difference in the high-mass slope. First, equation (8) does not consider the contribution of mergers to stellar mass growth, an effect that tends to increase with mass (e.g. Behroozi & Silk 2015; Behroozi et al. 2019) and potentially steepens the SHMR beyond what star formation alone would suggest. Secondly, the equation does not account for the scatter of the SFE at given halo mass, with the impact of the scatter likely depending both on its magnitude and the autocorrelation time of the SFR. Thirdly, the SFE is calculated by dividing the SFR of a halo of mass $M_{\rm halo}$ by an average halo growth rate of haloes of that mass, thereby ignoring variations in accretion rates at fixed halo mass. Lastly, the average halo growth rates in FIREbox^{HR} may differ slightly from those in Behroozi & Silk (2015), as the latter are based on simulations without baryonic effects (e.g. Sawala et al. 2013; Beltz-Mohrmann & Berlind 2021). For instance, removing the weak halo mass dependence of the specific halo growth rate at $z > 6$ would increase the high-mass slope of the SFE–halo mass relation by about 0.1, aligning it more closely with the SHMR slope in FIREbox^{HR}. Discrepancies in the average halo growth rates change the nominal SFE fitting parameters and the predictions of equation (8) but have otherwise no impact on this work's predictions as the latter involve the product of the SFE and the average halo growth rate, thus depending only on the underlying SFR or corresponding UV luminosity.

3.4 A theoretical model for the UV LF and density at $z > 6$

As discussed in Section 3.1, FIREbox^{HR} predicts UV luminosity densities at $z > 10$ in good agreement with observational data by *JWST*. In this section, we introduce a simple model that provides a theoretical explanation for this result. Our approach builds on the ideas of previous work (Trenti et al. 2010; Tacchella et al. 2013, 2018; Mason et al. 2015; Furlanetto et al. 2017; Harikane et al. 2022; Sabti et al. 2022; Ferrara et al. 2023; Lovell et al. 2023) but differs in its use of an SFE–halo mass relation derived from a cosmological, hydrodynamical simulation. Given that the FIRE-2 physics model is not explicitly tuned to specific observables, this model is thus theoretical, and not empirical, in nature. This theoretical framework demonstrates that the gradual evolution of the UV luminosity density can be directly attributed to the baryonic processes, including stellar feedback and gas accretion, that take place in galaxies at high redshifts.

The core component of the model is the SFE–halo mass relation predicted by FIREbox^{HR}. Since we are interested in estimating the *observed* UV luminosity density $\mathcal{L}$, we define the SFE $\mathcal{S}$ as the ratio between $\mathcal{L}$, converted to units of SFR by multiplication with a constant conversion factor κ, and the averaged halo accretion rate[7] $\dot{M}$, i.e.

$$\mathcal{S} = \kappa \mathcal{L}/\dot{M}. \tag{9}$$

Analogous definitions may be used to define $\mathcal{S}$ in terms of, e.g. the intrinsic UV luminosity density or the actual SFR density. The function $\dot{M}$ measures the averaged and smoothed accretion rate for haloes of mass M at redshift z (Behroozi & Silk 2015). We adopt the constant $\kappa = 1.15 \times 10^{-28}\, M_{\odot}\,{\rm yr}^{-1}\,{\rm erg}^{-1}\,{\rm s\,Hz}$ as the conversion factor between luminosity and SFR (Madau & Dickinson 2014). However, this choice has no impact on the model predictions because the same factor is used to constrain the average SFE–halo mass relation from the UV luminosities of FIREbox^{HR} galaxies.

We model the SFE of galaxies residing in haloes of mass M at redshift z as a log-normally distributed random variable, i.e.

$$\begin{aligned} &\mathcal{S} \sim {\rm Lognormal}(\mu, \sigma^2), \text{ with} \\ &\mu = \ln\langle \mathcal{S}\rangle - \sigma^2/2, \\ &\sigma = {\rm std}(\lg \mathcal{S})\, \ln 10, \end{aligned} \tag{10}$$

where $\langle \mathcal{S}\rangle$ denotes the average SFE and ${\rm std}(\lg \mathcal{S})$ is the scatter of the SFE in dex. Both are inferred directly from FIREbox^{HR} and they may, in principle, vary with both M and z. An advantage of the above parametrization, in contrast to alternatives based on, e.g. the median SFE (Shen et al. 2023b), is that it cleanly distinguishes between changes to the average SFE and changes to the scatter of the SFE. This is useful because absent a UV magnitude limit, the cosmic UV luminosity density depends on the *average* SFE–halo mass relation (see below) and not on its scatter.

It follows from equation (9) that $\mathcal{L}$ is also a lognormally distributed random variable with $\langle\mathcal{L}\rangle = \langle \mathcal{S}\rangle \dot{M}/\kappa$. In contrast, the rest-frame UV magnitude defined as

$$\mathcal{M} = {\rm Mag}(\mathcal{L}) \equiv -2.5 \lg\left(\frac{\mathcal{L}}{4\pi\,(10\,{\rm pc})^2}\right) - 48.6 \tag{11}$$

is normally distributed at a given M and z with mean and standard deviation given by

$$\langle\mathcal{M}\rangle = {\rm Mag}(e^{\mu}\dot{M}/\kappa) \text{ and } {\rm std}(\mathcal{M}) = \frac{2.5}{\ln 10}\sigma. \tag{12}$$

According to the model, the cosmic UV luminosity density in galaxies brighter than some limit luminosity l is

$$\begin{aligned} \rho_{\rm UV}(z) &= \int_0^{\infty} {\rm d}M \frac{{\rm d}n}{{\rm d}M}(M, z) \int_l^{\infty} p(\mathcal{L} = L | M, z) L\, {\rm d}L \\ &= \int_0^{\infty} {\rm d}M \frac{{\rm d}n}{{\rm d}M} \langle\mathcal{L}\rangle\, \Phi\left(\frac{\ln(\langle\mathcal{L}\rangle/l) + \sigma^2/2}{\sigma}\right) \\ &= \frac{1}{\kappa}\int_{-\infty}^{\infty} {\rm d}\lg M \frac{{\rm d}n}{{\rm d}\lg M} \dot{M} \langle\mathcal{S}\rangle_{\rm eff}. \end{aligned} \tag{13}$$

In the equation above, Φ is the cumulative distribution function of the standard normal distribution, p is the probability density function (pdf) of $\mathcal{L}$, dn/dM is the halo mass function, and $\langle\mathcal{S}\rangle_{\rm eff}$ is an effective

---

[7] In this section, we denote halo mass as M instead of $M_{\rm halo}$ for notational simplicity.

SFE defined by

$$\langle \mathcal{S} \rangle_{\rm eff} = \langle \mathcal{S} \rangle \, \Phi \left(\frac{\ln(\langle \mathcal{S} \rangle \dot{M}/(\kappa l)) + \sigma^2/2}{\sigma} \right). \qquad (14)$$

The effective SFE is $\langle \mathcal{S} \rangle/2$ if $\langle \mathcal{S} \rangle = \kappa l \exp(-\sigma^2/2)/\dot{M}$. In case of vanishing scatter ($\sigma \to 0$), $\langle \mathcal{S} \rangle_{\rm eff} = \langle \mathcal{S} \rangle$ if $\langle \mathcal{S} \rangle > \kappa l/\dot{M}$ and $\langle \mathcal{S} \rangle_{\rm eff} = 0$ otherwise. In case of a vanishing limit luminosity ($l \to 0$), $\langle \mathcal{S} \rangle_{\rm eff} = \langle \mathcal{S} \rangle$ and $\rho_{\rm UV}(z)$ is independent of σ.

We similarly obtain the number density of galaxies brighter than some luminosity l or magnitude m as

$$n(>l, z) = \int_0^\infty \mathrm{d}M \frac{dn}{\mathrm{d}M} \, \Phi \left(\frac{\ln(\langle \mathcal{L} \rangle / l) - \sigma^2/2}{\sigma} \right), \text{ and}$$

$$n(<m, z) = \int_0^\infty \mathrm{d}M \frac{\mathrm{d}n}{\mathrm{d}M} \, \Phi \left(\frac{m - \langle \mathcal{M} \rangle}{\mathrm{std}(\mathcal{M})} \right). \qquad (15)$$

The UV LF predicted by the model is

$$\begin{aligned} \phi(m, z) &= \frac{\mathrm{d}n(<m, z)}{\mathrm{d}m} = np(\mathcal{M} = m|z) \\ &= \int_0^\infty \mathrm{d}M \frac{dn}{\mathrm{d}M} p(\mathcal{M} = m|M, z), \end{aligned} \qquad (16)$$

where p is the pdf of $\mathcal{M}$ with parameters given by (12). We evaluate the integrals in equations (13, 15, 16) numerically with halo mass functions (HMFs) provided by the HMF module for Python (Murray, Power & Robotham 2013; Murray 2014). Appendix D provides an analytical solution of equation (16) in the case of a power-law HMF and SFE–halo mass relation.

The discussion so far has been quite general. The non-evolving SFE model makes the additional assumption, based on the results of the previous sections, that the average SFE and its scatter in haloes of a given mass do not vary with redshift at $z > 6$.

Fig. 6 compares the evolution of the (dust-attenuated) UV luminosity density in FIREbox^{HR}, for $M_{\rm UV} < -17$, with the predictions of the theoretical model under the assumption of a non-evolving SFE–halo mass relation. To this end, we use the SFE–halo mass relation inferred directly from FIREbox^{HR} for dust-attenuated UV luminosities and halo mass binning. Specifically, the average SFE–halo mass relation is approximated by a broken-power law form, see equation (2), and the halo mass dependence of the scatter follows equation (3), with fit parameters as provided in the first row of Tables 1 and 2.

For a fairer comparison that accounts for the finite box size of the simulation, we calculate the UV luminosity density not via integrating equation (13) but by sampling. Specifically, for each simulated halo of mass M and z, we first draw a UV luminosity from the appropriate lognormal distribution (see equations 9 and 10). Next, we add the luminosities of all haloes with a magnitude brighter than –17 and divide the sum by the simulation volume. By repeatedly resampling with multiple redraws, we estimate the uncertainty of the UV luminosity density in the simulation volume, attributable to the scatter in the SFE–halo mass relation. This uncertainty estimate does not include any variance due to fluctuations in the halo numbers and is thus generally smaller than the uncertainty in FIREbox^{HR} obtained via bootstrapping.

As the figure demonstrates, the theoretical model accurately captures the evolution of the cosmic UV luminosity density in FIREbox^{HR}. The simulation results are within the 95 per cent confidence interval of the model's predictions. Given that the uncertainties in the theoretical model stem from the scatter in the SFE–halo mass relation, we conclude that the fluctuations of the UV luminosity with redshift found in FIREbox^{HR} can be attributed to this variability. This includes the data point at $z \sim 15$, where a strong burst in star formation just prior to $z = 15$ elevates the UV luminosity density in the simulation snapshot. Moreover, the simulation results are entirely consistent (often within their 68 per cent confidence interval obtained via bootstrapping) with the expectation from the theoretical model. We conclude that the theoretical model introduced in this section reproduces the UV luminosity density predicted by FIREbox^{HR} and matches corresponding observational constraints at $z > 6$.

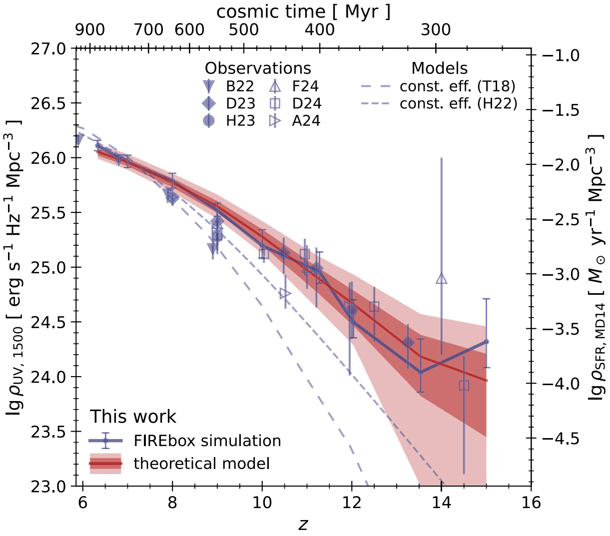

Figure 6. Evolution of the UV luminosity density down to a limiting observed rest-frame magnitude of −17 as predicted by FIREbox^{HR} (blue solid line and error bars) and by a theoretical model with a non-evolving SFE–halo mass relation inferred from the simulation (red line and shaded areas). The red line shows the UV luminosity density in galaxies brighter than −17 as predicted by the theoretical model for the same halo mass distribution as in FIREbox^{HR}, while dark and light shaded areas indicate how the scatter in the SFE affects the UV luminosity in the given volume at the 68 and 95 per cent confidence level. Uncertainties (68 per cent confidence level) of the FIREbox^{HR} predictions are calculated via bootstrapping and account for both the scatter in SFE and variations in halo numbers. Long and short dashed lines reproduce the predictions of empirical models by Tacchella et al. (2018) and Harikane et al. (2022), and large symbols with error bars show observational estimates by Bouwens et al. (2022), Donnan et al. (2023a, b, 2024), Harikane et al. (2023), Adams et al. (2024), and Finkelstein et al. (2024). The theoretical model reproduces the evolution of the UV luminosity density found by FIREbox^{HR} within the uncertainties.

3.5 Implications of a non-evolving SFE–halo mass relation: UV luminosities of galaxies at the EoR and Cosmic Dawn

The theoretical model introduced in the previous section allows us to study the evolution of the UV luminosity density and UV LF during reionization and late Cosmic Dawn without being limited by simulation volume. To integrate equations (13, 16), we use the halo number densities provided by HMF version 3.4.4 for a Planck 2018 cosmology (Aghanim et al. 2020) with $h = 0.6766$, $\Omega_0 = 0.3111$, $\Omega_{\rm b} = 0.04897$, and $\sigma_8 = 0.8102$, a CAMB transfer function with[8] $k_{\rm max} = 150$, and the Tinker et al. (2008) halo mass

---

[8] Setting $k_{\rm max}$ to a sufficiently large value is critical as HMF's default setting, at least in the code version we used, overestimates (e.g. by about 0.5 dex for $10^8\,M_\odot$ haloes at $z = 10$) the number density of low-mass haloes at high redshift.

function with the Behroozi et al. (2013) extension to high redshift. To approximately account for the impact of baryonic effects on the halo mass (e.g. Sawala et al. 2013; Cui, Borgani & Murante 2014; Velliscig et al. 2014; Schaller et al. 2015; Beltz-Mohrmann & Berlind 2021), we reduce the halo masses provided by HMF by 0.07 dex, i.e. $M_{\rm halo} \rightarrow M'_{\rm halo} = 10^{-0.07} M_{\rm halo}$ and $n(> M_{\rm halo}) \rightarrow n'(> M'_{\rm halo}) = n(> M_{\rm halo})$. For the fiducial set up, we adopt the non-evolving SFE–halo mass relation with a mass-dependent scatter and with parameters provided in Tables 1 and 2 for dust-attenuated UV luminosities and halo mass binning. Variations of this set-up will be discussed in the text when needed. We stress that some model predictions involve extrapolations of the non-evolving SFE–halo mass ansatz to lower halo masses and higher redshifts than reliably probed by FIREbox^{HR}. Additionally, the predictions assume no fundamental changes in baryonic physics and star formation processes at high z, such as contributions from Population III stars (see Section 3.7).

The left panel of Fig. 7 presents the UV luminosity density and UV LFs predicted by the theoretical model for $z \sim 6 - 20$. The model accurately captures the observed evolution of the UV luminosity density over $z \sim 6 - 13.5$. Notably, $\log \rho_{\rm UV}$ does not evolve linearly with redshift at $z \geq 6$ (cf. Ceverino et al. 2024) showing instead a steeper decline in UV luminosity density towards higher redshifts. For instance, the UV luminosity density at $z = 16$ (for a limiting magnitude of -17) is predicted to be about two orders of magnitude lower than at $z = 11$, highlighting a challenge for observational studies targeting galaxies at those redshifts (e.g. Robertson et al. 2024). Extending this model speculatively to $z = 20$ suggests a further reduction in luminosity density by an additional two orders of magnitude. Recent tentative observational evidence may suggest a sudden steepening of the UV luminosity density evolution between $z \sim 12.5$ and 14.5 (Robertson et al. 2024; Donnan et al. 2024). While a steeper evolution at higher z is in line with our findings, our model predicts a gradual steepening over $z \sim 6 - 15$, not a sudden transition between two separate evolutionary regimes.

Constraining the evolution of the cosmic UV luminosity density at high z is of critical importance for the large number of experiments aiming to detect and characterize the distribution of neutral hydrogen ($\rm H_I$) during Cosmic Dawn and reionization [e.g. HERA (Deboer et al. 2017; Abdurashidova et al. 2022); LOFAR (Patil et al. 2017; Mertens et al. 2020); NenuFAR (Munshi et al. 2024); MWA (Barry et al. 2019)], including the future Square Kilometer Array Observatory (SKAO; Mellema et al. 2013; Koopmans et al. 2015). Ly α radiation emitted from galaxies during these early times ($z \lesssim 20$) can decouple the spin temperature of $\rm H_I$ from the CMB background, rendering neutral hydrogen accessible to observations via its 21 cm line (Wouthuysen 1952; Field 1958). Provided that faint, metal-poor galaxies are the dominant Ly α contributors, detectability of the 21 cm line requires a cosmic UV luminosity density exceeding $\rho_{\rm UV,21cm}(z) \sim 10^{24.5}(18/(1+z))^{1/2}\,{\rm erg\,s^{-1}\,Mpc^{-3}\,Hz^{-1}}$ (Madau 2018).

Our theoretical model predicts that, for $M_{\rm UV,lim} = -12$, $\rho_{\rm UV}(z)$ exceeds $\rho_{\rm UV,21cm}(z)$ only at $z \lesssim 14$. The tentative detection of a 21 cm signal corresponding to $z \sim 16 - 19$ reported by the EDGES collaboration (Bowman et al. 2018) would thus be at odds with the predictions of our theoretical model. We note that a subsequent measurement of the radio sky in the same band (55–85 MHz) ruled out an astrophysical origin of the EDGES signal with 95 per cent confidence (Singh et al. 2022). Instead, various measurement and instrument systematics have been suggested as culprits (Hills et al. 2018; Bradley et al. 2019; Singh & Subrahmanyan 2019; Sims & Pober 2020; Bevins et al. 2021). Our predictions for the detectability of an EDGES-like signal in 21 cm are thus much more pessimistic than expectations based on linearly extrapolating $\log \rho_{\rm UV}(z)$ as function of z from $z \sim 4 - 9$ to Cosmic Dawn (Madau 2018; Hassan et al. 2023, see also Bera et al. 2023). However, the UV luminosity density at higher redshift could potentially be boosted by a larger contribution of Population III stars that are not included in our model (e.g. Muñoz et al. 2022). In addition, low-mass ($M_{\rm halo} < 10^8\,M_\odot$) haloes could provide a significant contribution to the cosmic star formation activity before reionization (Barkana & Loeb 2000; Harikane et al. 2023).

The right panel of Fig. 7 shows the number density of galaxies with rest-frame UV magnitudes brighter than a limiting value, $M_{\rm UV,lim}$, as predicted by our theoretical model. The predicted number densities match well observational estimates derived by integrating UV LFs down to $M_{\rm UV,lim} = -17$. Deeper observations would dramatically increase the number density of detectable galaxies, e.g. by one order of magnitude when going from $M_{\rm UV,lim} = -17$ to $M_{\rm UV,lim} = -14$ at $z = 6$. In contrast, the UV luminosity density is much less sensitive to the UV magnitude limit, increasing by only 0.3 dex at $z = 6$ for the same change in $M_{\rm UV,lim}$.

The UV LFs predicted by the theoretical model are also in approximate agreement with observations, see Fig. 8. Deviations at the luminous end partly arise due to the lack of massive haloes in FIREbox^{HR} (given its modest box size) needed to constrain the high-mass behaviour of the SFE–halo mass relation. In addition, it is possible that FIREbox^{HR} underestimates the scatter in the SFE in more massive haloes. A larger scatter would indeed increase the number density of UV luminous galaxies as shown by the figure (see also Sun et al. 2023c). For instance, an SFE scatter of 0.6 dex (compared with the lower ~ 0.3 dex found in FIREbox^{HR} for $M_{\rm halo} \sim 10^{10} - 10^{11}\,M_\odot$ haloes) would be sufficient to match the reported UV LF at $z = 12$ by Harikane et al. (2023). However, applying the same scatter to $z = 10$ would then lead to an overprediction of the observed UV LFs at this earlier redshift (Donnan et al. 2023a). The dependence of the UV LFs on the scatter is further discussed in Appendix D. A peculiar feature of the model with mass-dependent scatter is that it introduces a much more pronounced change in slope of the UV LF at moderately faint luminosities (e.g. near -16.5 at $z = 6$) compared to the model with mass-independent scatter.

We fit the predicted UV LFs both with a modified Schechter function, see Section 4.3 in Bouwens et al. (2017), and a double power law (e.g. Harikane et al. 2022). The modified Schechter function includes a multiplicative term $10^{-0.4\delta(M_{\rm UV}+16)^2}$ to model a roll-over of the LF at the faint end. The fitting parameters are provided in Appendix E. While not expected a priori, our model predictions are well fit by either functional form. In either case, and independently of the chosen scatter of the SFE–halo mass relation, fits to the UV LFs confirm the visually apparent decrease in the overall normalization and the steepening in the faint end slope with increasing redshift.

We now compare the parameters from the modified Schechter fit to the UV LFs predicted by the theoretical model with mass-dependent scatter to those derived from the observational analysis by Bouwens et al. (2022). At $z = 6$, we find decent agreement with a characteristic magnitude $M^*_{\rm UV}$ that is about 0.3 mag lower, a similar normalization, and a faint end slope (-2.0 versus -1.9). At $z = 8$, the agreement is less favourable with the theoretical model predicting an $M^*_{\rm UV}$ that is about 0.8 mag too faint and a slope that is slightly too shallow (-2.0 in the theoretical model versus -2.2 found by Bouwens et al. 2022). The theoretical model is in somewhat better agreement with the observational results by Bouwens et al. (2015).

The roll-over parameter obtained by the fit is positive ($\delta \sim 0.09 - 0.17$), suggesting that the UV LF deviates from a traditional Schechter function at lower luminosities. This is further indicated by the turn-over magnitude $M_{\rm UV,T} \equiv -16 - 0.5(1+\alpha)/\delta$, which

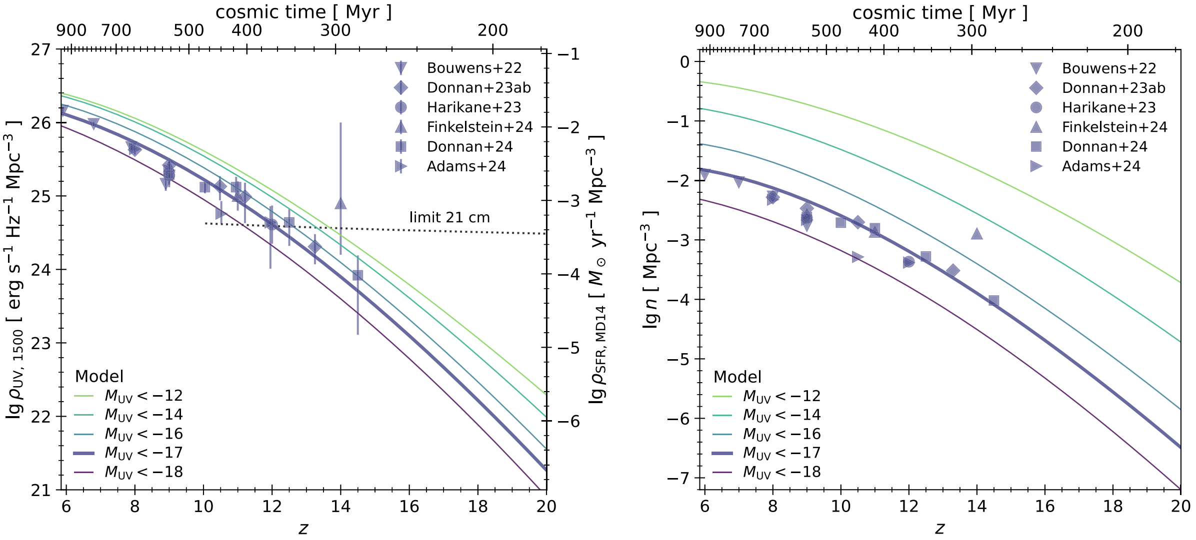

Figure 7. Predictions of the theoretical model for the cosmic UV luminosity density (left panel) and the corresponding galaxy number density (right panel) at $z \sim 6 - 20$. The predictions (shown by solid lines) assume a non-evolving SFE–halo mass relation with mass-dependent scatter with parameters provided in Tables 1 and 2, a Tinker et al. (2008) halo mass function with the Behroozi, Wechsler & Conroy (2013) extension to high redshift, and Planck 2018 cosmology (Aghanim et al. 2020). Line colours indicate the adopted limiting magnitude (see legend). Symbols show observational estimates of the UV luminosity density and their uncertainties for $M_{\rm UV,lim} = -17$ (left panel) and galaxy number densities obtained by integrating the reported UV LFs to $M_{\rm UV,lim} = -17$ (Bouwens et al. 2022; Harikane et al. 2023; Donnan et al. 2023a, b, 2024; Adams et al. 2024; Finkelstein et al. 2024). The dotted line in the left panel is the UV luminosity density needed for a 21 cm absorption signal in the 'minimal coupling' regime (Madau 2018). The UV luminosity density and number density predicted by the theoretical model for $M_{\rm UV,lim} = -17$ matches current observations and shows a steeper evolution at the highest redshift.

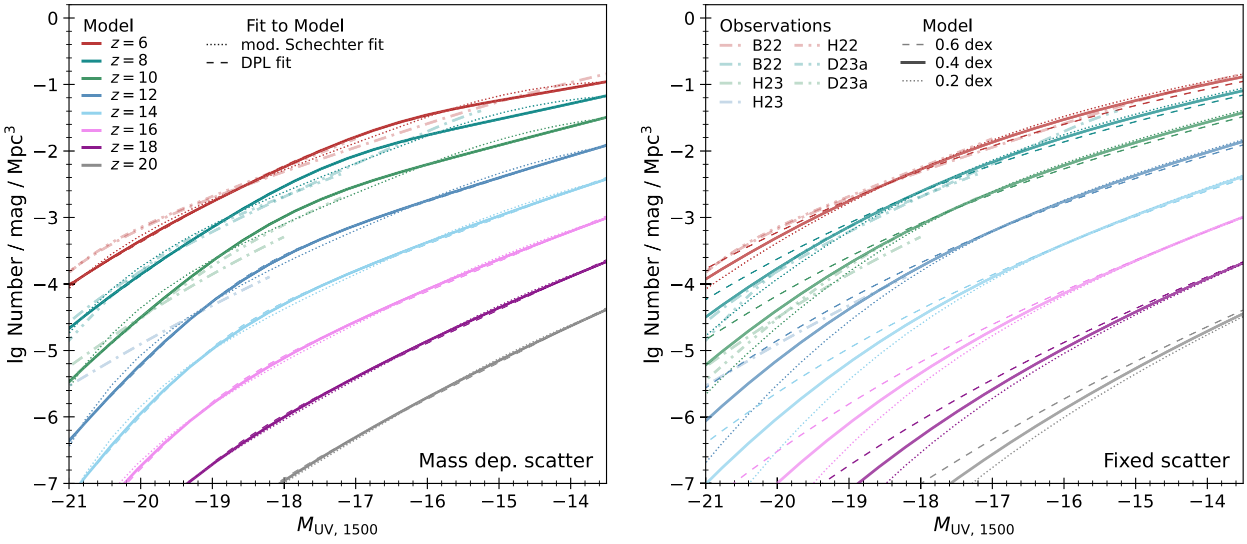

Figure 8. Predictions of the theoretical model for the UV LFs at $z \sim 6 - 20$. All predictions assume a non-evolving SFE–halo mass relation, a Tinker et al. (2008) halo mass function with the Behroozi extension to high redshift (Behroozi et al. 2013), and Planck 2018 cosmology (Aghanim et al. 2020). Solid lines of various colours indicate the model predictions for different redshifts. Dot–dashed and double dot–dashed lines show observational estimates of the UV LF at $z \sim 6 - 12$ (Bouwens et al. 2022; Harikane et al. 2022, 2023; Donnan et al. 2023a). Left: Predictions for the fiducial model with a mass-dependent scatter (see Table 2). Dotted lines (dashed lines) show fits of the model UV LFs to a modified Schechter (a double power law) function (Bouwens et al. 2017; Harikane et al. 2022). While both fitting functions describe the UV LFs of the theoretical model reasonably well, a double power law provides a significantly better fit, especially at $z \leq 14$. Right: Similar to left panel but for a mass-independent scatter of the SFE–halo mass relation. Solid (dotted, dashed) lines correspond to a scatter of 0.4 (0.2, 0.6) dex. A larger scatter increases the number density of UV luminous galaxies. In addition to a rapid decline in overall normalization, the theoretical model predicts a steepening in the faint-end of the UV LFs towards higher redshift. Fitting parameters for a modified Schechter function and double power law are provided in Appendix E.

increases with redshift – from −13.2 at $z = 6$ to −11.2 at $z = 12$. These findings suggest that observations at $z \lesssim 6$ are likely better suited to identifying deviations from a traditional Schechter function.

While a modified Schechter function is able to approximate the UV LF reasonably well, we find that the double power law generally provides a superior fit (see the left panel of Fig. 8). The positive value of δ may thus reflect a limitation on the fitting function rather than a true turn-over in the UV LFs at low luminosities. Moreoever, the double power law fit reveals that the faint end appears to have a slope that is shallower than the one suggested by the modified Schechter fit. Specifically, at $z = 6$, the faint end slope is $\alpha = -1.4$ (compared to $\alpha = -2.0$ for the modified Schechter fit), and $\alpha = -1.9$ at $z = 12$ (versus $\alpha = -2.1$).

The faint end slope of the UV LF, α, is directly related to a combination of the low-mass slope α_1 of the SFE–halo mass relation, the slope α_M of the halo mass function over the relevant halo mass range, and the slope γ of the halo growth rate. Specifically,

$$\alpha = \frac{1 + \alpha_M}{\alpha_1 + \gamma} - 1, \tag{17}$$

assuming that the SFE, halo mass function, and halo growth rate follow power law relations with halo mass, and the scatter of the SFE is mass-independent, see Appendix D. For a given ΛCDM cosmology, the faint end slope of the UV LF thus directly probes the low-mass slope of the SFE–halo mass relation. Alternatively, if the SFE–halo mass relation can be determined independently, then the faint end slope can serve as a constraint on the low-mass end of the halo mass function. In particular, if the SFE–halo mass relation is redshift independent, as suggested by FIREbox^{HR}, the observed redshift evolution of α (e.g. Bouwens et al. 2012; Finkelstein et al. 2015; Bouwens et al. 2022) can be explained by the steepening (i.e. the decrease) of the slope α_M of the halo mass function for haloes corresponding to moderately faint galaxies ($M_{\rm UV} \sim -18$ to -16) with increasing redshift.

So far, we discussed model predictions mainly for a specific SFE–halo mass relation obtained from FIREbox^{HR}. In Fig. 9, we address the question how sensitively the UV luminosity density and LFs depend on the parameters of the SFE–halo mass relation. This analysis will also allow us to better understand the comparably gradual evolution of the UV luminosity density with cosmic time in our model. Specifically, we explore the effect of varying (i) the overall normalization by ± 0.3 dex, (ii) the low-mass slope α_1 by ± 0.3, (iii) the high-mass slope α_2 by ± 0.3, (iv) the log pivot mass $x_{\rm b}$ by ± 0.3, and (v) the scatter of the SFE–halo mass relation by ± 0.2 dex. Each of these variations is much larger than the statistical uncertainty (< 0.1) in the corresponding fit parameter reported in Tables 1 and 2.

A change in the normalization of the SFE–halo mass relation by 0.3 dex has the expected effect of shifting the UV LFs horizontally by a corresponding amount (0.75 magnitudes). The UV luminosity density in galaxies brighter than -17 is affected at the level of about 0.4 dex at $z \sim 6$–8, and 0.5 dex at $z \sim 13 - 15$, i.e. the change is not a strong function of redshift. The models by Tacchella et al. (2018) and Harikane et al. (2022) predict UV luminosity densities that match observations at $z \sim 6 - 7$ but are $1.2 - 2.4$ dex lower than observations at $z \sim 12$. Bringing these models in agreement with observations would thus require boosting the SFE of the galaxies responsible for the cosmic UV luminosity by a redshift dependent factor. Hence, a change in the normalization of a non-evolving SFE–halo mass relation alone cannot explain the observed gradual evolution of the UV luminosity density.

The value of the low-mass slope α_1 has little impact on the UV luminosity density of galaxies brighter than -17 at $z < 12$ although it changes the faint end slope of the UV LFs. The luminosity density is not strongly affected because, at $z < 12$, $M_{\rm UV} = -17$ galaxies reside typically in haloes more massive than the pivot mass. The faint end of the UV LF becomes shallower with a steeper (i.e. larger) α_1 because increasing α_1, while keeping the normalization fixed at the pivot mass, reduces the SFE and UV luminosity of low-mass haloes. Generally, the faint end slope gains in importance with increasing redshift as the average halo mass per given UV magnitude decreases, see appendix B. However, while varying α_1 affects the UV luminosity density at $z > 12$, these changes are comparably moderate. Hence, we do not attribute the gradual evolution of the UV luminosity density in FIREbox^{HR} to this parameter.

Instead, the figure shows that the high-mass slope α_2 of the SFE–halo mass relation significantly affects the evolution of the UV luminosity density of galaxies brighter than -17 at $z \sim 6 - 10$. In addition, the slope also strongly influences the shape of the bright end of the UV LFs. Provided we keep the normalization of the relation fixed at the pivot mass ($M_{\rm halo} \sim 10^{9.5}\,{\rm M}_\odot$), a steeper α_2 results in a larger SFE in haloes more massive than the pivot mass. A steeper slope thus increases the cosmic UV luminosity density as well as the number density of UV bright galaxies. Hence, provided we have an appropriate normalization of the SFE–halo mass relation such that $\rho_{\rm UV}$ matches observations at some lower redshift (e.g. for $z = 6$), a shallower (steeper) high-mass slope leads to a shallower (steeper) evolution of the cosmic UV luminosity density. Indeed, the slope of the SFE–halo mass relation predicted by FIREbox^{HR} for galaxies in $M_{\rm halo} = 10^{9.5} - 10^{10.5}\,M_\odot$ haloes is much lower than the slope by Harikane et al. (2022) extrapolated to the same mass regime while approximately matching at the high-mass end ($M_{\rm halo} \sim 10^{11}\,{\rm M}_\odot$). FIREbox^{HR} thus predicts a much higher SFE for galaxies that dominate the cosmic UV luminosity density compared with Harikane et al. (2022). We note that the UV luminosity above which the LF is significantly affected by a change in high-mass slope increases with increasing redshift (from about -17 at $z = 6$ to -19 at $z = 14$). Consequently, the impact of α_2 on the UV luminosity density decreases with increasing z and the theoretical model always predicts a rather steep evolution of $\rho_{\rm UV}$ at the highest redshifts.

Varying the pivot mass, i.e. the mass separating the low-mass and high-mass regime of the broken-power law fit to the SFE–halo mass relation in FIREbox^{HR}, has a similar effect as changing the low-mass slope. Increasing $x_{\rm b}$, while keeping the normalization fixed, reduces the number density of haloes above the pivot mass and thus lowers the UV luminosity density. This effect is more pronounced at higher z when a larger proportion of the UV luminosity density arises from haloes near the pivot mass.

Finally, the figure analyses how scatter in the SFE–halo mass relation, and the corresponding variability in the UV magnitudes, affects the cosmic UV luminosity density and the UV LFs. Specifically, we vary the mass-dependent scatter by ± 0.2 dex finding that the cosmic UV luminosity density is largely insensitive to this scatter. This finding is in qualitative agreement with a recent study by Gelli, Mason & Hayward (2024) who concluded that scatter alone does not explain the high UV luminosity density at $z > 12$. Scatter in the SFE–halo mass relation has a significant impact, however, on the bright end of the UV LFs. As discussed before, a higher UV variability boosts the number density of UV bright galaxies given their much lower number density compared to faint ones. However, unless the scatter is increased to a value much larger than found in FIREbox^{HR}, the number density of galaxies which dominate the cosmic UV luminosity density is only weakly affected. For a further discussion of the importance of the scatter on the UV LF, see Appendix D.

Our finding contrasts with alternative models that aim to explain the relatively shallow evolution of the UV luminosity density at high z with a large and redshift-dependent scatter of the SFE (e.g. Shen et al. 2023b). We parametrize the SFE–halo mass relation in terms of both the mean relation and its log-normal scatter. As discussed in Section 3.4, an alternative approach is to parametrize the SFE–halo mass relation in terms of the *median* relation and its scatter.

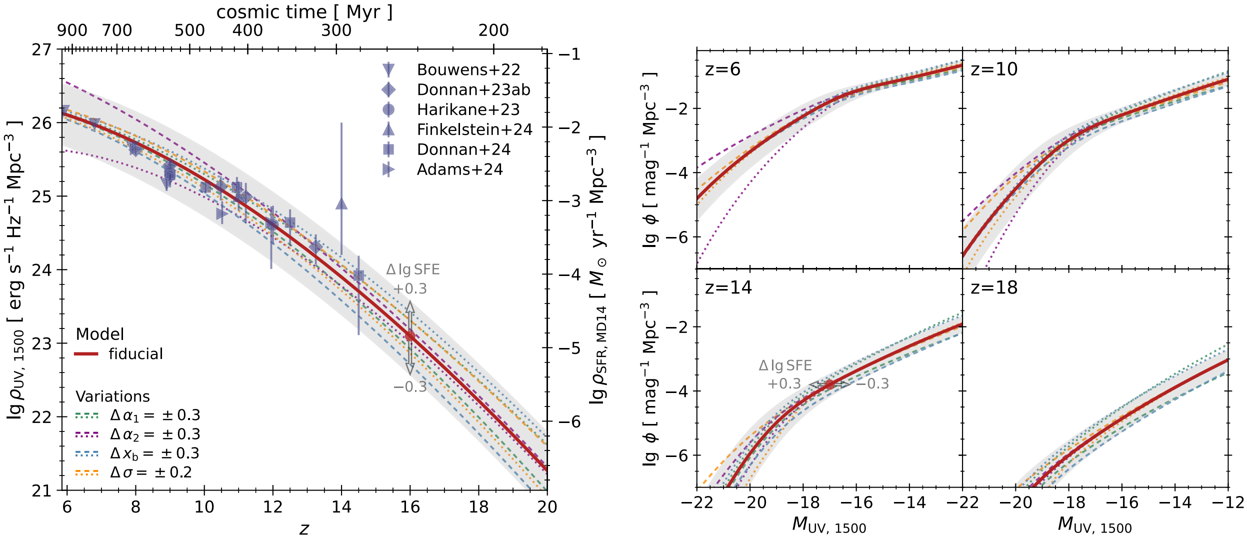

Figure 9. The effect of varying the fit parameters of the non-evolving SFE model on the predicted UV density (left panel) and the UV LF (right four panels). Only galaxies with a rest-frame UV magnitude brighter than −17 are included in the UV luminosity density. In each panel, model predictions for the fiducial set of parameters are shown by solid red lines. Predictions for different low-mass (α_1) and high-mass (α_2) slopes of the SFE–halo mass relation are indicated by green and purple lines while a change in the scatter (σ) of the SFE–halo mass relation is shown by orange lines. In each case, dashed lines (dotted lines) show the result for an increase (decrease) of the corresponding parameter. The grey-shaded region illustrates how the model predictions would change if the overall normalization of the SFE–halo mass relation is increased or decreased by up to 0.3 dex. Varying the scatter of the SFE–halo mass relation between 0.2 and 0.6 dex, a range consistent with the scatter predicted by FIREbox^{HR} (see the bottom right panel of Fig. 4), has only a weak effect on the UV LF or UV luminosity density. Instead, the shape of the UV LF at low and high luminosities is largely controlled by the low-mass and high-mass slope of the SFE–halo mass relation. A change in the high-mass slope also has a noticeable impact on the UV luminosity density at $z < 10$. In contrast, at $z > 10$, the UV luminosity density of galaxies brighter than −17 is primarily determined by the SFE in $M_{\mathrm{halo}} \sim 10^9 - 10^{10}\,M_\odot$ haloes, i.e. by the SFE of haloes near the pivot mass of the SFE–halo mass parametrization (see Table 1).

However, for a lognormally distributed SFE, increasing the scatter while holding the median SFE fixed results in an increase in the mean SFE. A scatter that grows with redshift, while maintaining a fixed median SFE–halo mass relation, consequently raises the normalization of the average SFE–halo mass relation and causes a weaker decline in UV luminosity density with redshift. In contrast, our theoretical model successfully matches the observed evolution of the UV luminosity density without requiring an explicit redshift dependence of the average SFE–halo mass relation.

To better understand the comparably shallow evolution of the UV LF at $z \lesssim 12$, we analyse how haloes of different mass contribute to the cosmic UV luminosity density for different UV magnitude limits. According to equation (13), the luminosity density per dex in halo mass

$$\frac{\mathrm{d}\rho_{\mathrm{UV}}}{\mathrm{d}\lg M_{\mathrm{halo}}} = \left[\dot{M}_{\mathrm{halo}} \frac{\mathrm{d}n}{\mathrm{d}\lg M_{\mathrm{halo}}}\right] \langle \mathcal{S} \rangle_{\mathrm{eff}} \frac{1}{\kappa} \tag{18}$$

is proportional to the halo mass growth rate density per dex in halo mass (the term in brackets) and the effective SFE $\langle \mathcal{S} \rangle_{\mathrm{eff}}$. While the former is related to gravitational processes, the latter encapsulates the baryonic physics of galaxy formation. While both terms are functions of halo mass and redshift, the effective SFE also depends on the chosen UV magnitude limit.

In the left panel of Fig. 10, we plot $\mathrm{d}\rho_{\mathrm{UV}}/\mathrm{d}\lg M_{\mathrm{halo}}$ as function of mass and redshift as predicted by our theoretical model for a mass-dependent scatter. According the figure, the majority of the cosmic UV luminosity at $z \sim 6$–15 is produced by galaxies in haloes of moderate mass ($M_{\mathrm{halo}} \sim 10^9$–$10^{11}\,\mathrm{M}_\odot$). For instance, at $z = 6$ half the UV luminosity arises in haloes with $M_{\mathrm{halo}} \sim 10^{10.3}$–$10^{11}\,\mathrm{M}_\odot$ if a UV magnitude limit of $M_{\mathrm{UV,lim}} = -17$ is chosen. The mass range of haloes responsible for the majority of the UV luminosity shifts towards lower masses with increasing redshift, e.g. it is $M_{\mathrm{halo}} \sim 10^{9.1}$–$10^{9.6}\,\mathrm{M}_\odot$ at $z = 15$. For $M_{\mathrm{UV,lim}} = -14$, the corresponding halo mass ranges are $M_{\mathrm{halo}} \sim 10^{9.7}$–$10^{10.7}\,\mathrm{M}_\odot$ and $M_{\mathrm{halo}} \sim 10^{8.8}$–$10^{9.3}\,\mathrm{M}_\odot$. The downward shift of the halo mass range is partly driven by the evolution of the halo mass function which reduces the number density of massive haloes at higher z. Furthermore, haloes of a given mass have a higher growth rate at higher redshift (Behroozi & Silk 2015; Rodríguez-Puebla et al. 2016) and thus, for a non-evolving SFE–halo mass relation, harbour brighter galaxies ($\mathcal{L} \propto \mathcal{S}\dot{M}_{\mathrm{halo}}$). Consequently, a larger number of galaxies in low-mass haloes is UV detectable at higher z.

In order to analyse the impact a change in slope of the SFE–halo mass relation has on the UV luminosity density, we need to clarify how we adjust the normalization of the relation. In the following we choose a normalization such that the UV luminosity density at $z = 6$ remains unchanged. For instance, if we increase the fiducial value of the (high-mass) slope α_2 of the relation by 0.5, we need to decrease the normalization A by 0.66. Incidentally, the SFE in haloes of $\sim 10^{10.7}\,M_\odot$ remains approximately constant which is near the lower end halo mass range probed by Harikane et al. (2022). In this scenario, galaxies in haloes of a given mass below $10^{10.7}\,M_\odot$ have a higher SFE, and thus a higher UV luminosity, when the slope α_2 of the SFE–halo mass relation is lower. Also, a smaller slope allows additional galaxies, namely those from comparably low-mass haloes, to contribute to the UV luminosity density (see left versus right panel of Fig. 10). Hence, the UV luminosity density at $z > 6$ generally increases as α is decreased. The effect is stronger at higher z because then more of the UV luminosity arises from lower mass galaxies (see previous paragraph).

For a more quantitative discussion of the role of the slope of the SFE–halo mass relation it is useful to consider the contributions to

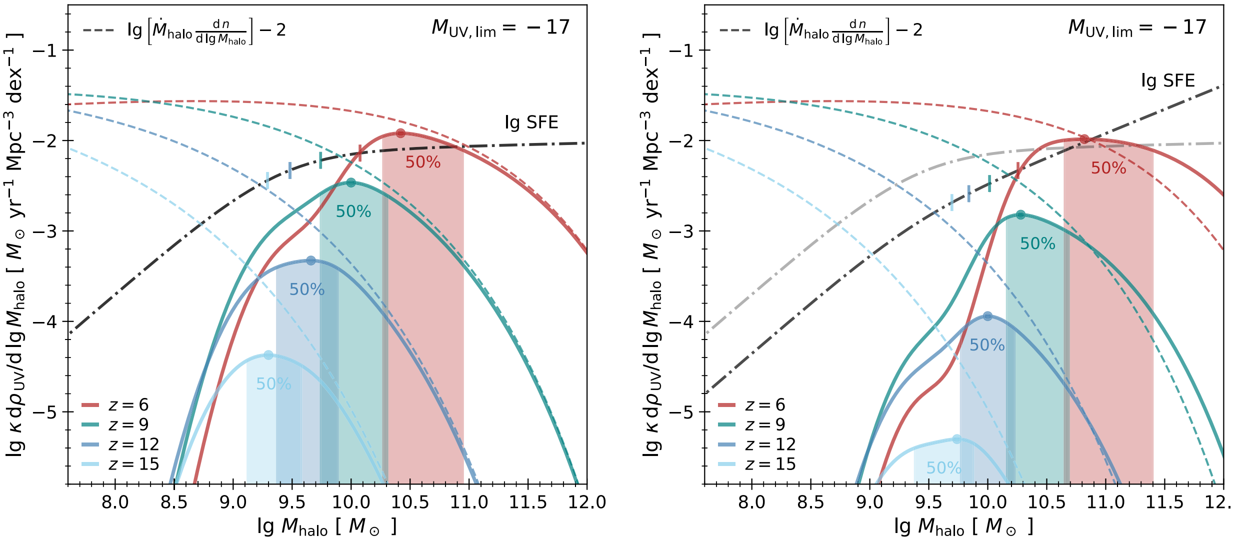

Figure 10. Contribution of haloes of different mass to the UV luminosity density at redshifts $z = 6 - 15$ according to equation (18) for a UV magnitude limit of $M_{\rm UV,lim} = -17$. Solid curves show $\kappa\, {\rm d}\rho_{\rm UV}/{\rm d}\lg M_{\rm halo}$, i.e. the UV luminosity density times the constant κ per dex in halo mass, in units of $M_\odot$ yr^{-1} cMpc^{-3}. Left: Predictions of the theoretical model for the non-evolving SFE–halo mass relation from the bottom right panel of Fig. 4 with high-mass slope $\alpha_2 = 0.032$ and normalization of $A = -2.370$ (dot–dashed line). Right: Same as the left panel but for an SFE–halo mass relation with a larger high-mass slope $\alpha_2 = 0.532$ and a lower normalization $A = -3.027$ (black dot–dashed line). The SFE–halo mass relation from the left panel is shown by a grey dot–dashed line for comparison. By construction, both relations result in the same UV luminosity density for galaxies brighter than $M_{\rm UV,lim} = -17$ at $z = 6$. In either panel, halo masses corresponding to $\langle\mathcal{S}\rangle_{\rm eff} = 0.5\langle\mathcal{S}\rangle$ are indicated by short vertical lines on the SFE–halo mass relation. Dashed lines depict the halo mass growth rate density per dex in halo mass, $\dot{M}_{\rm halo}{\rm d}n/{\rm d}\lg M_{\rm halo}$ in units M$_\odot$ yr^{-1} cMpc^{-3}, rescaled by a factor of 1/100 for visual clarity. Circles indicate the halo mass corresponding to the maximum value of ${\rm d}\rho_{\rm UV}/{\rm d}\lg M_{\rm halo}$, while shaded areas labelled ‘50 per cent’ depict the halo mass range contributing to half the total UV luminosity density down to the magnitude limit. As detailed in the text, a shallower slope of the SFE–halo mass relation implies a larger downward shift of this halo mass range resulting in a more gradual evolution of the UV luminosity density.

the UV luminosity density from different halo masses via equation (18). As discussed above, reducing the slope implies that additional UV luminosity is provided by galaxies in low-mass haloes. The ‘typical mass’ of haloes dominating the total UV luminosity, which we may define to be represented by the mode in the ${\rm d}\rho_{\rm UV}/{\rm d}\lg M_{\rm halo}$ distribution, thus decreases with decreasing α_2 at fixed z. As this typical halo mass changes with redshift, both the halo mass growth rate density $\dot{M}_{\rm halo}{\rm d}n/{\rm d}\lg M_{\rm halo}$ and the effective SFE of such haloes evolves as well. Specifically, in our fiducial model, the effective SFE at this typical halo mass decreases by about 0.6 dex between $z = 6$ and $z = 15$, the halo mass growth rate density decreases by about 1.8 dex, and the size of the halo mass range contributing half the total UV luminosity decreases by about 0.2 dex. Hence, the UV luminosity density should evolve by about 2.6 dex between $z = 6$ and $z = 15$, which is consistent with Fig. 7. By contrast, if we increase α_2 by 0.5, the effective SFE of the typical halo mass decreases by 0.9 dex, the halo mass growth rate density plummets by about 2.4 dex, and the width of the halo mass is reduced by 0.2 dex, resulting in a much steeper redshift evolution of the UV luminosity density (3.5 dex between $z = 6$ and $z = 15$).

In conclusion, we attribute the gradual evolution of the UV luminosity density in FIREbox^{HR}, compared with other theoretical studies, to the more accurate accounting of baryonic processes in the FIRE-2 physics model. At $z \sim 6 - 15$, these baryonic processes give rise to a redshift-independent SFE–halo mass relation with a comparably shallow slope at intermediate halo masses ($M_{\rm halo} \sim 10^9 - 10^{11}\, M_\odot$). As described above, a shallower slope results in an additional number of UV detectable galaxies in low-mass haloes at higher z, and, hence, a more gradual evolution of the cosmic UV luminosity density.

3.6 Implications of a non-evolving SFE–halo mass relation: the role of galaxies for the cosmic reionization history

During cosmic reionization ($z \sim 6 - 10$), the neutral hydrogen component of the intergalactic medium (IGM) is converted into its ionized state (e.g. Fan, Carilli & Keating 2006; Robertson et al. 2010). The primary physical driver of this phase transition is thought to be Lyman-continuum radiation escaping low-mass galaxies (Madau, Haardt & Rees 1999; Gnedin 2000; Robertson et al. 2015; Mascia et al. 2023; Simmonds et al. 2023b; Atek et al. 2024; Dayal et al. 2024). In this section, we will explore the implications of the theoretical model implemented as described in Section 3.5 by comparing its predictions with available observational constraints on the ionization of the IGM. Specifically, by linking the predicted UV luminosity to the observed ionized hydrogen fraction of the Universe, we will constrain the product of the escape fraction $f_{\rm esc}$ of ionizing radiation and the ionizing photon production efficiency $\xi_{\rm ion}$ of faint galaxies.

We model the reionization history of the IGM with the help of a commonly employed analytical technique that keeps track of the number density of ionizing photons (Madau et al. 1999; Kuhlen & Faucher-Giguère 2012; Gnedin & Madau 2022). Specifically, we follow the approach by So et al. (2014) and write the time evolution of the volume fraction Q of ionized hydrogen as

$$\frac{{\rm d}Q}{{\rm d}t} = \frac{\gamma}{\delta}\frac{\dot{n}_{\rm ion}}{\bar{n}_{\rm H}} - \frac{Q}{\bar{t}_{\rm rec}}, \qquad (19)$$

where $\dot{n}_{\rm ion} = f_{\rm esc}\, \xi_{\rm ion}\, \rho_{\rm UV}$ is the injection rate of ionizing photons per volume, $f_{\rm esc}$ is the fraction of ionizing photons escaping from galaxies, $\xi_{\rm ion}$ is the rate of ionizing photons per spectral UV luminosity, $\rho_{\rm UV}$ is the intrinsic spectral UV luminosity density, $\bar{n}_{\rm H}$ is the average number density of hydrogen nuclei, and $\bar{t}_{\rm rec}$ is an averaged recombination time-scale. Compared to Madau et al. (1999), this equation contains the extra factors γ and δ. Multiplying $\dot{n}_{\rm ion}$ by γ converts the injection rate density of ionizing photons to the ionization rate density, while multiplying $\bar{n}_{\rm H}$ by δ accounts for the slightly higher density of ionized bubbles compared to the cosmic average. We adopt the following parametrizations for γ, δ, and $\bar{t}_{\rm rec}$, obtained by fitting to the results of radiative transfer calculations (So et al. 2014)

$$\gamma = 1 - 0.91 Q^{2.44},\ \delta = \frac{1+0.02}{Q^{0.12}+0.02},$$
$$\bar{t}_{\rm rec} = 5.6\times 10^{12}\,(1+z)^{-4.35}\ {\rm yr}. \qquad (20)$$

While the use of this parametrization is not without caveats, e.g. the simulations by So et al. (2014) only cover volumes of 20 cMpc^3 and employ a different (WMAP year 7) cosmology, the predictions of equation (19) are similar if $\gamma = \delta = 1$ is chosen, except near $z \sim 6 - 6.75$, where this choice results in earlier and more abrupt completion of reionization.

For simplicity, we assume that $f_{\rm esc}\,\xi_{\rm ion}$ is a constant. Incidentally, this model then implies that comparably faint galaxies (fainter than $M_{\rm UV} \sim -16$ to -17, see Fig. 2) dominate the reionization budget at $z \sim 6 - 11$ (e.g. Wise et al. 2014; Katz et al. 2019; Lewis et al. 2020), not more luminous galaxies with $M_{\rm UV} < -18$ (cf. Naidu et al. 2020). We use in this section the SFE–halo mass relation derived from the intrinsic UV luminosity of FIREbox^{HR} galaxies (third row in Tables 1 and 2). However, we find no qualitative, and only minor quantitative, changes if we adopt SFEs based on dust-attenuated UV luminosities.

Given $f_{\rm esc}\,\xi_{\rm ion}$ and a cosmic UV luminosity density $\rho_{\rm UV}(z)$ provided by our theoretical model, we solve equations (19, 20) numerically with the SCIPY.INTEGRATE.SOLVE_IVP function starting from a small, positive value for Q at $t = 0$ (we use 10^{-7}). Values of $Q > 1$ are clipped to $Q = 1$. A limiting magnitude of $M_{\rm UV,lim} = -12$ is used to calculate $\rho_{\rm UV}(z)$. The reionization history predicted by this model is insensitive to the choice of $M_{\rm UV,lim} \geq -14$.

We set the value of $f_{\rm esc}\,\xi_{\rm ion}$ by comparing the predicted optical depth $\tau_{\rm e}$ of CMB photons due to free electron scattering to the observed optical depth $\tau_{\rm e,Planck} = 0.0561$ (Aghanim et al. 2020). To this end, we first calculate the optical depth between redshifts 0 and z (Kuhlen & Faucher-Giguère 2012):

$$\tau_{\rm e}(z) = \sigma_{\rm T}\bar{n}_{\rm H}c\int_0^z \frac{1+z^2}{H(z)}Q(z)\left(1+\eta\frac{Y}{4(1-Y)}\right){\rm d}z, \qquad (21)$$

where $\sigma_{\rm T}$ is the Thomson cross-section, c is the speed of light, $H(z)$ is the Hubble parameter, $Q(z)$ is the reionization history computed numerically via equations (19) and (20), $Y = 0.243$ is the cosmic Helium mass fraction (Aver, Olive & Skillman 2015; Peimbert, Peimbert & Luridiana 2016; Aghanim et al. 2020), and $\eta = 1$ ($\eta = 2$) assumes singly (doubly) ionized Helium at $z \geq 4$ ($z < 4$). We then find a value for $f_{\rm esc}\,\xi_{\rm ion}$ such that $\tau_{\rm e}(z = 14) = \tau_{\rm e,Planck}$ with the help of the SCIPY.OPTIMIZE.ROOT_SCALAR function. To represent the uncertainty in the Planck 2018 measurement, we also constrain $f_{\rm esc}\,\xi_{\rm ion}$ such that $\tau_{\rm e}(z = 14)$ equals $\tau_{\rm e,Planck} \pm 0.0071$ and $\tau_{\rm e,Planck} \pm 2 \times 0.0071$.

Fig. 11 compares the reionization history $Q(z)$ predicted by our theoretical model with a variety of observational data based on Ly α dark pixel fractions (McGreer et al. 2015), gap-peak statistics in quasar absorption spectra (Gallerani et al. 2007), Ly α damping wing absorption of quasars and galaxies (Schroeder et al. 2013; Greig et al. 2017; Bañados et al. 2018; Greig et al. 2022; Hsiao et al. 2024; Umeda et al. 2024), clustering of Ly α emitters (Ouchi et al. 2010; Sobacchi & Mesinger 2015), fractions and equivalent width distributions of Ly α emitters (Schenker et al. 2014; Mason et al. 2019; Bolan et al. 2021; Bruton et al. 2023), and Ly α opacity statistics (Gaikwad et al. 2023). The reionization history predicted by the theoretical model is in good agreement with observational data for $f_{\rm esc}\,\xi_{\rm ion}$ values that result in optical depths close to $\tau_{\rm e,Planck}$. Once possible exception is the lower limit of 0.12 at $z = 10.6$ reported by Bruton et al. (2023) which, however, conflicts with the upper limit of 0.1 at $z = 10.17$ reported by Hsiao et al. (2024). Replacing equation (20) with the simpler ansatz $\gamma = \delta = 1$ leads to reionization histories that are near identical to those shown in the figure when $Q < 0.7$ but also to a much faster evolution of the ionized hydrogen fraction during the final stages of reionization.

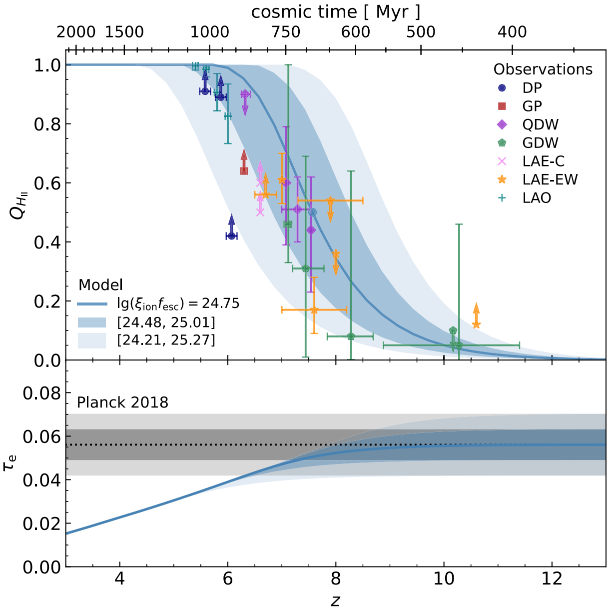

Figure 11. Reionization history predicted by the theoretical model for a non-evolving SFE–halo mass relation inferred from FIREbox^{HR}. In each panel, results are shown for a range of values for $f_{\rm esc}\xi_{\rm ion}$, see legend, and for a limiting magnitude of $M_{\rm UV} = -12$. Top: Volume-weighted ionized hydrogen fraction predicted by the model. Overplotted are observational constraints based on the Ly α dark pixel fraction (DP; McGreer, Mesinger & D'Odorico 2015), gap-peak statistics in quasar absorption spectra (GP; Gallerani et al. 2007), Ly α damping wing absorption of quasars (QDW; Schroeder, Mesinger & Haiman 2013; Greig et al. 2017; Bañados et al. 2018; Greig et al. 2022), Ly α damping wing absorption of galaxies (GDW; Hsiao et al. 2024; Umeda et al. 2024), clustering of Ly α emitters (LAE-C; Ouchi et al. 2010; Sobacchi & Mesinger 2015), the fractions and equivalent width distributions of Ly α emitters (LAE-EW; Schenker et al. 2014; Mason et al. 2019; Bolan et al. 2021; Bruton et al. 2023), and Ly α opacity statistics (LAO; Gaikwad et al. 2023), see legend. Upper and lower limits are indicated by arrows and correspond to the 95 per cent confidence level, if reported, otherwise to the 68 per cent confidence level. Horizontal error bars indicate the redshift range of the observational sample. Vertical error bars show uncertainties in the estimated ionized volume fraction at the 68 percentile confidence level. The blue circle at the centre of the upper panel indicates the mid-point of re-ionization at $z_{\rm re} = 7.57$ as predicted by the theoretical model for $f_{\rm esc}\xi_{\rm ion} = 10^{24.74}\,{\rm Hz\,erg^{-1}}$. Bottom: Optical depth of cosmic microwave background (CMB) photons due to Thomson scattering off free electrons as predicted by the model. The values for $f_{\rm esc}\xi_{\rm ion}$ are chosen to match the measured optical depth by the Planck Collaboration (dotted line; Aghanim et al. 2020), obtained from CMB power spectra combined with CMB lensing reconstruction and baryonic acoustic oscillations, and the boundaries of the 68 and 95 percentile confidence interval (grey shaded regions). The model is in good agreement with observational data provided $f_{\rm esc}\xi_{\rm ion}$ lies in the range $\sim 10^{24.5} - 10^{24.7}\,{\rm Hz\,erg^{-1}}$.

Table 3. Statistics of the reionization history as predicted by the theoretical model for a non-evolving SFE–halo mass relation inferred from FIREbox^{HR} for given UV magnitude limits $M_{\rm UV,lim}$ (row header) and values of $\zeta \equiv \lg(f_{\rm esc}\,\xi_{\rm ion}\,[{\rm Hz\,erg^{-1}}])$ (first column). The values of ζ are chosen such that the electron scattering optical depth $\tau_{\rm e}$ (second column) predicted by the model matches the optical depth reported by Planck 2018 ($\tau_{\rm e,Planck} = 0.0561$) or the lower and upper values of its 68 per cent and 95 per cent confidence intervals. Columns 3–9 list the redshift of the mid-point of reionization ($z_{\rm re} \equiv z_{50}$), the duration of reionization defined as $\Delta z_{\rm re} = z_{10} - z_{90}$ or $\tilde{\Delta} z_{\rm re} = z_{25} - z_{75}$, and the redshifts z_f corresponding to $Q(z_f) = f/100$ for $f = 10, 25, 75, 90$.

ζ	$\tau_{\rm e}$	$z_{\rm re}$	$\Delta z_{\rm re}$	$\tilde{\Delta} z_{\rm re}$	z_{10}	z_{25}	z_{75}	z_{90}
				$M_{\rm UV,lim} = -12$				
24.21	0.0419	6.04	2.84	1.40	7.84	6.85	5.44	5.00
24.48	0.0490	6.82	2.80	1.40	8.58	7.62	6.22	5.78
24.75	0.0561	7.57	2.78	1.38	9.31	8.35	6.97	6.53
25.01	0.0632	8.28	2.75	1.37	9.99	9.06	7.69	7.24
25.27	0.0703	8.97	2.72	1.35	10.66	9.73	8.39	7.94
				$M_{\rm UV,lim} = -14$				
24.24	0.0419	6.05	2.77	1.38	7.81	6.84	5.46	5.03
24.52	0.0490	6.83	2.74	1.37	8.55	7.61	6.25	5.81
24.80	0.0561	7.58	2.70	1.35	9.27	8.34	6.99	6.57
25.07	0.0632	8.29	2.67	1.33	9.95	9.04	7.72	7.28
25.33	0.0703	8.98	2.62	1.30	10.61	9.71	8.41	7.98

As highlighted by the figure, a larger (smaller) optical depth goes along with an earlier (later) start, mid-point, and finish of reionization. This trend puts strong limits on the allowed optical depth in the context of our model. For instance, an optical depth similar to the Planck 2015 best-fitting value of 0.066, which is about 1.4σ above the 2018 estimate, would appear to be inconsistent with several observational constraints (Schroeder et al. 2013; Schenker et al. 2014; Bolan et al. 2021). For $\tau_{\rm e} = 0.0561 \pm 0.0071$, the mid-point of reionization is predicted to take place at $z_{\rm re} = 7.57^{+0.71}_{-0.75}$, which is consistent with the estimate $z_{\rm re} = 7.82 \pm 0.71$ by Planck 2018 (Aghanim et al. 2020). Our model predicts an extended duration of reionization $\Delta z_{\rm re} = z_{10} - z_{90} \sim 2.8$ and $\tilde{\Delta} z_{\rm re} = z_{25} - z_{75} \sim 1.4$ with only a weak dependence on the choice of $f_{\rm esc}\,\xi_{\rm ion}$. Here, z_f is the redshift at which $Q = f/100$. While current estimates are still rather uncertain, an extended duration of reionization ($\Delta z_{\rm re} \sim 2 - 4$, $\tilde{\Delta} z_{\rm re} \sim 1 - 2$), potentially driven by the large contribution of UV faint galaxies (Kuhlen & Faucher-Giguère 2012), is at least consistent with cosmological radiative transfer simulations (Rosdahl et al. 2018; Kannan et al. 2022; Villasenor et al. 2022), semi-numerical approaches (Maity & Choudhury 2022; Bera et al. 2023), and observational data (Adam et al. 2016; Reichardt et al. 2021; Gorce, Douspis & Salvati 2022). The figure also shows that the evolution of $Q(z)$ is not symmetric in redshift around the mid-point, i.e. it is not well described by a shifted hyperbolic tangent function that is sometimes adopted by models. Table 3 lists the reionization mid-point and duration predicted by our theoretical model for different choices of the limiting UV magnitude $M_{\rm UV,lim}$ and values of $f_{\rm esc}\,\xi_{\rm ion}$.

Quantitatively, we find that values of

$$\zeta \equiv \lg\,(f_{\rm esc}\,\xi_{\rm ion}[{\rm Hz\,erg^{-1}}]) \sim 24.5 - 24.7 \qquad (22)$$

result in good agreement with most observational data. To convert constraints on ζ into an estimate of the escape fraction, we need to divide by the ionizing photon production efficiency $\xi_{\rm ion}$. At $z \sim 4 - 6$ the efficiency $\lg\,(\xi_{\rm ion}\,[{\rm Hz\,erg^{-1}}])$ is $\sim 25 - 25.5$ (e.g. Robertson et al. 2013; Bouwens et al. 2016a; Naidu et al. 2020; Castellano et al. 2023; Saldana-Lopez et al. 2023; Simmonds et al. 2023a), with a similar range in ionizing efficiency also predicted by numerical models (e.g. Wilkins et al. 2016; Ceverino, Klessen & Glover 2019; Seeyave et al. 2023). Recent estimates with *JWST*, however, suggest somewhat larger values up to 25.8 in galaxies at $z \sim 7 - 9$ likely as a result of their younger ages and lower metallicities (Endsley et al. 2023b; Fujimoto et al. 2023; Simmonds et al. 2023b; Tang et al. 2023; Atek et al. 2024). Adopting the upper value of $\lg\,(\xi_{\rm ion}\,[{\rm Hz\,erg^{-1}}]) = 25.8$, we infer escape fractions of $f_{\rm esc} = 0.05 - 0.08$, while lower ionization efficiencies of 25.4 and 25.0 would imply correspondingly larger escape fractions of $f_{\rm esc} = 0.12 - 0.20$ and $f_{\rm esc} = 0.30 - 0.50$.

The escape fractions of galaxies that dominate cosmic reionization have yet to be fully constrained. Numerical predictions vary significantly depending on included physics, resolution, redshift, and halo mass (e.g. Kimm & Cen 2014; Wise et al. 2014; Sharma et al. 2016; Rosdahl et al. 2022). For instance, cosmological simulations with FIRE-2 physics suggest average escape fractions $f_{\rm esc} \sim 20$ per cent (Ma et al. 2020) that peak in $M_{\rm halo} \sim 10^{9.5}$–$10^{11}\,{\rm M}_{\odot}$ haloes, while other recent works suggest somewhat smaller values ($f_{\rm esc} \sim 3$–10 per cent, e.g. Katz et al. 2018; Lewis et al. 2020; Rosdahl et al. 2022; Yeh et al. 2023) with a different mass dependence. Observational constraints can only be indirect given that Lyman continuum photons emitted from galaxies during reionization are fully absorbed by intervening neutral hydrogen (Inoue et al. 2014). Scaling relations based on local analogs suggest escape fractions during reionization in the range of 10–15 per cent (Lin et al. 2023; Mascia et al. 2023), while measurements of escape fractions at $z \sim 2 - 5$ are often found to be in the range 5–10 per cent (Matthee et al. 2017; Pahl et al. 2021; Saldana-Lopez et al. 2023) but with a large scatter for individual objects sometimes showing much larger escape fractions (Leethochawalit et al. 2016; Shapley et al. 2016; Naidu et al. 2017).

In summary, a non-evolving SFE–halo mass relation produces an ionization history in agreement with observations provided $\lg\,(f_{\rm esc}\,\xi_{\rm ion}[{\rm Hz\,erg^{-1}}])$ is about $24.5 - 24.7$. Large ionizing efficiencies $\lg\,(\xi_{\rm ion}\,[{\rm Hz\,erg^{-1}}]) \sim 25.8$ thus imply small escape fractions of ~ 5–8 per cent, see also Muñoz et al. (2024). Vice versa, larger escape fractions of ~ 20 per cent as predicted by FIRE-2 zoom-in simulations at $z \sim 6$–10 (Ma et al. 2020) require lower average ionization efficiencies of 25.2–25.4 (cf. Endsley et al. 2023a) to avoid overproducing ionizing photons resulting in too early an reionization of the Universe. Future measurements of the ionization efficiency during $z \sim 6$–10 for large representative samples with *JWST* should provide more clarity.

3.7 Caveats

A caveat of the present study is that it is limited to a single physical model (FIRE-2). Fortunately, the chosen model is able to reproduce successfully the galaxy properties of interest, i.e. the UV LFs and the evolution of the UV luminosity density, lending credence to the inferences drawn from it. Furthermore, the model has been extensively validated in previous studies from the FIRE collaboration (Faucher-Giguère 2018; Hopkins et al. 2018).

A further concern is the mass range of galaxies captured by FIREbox^{HR}. While the high resolution of the simulation allows us to resolve faint galaxies, the high-mass end ($M_{\rm star} > 10^9\,{\rm M}_{\odot}$, $M_{\rm halo} > 10^{11}\,{\rm M}_{\odot}$) is not well sampled given the modest box size ($L \sim 22.1$ cMpc). However, as we demonstrated explicitly, the lack of such massive galaxies does not affect the UV luminosity density at a significant level (Fig. 2). Furthermore, given the focus on low- to intermediate-mass galaxies, the lack of AGN feedback in FIREbox^{HR} does not appear to pose a significant limitation. We plan to revisit the role of AGN feedback with future simulations covering larger volumes.

A recent study by Borrow et al. (2023) suggests that the use of a spatially uniform cosmic ionizing background may overestimate the UV luminosity in faint, low-mass galaxies ($M_{\rm UV} \gtrsim -13$, $M_{\rm star} \lesssim 10^6\,{\rm M}_{\odot}$) compared with a fully self-consistent radiation-hydrodynamical simulation. However, such galaxies do not strongly influence the cosmic UV luminosity density (Figs 2 and 3). Moreover, while a uniform background is used to capture the collective radiation from distant galaxies, FIREbox^{HR} also accounts explicitly, albeit approximately, for local inhomogeneities in the radiation field (see Section 2.1).

Our estimates also do not account for a potential Population III contribution with a top-heavy IMF which could boost the UV luminosities significantly (Zackrisson et al. 2011; Harikane et al. 2023; Yung et al. 2023). More generally, the physics of star formation, gas cooling, and feedback, might noticeably change at the earliest cosmic times leading to different SFEs. Our work suggests, however, that such strong changes are not present at $z < 14$. We leave a deeper exploration of this topic for future work.

4 SUMMARY AND CONCLUSIONS

We have introduced FIREbox^{HR}, a high-resolution cosmological volume simulation from the FIRE project, to explore galaxy formation from late Cosmic Dawn through the end of reionization – a period that continues to attract intense observational and theoretical interest. The simulation covers the same volume ($L = 22.1$ Mpc) as the original FIREbox run (Feldmann et al. 2023) down to $z = 6.3$, employing the established FIRE-2 physics model, but with significantly improved numerical resolution ($m_{\rm b} \sim 7800\,M_{\odot}$). FIREbox^{HR} resolves a substantial number of faint, low-mass galaxies (e.g. about 2000 galaxies with $M_{\rm UV} < -14$ or with $M_{\rm star} > 10^{6.4}\,M_{\odot}$ at $z = 6.3$) making it well suited to examine the evolution of the faint end of the galaxy population that may have played a pivotal role in cosmic reionization (e.g. Robertson et al. 2015; Mascia et al. 2023; Simmonds et al. 2023b; Atek et al. 2024; Dayal et al. 2024). In this initial application of FIREbox^{HR}, we analysed the predicted UV luminosities and star formation efficiencies (SFEs) of high-redshift galaxies ($z \sim 6-15$) and discussed implications for early galaxy formation. We plan to investigate other properties of FIREbox^{HR} galaxies, such their metallicities, sizes, and shapes, in future work. Our main findings are as follows:

(i) The UV LFs predicted by FIREbox^{HR} are in excellent agreement with observations at $z \sim 6$–12 (Fig. 1). The UV LFs are well fit by a Schechter function or double power law for $M_{\rm UV}$ brighter than about -15. At magnitudes near or just below current observational limits at $z \sim 6$–8, the predicted LFs deviate from the traditional Schechter form indicative of a turn-over.

(ii) The cosmic UV luminosity density at $z \sim 6$–12 is dominated by galaxies of moderate luminosity, i.e. by galaxies with $M_{\rm UV} \sim -18$ to -18.5 for a UV magnitude limit $M_{\rm UV,lim} = -17$ and by galaxies with $M_{\rm UV} \sim -16$ to -17 for $M_{\rm UV,lim} = -12$, depending on redshift (Fig. 2). These galaxies reside in haloes of intermediate mass $M_{\rm halo} \sim 10^9$–$10^{11}\,{\rm M}_{\odot}$.

(iii) In contrast to other theoretical and empirical studies (e.g. Tacchella et al. 2018; Harikane et al. 2022; Kannan et al. 2023), FIREbox^{HR} reproduces the comparably gradual evolution of the UV luminosity density out to $z \sim 14$ found in recent *JWST* observations (Fig. 3). FIREbox^{HR} demonstrates that such a comparably shallow evolution of the UV luminosity density is not in conflict to galaxy formation theory but a natural outcome of galaxy evolution in the context of the FIRE-2 physics model.

(iv) The SFE–halo mass relation of FIREbox^{HR} galaxies does not significantly evolve with redshift and is only weakly dependent on mass for intermediate-mass haloes ($M_{\rm halo} \sim 10^9$–$10^{11}\,{\rm M}_{\odot}$; see Fig. 4). The slope for $M_{\rm halo} \sim 10^{10}$–$10^{11}\,{\rm M}_{\odot}$ haloes is ~ 0.03 if dust-attenuated UV luminosities are used as SFR tracers and ~ 0.3 if based on intrinsic UV luminosities or time-averaged SFRs. The scatter of the relation, which as defined here measures the variability of the UV luminosity or SFR, shows no obvious dependence on redshift and it is too small ($\sim 0.3 - 0.6$ dex over the same halo mass range) to substantially affect the UV luminosity density for $M_{\rm UV,lim} = -17$. The comparably gradual evolution of the UV luminosity density at $z \sim 6$–14 is thus neither explained by galaxies at higher redshift becoming more efficient on average in forming stars nor by an increase in the scatter of the SFE. Indeed, given the monotonic increase of the SFE with halo mass for $M_{\rm halo} \sim 10^9$–$10^{11}\,{\rm M}_{\odot}$ haloes, individual galaxies tend to become less efficient in forming stars at higher redshift. A parametrization of the SFE–halo mass relation in FIREbox^{HR} is provided in Table 1.

(v) The stellar mass–halo mass relation (SHMR) predicted from the non-evolving SFE–halo mass relation is in line with the actual SHMR in FIREbox^{HR} (Fig. 5). The slope (~ 0.5) of the SHMR for $M_{\rm halo} \sim 10^{10}$–$10^{11}\,{\rm M}_{\odot}$ haloes is steeper than the slope (~ 0.03) of the (dust-attenuated UV luminosity based) SFE–halo mass relation largely, but not completely, because of the dust-attenuation. Possible explanations for the remaining difference in slope are discussed in Section 3.3.

(vi) A simple theoretical model based on the inferred SFE–halo mass relation well reproduces the observed, gradual evolution of the UV luminosity density (Fig. 6). Applying this model up to $z = 20$, we observe a pronounced decrease in cosmic UV luminosity density at higher redshifts (Fig. 7). As a result, detecting neutral hydrogen in absorption via Ly activation of its 21 cm line appears not to be possible at redshifts as high as suggested by the 21 cm interpretation of the EDGES signal. Formally, $\rho_{\rm UV}(z)$ exceeds the minimum required UV luminosity density (Madau 2018) only at $z \lesssim 14$ (for $M_{\rm UV,lim} = -12$), i.e. at a time around which cosmic gas was presumably (pre-)heated by stellar and X-ray sources (e.g. Eide et al. 2020; Abdurashidova et al. 2023).

(vii) The evolution of the cosmic UV luminosity density depends on the slope and normalization of the SFE—halo mass relation for $M_{\rm halo} \sim 10^9$–$10^{11}\,{\rm M}_{\odot}$ haloes but not on its scatter provided the latter is in a range (~ 0.2–0.6 dex) consistent with FIREbox^{HR} (Fig. 9).

(viii) Further inspection of the theoretical model reveals that the comparably gradual evolution of the cosmic UV luminosity density is a consequence of the weak mass dependence (and the redshift independence) of the SFE–halo mass relation in the intermediate halo mass regime (Fig. 10). When reducing the slope of the relation while keeping the UV luminosity density at $z = 6$ fixed, galaxies in $M_{\rm halo} \lesssim 10^{10.7}$ M$_\odot$ haloes tend to become more UV luminous. Also, additional galaxies in low-mass haloes may exceed the adopted UV magnitude limit and thus contribute to the UV luminosity density. The resulting increase in the cosmic UV luminosity density is stronger at higher z as the typical halo mass harbouring galaxies contributing to the cosmic UV luminosity density becomes smaller. Hence, a lower (i.e. shallower) slope of the SFE–halo mass relation in the intermediate halo mass range leads to a more gradual evolution of the UV luminosity density. In contrast, the large slopes (~ 1–1.2) adopted by previous non-evolving SFE models (Tacchella et al. 2018; Harikane et al. 2022) lead to a steep evolution of $\rho_{\rm UV}(z)$ at $z \sim 6$–14.

(ix) The faint end slope of the UV LF steepens with increasing redshift (Fig. 8). Deviations from a pure Schechter function may not necessarily point to a turn-over at low luminosities but could reflect a double power law form of the UV LFs. Changes to the low-mass and high-mass slope of the SFE–halo mass relation affect the UV LF in expected ways.

(x) The theoretical model based on the non-evolving SFE–halo mass relation predicts a reionization history in line with both observational data at $z \sim 5.5$–10 and the optical depth reported by Planck 2018 provided $\zeta \equiv \lg\,(f_{\rm esc}\,\xi_{\rm ion}[{\rm Hz\,erg}^{-1}])$ is in the range ~ 24.5–24.7 (Fig. 11). Here, $f_{\rm esc}$ is the escape fraction of ionizing radiation and $\xi_{\rm ion}$ is the ionizing photon production efficiency. Table 3 lists the reionization mid-point and duration for different choices of ζ.

(xi) The constraint $\zeta \sim 24.5 - 24.7$ translates into escape fractions of $f_{\rm esc} = 0.05 - 0.08$ ($f_{\rm esc} = 0.12 - 0.20$, $f_{\rm esc} = 0.30 - 0.50$) for ionizing efficiencies $\lg\,(\xi_{\rm ion}\,[{\rm Hz\,erg}^{-1}]) = 25.8\ \ (25.4,\ \ 25.0)$. Adopting $f_{\rm esc} \sim 0.2$ as predicted by FIRE-2 zoom-in simulations at $z \sim 6 - 10$ (Ma et al. 2020) implies an average ionizing efficiency of $\lg\,(\xi_{\rm ion}\,[{\rm Hz\,erg}^{-1}]) = 25.2 - 25.4$.

The present work leaves open several key follow-up questions for future studies. First, it remains to be understood how the physical processes included in the simulation lead to an SFE–halo mass relation for $M_{\rm halo} \sim 10^9$–10^{11} M$_\odot$ haloes at $z \sim 6$–15 that is only weakly dependent on halo mass and redshift. Here, a thorough exploration of the dependence of the SFE–halo mass relation on either the adopted physical model or on secondary galaxy or halo properties should prove fruitful. Secondly, we may ask how the SFE–halo mass relation evolves at the massive end ($M_{\rm halo} > 10^{11}$ M$_\odot$), which is not probed by FIREbox^{HR} because of its modest box size. Empirical models predict a potential reduction of the SFE at masses above $M_{\rm halo} \sim 10^{11.2}$–$10^{11.7}$ M$_\odot$ and perhaps some redshift evolution (Tacchella et al. 2018; Harikane et al. 2022). Simulations of moderately large cosmological volumes with AGN feedback will likely be needed to properly explore this mass regime. Such simulations should not only help to constrain the physical parameters of AGN feedback by comparing with available *JWST* observations of UV bright galaxies, but also provide insights into the growth of massive, luminous galaxies with star formation efficiencies (e.g. Bassini et al. 2023; Lovell et al. 2023; Carnall et al. 2024; Casey et al. 2024; Glazebrook et al. 2024). Thirdly, understanding how galaxies reionize intergalactic gas and influence its topology is a key focus of many observational programs, including those planned with the upcoming SKAO. Given that the SFE–halo mass relation encapsulates well the star formation activity of galaxies during the epoch of reionization, it appears promising to combine the theoretical model outlined in this paper with approximate numerical methods based on one-dimensional radiative transfer calculations (e.g. Ghara et al. 2018; Schaeffer, Giri & Schneider 2023), as a computationally cheaper alternative to radiative-hydrodynamical simulations (e.g. Rosdahl et al. 2018; Ocvirk et al. 2020; Kannan et al. 2022; Lewis et al. 2022). A better understanding of the SFE–halo mass relation also holds great value for semi-numerical models that predict line intensities of 21 cm (Park et al. 2019) and other emission lines (e.g. Sun et al. 2023b).

Many predictions from this study will be testable through forthcoming observations. The stronger evolution of $\rho_{\rm UV}(z)$ at $z \gtrsim 13$, for example, could be explored with deeper *JWST* observations, potentially aided by strong gravitational lensing. Such observational studies may also be able to test the continued steepening of the faint end slope of the UV LFs with increasing redshift beyond the epochs currently probed. Additionally, the shape of the UV LF at $M_{\rm UV} \sim -13$ (e.g. turn-over versus power-law) may be more robustly quantified with deeper observations at $z \sim 5$–6. Finally, the SFE in low-mass haloes may be measured directly by analysing the clustering of UV faint galaxies. These future observations will not only test our current understanding of galaxy formation but also impose critical constraints on the involved physics during the first billion years of cosmic time.

ACKNOWLEDGEMENTS

The authors are grateful to the referee for their thoughtful suggestions, which improved the manuscript. RF thanks Andrey Kravtsov for insightful discussions which inspired the addition of Appendix D. RF acknowledges financial support from the Swiss National Science Foundation (grants PP00P2_194814 and 200021_188552). MBK acknowledges support from NSF CAREER award AST-1752913, NSF grants AST-1910346 and AST-2108962, and HST-GO-16686, HST-AR-17028, and HST-AR-17043 from the Space Telescope Science Institute, which is operated by AURA, Inc., under NASA contract NAS5-26555. MBK and JSB acknowledge supported from NASA grant 80NSSC22K0827. CAFG was supported by NSF through grants AST-1715216, AST-2108230, and CAREER award AST-1652522; by NASA through grant 17-ATP17-0067; by STScI through grant HST-AR-16124.001-A; and by the Research Corporation for Science Advancement through a Cottrell Scholar Award. DK was supported by NSF grant AST-210834. AL was supported by NASA grant 80NSSSC20K1469. PO acknowledges funding from the Swiss State Secretariat for Education, Research and Innovation (SERI) under contract number MB22.00072, as well as from the Swiss National Science Foundation (SNSF) through project grant 200020_207349. The Cosmic Dawn Center (DAWN) is funded by the Danish National Research Foundation under grant DNRF140. This work was supported in part by a Simons Investigator award from the Simons Foundation (EQ) and by NSF grant AST-2107872. GS was supported by a CIERA Postdoctoral Fellowship. This research was supported in part by the International Space Science Institute (ISSI) in Bern, through ISSI International Team project #562 (First Light at Cosmic Dawn: Exploiting the James Webb Space Telescope Revolution) and by grant NSF PHY-1748958 to the Kavli Institute for Theoretical Physics (KITP). This work also benefited from discussions during the Nordita Program 'Cosmic Dawn at High Latitudes'. We acknowledge PRACE for awarding us access to MareNostrum at the Barcelona Supercomputing Center (BSC), Spain. This research was partly carried out via the Frontera computing project at the Texas Advanced Computing Center. Frontera is made possible by National Science Foundation award OAC-1818253. This work was supported in part by an allocation from the Swiss National Supercomputing Centre (CSCS) under project IDs s697 and s698. We acknowledge access to Piz Daint and Alps/Eiger at the Swiss National Supercomputing Centre, Switzerland, under the University of Zurich's share with the project ID uzh18. This work made use of infrastructure services provided by S3IT (www.s3it.uzh.ch), the Service and Support for Science IT team at the University of Zurich. All plots were created with the MATPLOTLIB library for visualization with PYTHON (Hunter 2007). This research has made use of NASA's Astrophysics Data System.

DATA AVAILABILITY

The data supporting the plots within this article are available on reasonable request to the corresponding author. A public version of the GIZMO code is available at http://www.tapir.caltech.edu/~phopkins/Site/GIZMO.html. FIRE data releases are publicly available at http://flathub.flatironinstitute.org/fire.

REFERENCES

Abdurashidova Z. et al., 2022, ApJ, 925, 221

Abdurashidova T. H. C. Z. et al., 2023, ApJ, 945, 124

Adam R. et al., 2016, A&A, 596, A108

Adams N. J. et al., 2024, ApJ, 965, 169

Ade P. A. R. et al., 2016, A&A, 594, A13

Aghanim N. et al., 2020, A&A, 641, A6

Atek H., Richard J., Kneib J. P., Schaerer D., 2018, MNRAS, 479, 5184

Atek H. et al., 2023, MNRAS, 524, 5486

Atek H. et al., 2024, Nature, 626, 975

Aver E., Olive K. A., Skillman E. D., 2015, J. Cosmol. Astropart. Phys., 2015, 011

Bañados E. et al., 2018, Nature, 553, 473

Barkana R., Loeb A., 2000, ApJ, 539, 20

Barry N. et al., 2019, ApJ, 884, 1

Bassini L., Feldmann R., Gensior J., Hayward C. C., Faucher-Giguère C.-A., Cenci E., Liang L., Bernardini M., 2023, MNRAS, 525, 5388

Bassini L., Feldmann R., Gensior J., Faucher-Giguère C.-A., Cenci E., Moreno J., Bernardini M., Liang L., 2024, MNRAS, 532, L14

Behroozi P. S., Silk J., 2015, ApJ, 799, 32

Behroozi P. S., Conroy C., Wechsler R. H., 2010, ApJ, 717, 379

Behroozi P. S., Wechsler R. H., Conroy C., 2013, ApJ, 770, 57

Behroozi P., Wechsler R. H., Hearin A. P., Conroy C., 2019, MNRAS, 488, 3143

Beltz-Mohrmann G. D., Berlind A. A., 2021, ApJ, 921, 112

Bera A., Hassan S., Smith A., Cen R., Garaldi E., Kannan R., Vogelsberger M., 2023, ApJ, 959, 2

Bevins H. T., Handley W. J., Fialkov A., De Lera Acedo E., Greenhill L. J., Price D. C., 2021, MNRAS, 502, 4405

Bolan P. et al., 2021, MNRAS, 517, 3263

Borrow J., Kannan R., Garaldi E., Smith A., Vogelsberger M., Pakmor R., Springel V., Hernquist L., 2023, MNRAS, 525, 5932

Bouché N. et al., 2010, ApJ, 718, 1001

Bouwens R. J. et al., 2009, ApJ, 705, 936

Bouwens R. J. et al., 2012, ApJ, 752, L5

Bouwens R. J. et al., 2014, ApJ, 793, 115

Bouwens R. J. et al., 2015, ApJ, 803, 34

Bouwens R. J., Smit R., Labbé I., Franx M., Caruana J., Oesch P., Stefanon M., Rasappu N., 2016a, ApJ, 831, 176

Bouwens R. et al., 2016b, ApJ, 833, 72

Bouwens R. J., Oesch P. A., Illingworth G. D., Ellis R. S., Stefanon M., 2017, ApJ, 843, 129

Bouwens R. J., Illingworth G., Ellis R. S., Oesch P., Stefanon M., 2022, ApJ, 940, 55

Bouwens R., Illingworth G., Oesch P., Stefanon M., Naidu R., van Leeuwen I., Magee D., 2023a, MNRAS, 523, 1009

Bouwens R. J. et al., 2023b, MNRAS, 523, 1036

Bowman J. D., Rogers A. E. E., Monsalve R. A., Mozdzen T. J., Mahesh N., 2018, Nature, 555, 67

Boylan-Kolchin M., 2023, Nat. Astron., 7, 731

Boylan-Kolchin M., Bullock J. S., Garrison-Kimmel S., 2014, MNRAS, 443, L44

Boylan-Kolchin M., Weisz D. R., Johnson B. D., Bullock J. S., Conroy C., Fitts A., 2015, MNRAS, 453, 1503

Bradley R. F., Tauscher K., Rapetti D., Burns J. O., 2019, ApJ, 874, 153

Bruton S., Lin Y.-H., Scarlata C., Hayes M. J., 2023, ApJ, 949, L40

Bryan G. L., Norman M. L., 1998, ApJ, 495, 80

Camps P., Baes M., 2020, Astron. Comput., 31, 100381

Carnall A. C. et al., 2024, MNRAS, 534, 325

Carniani S. et al., 2024, Nature, 633, 318

Casey C. M. et al., 2024, ApJ, 965, 98

Castellano M., Belfiori D., Pentericci L., Calabrò A., Mascia S., Napolitano L., Caro F., 2023, A&A, 121, 1

Castellano M. et al., 2024, ApJ, 972, 143

Ceverino D., Klessen R. S., Glover S. C., 2019, MNRAS, 484, 1366

Ceverino D., Nakazato Y., Yoshida N., Klessen R., Glover S., 2024, A&A, 689, A244

Chabrier G., 2003, Publ. Astron. Soc. Pac., 115, 763

Chakraborty A., Choudhury T. R., 2024, JCAP, 2024, 078

Chan T. K., Kereš D., Wetzel A., Hopkins P. F., Faucher-Giguère C.-A., El-Badry K., Garrison-Kimmel S., Boylan-Kolchin M., 2018, MNRAS, 478, 906

Chemerynska I. et al., 2024, MNRAS, 531, 2615

Conselice C. J. et al., 2024, preprint (arXiv:2407.14973)

Cui W., Borgani S., Murante G., 2014, MNRAS, 441, 1769

Cullen F. et al., 2023, MNRAS, 520, 14

Curtis-Lake E. et al., 2023, Nat. Astron., 7, 622

Davé R., Finlator K., Oppenheimer B. D., 2012, MNRAS, 421, 98

Dayal P., 2019, Proc. Int. Astron. Union, 15, 43

Dayal P., Ferrara A., Dunlop J. S., Pacucci F., 2014, MNRAS, 445, 2545

Dayal P. et al., 2024, preprint (arXiv:2401.11242)

Deboer D. R. et al., 2017, Publ. Astron. Soc. Pacific, 129, 1

Dekel A., Sarkar K. C., Birnboim Y., Mandelker N., Li Z., 2023, MNRAS, 523, 3201

Donnan C. T. et al., 2023a, MNRAS, 518, 6011

Donnan C. T., McLeod D. J., McLure R. J., Dunlop J. S., Carnall A. C., Cullen F., Magee D., 2023b, MNRAS, 520, 4554

Donnan C. T. et al., 2024, MNRAS, 533, 3222

Draine B. T. et al., 2007, ApJ, 663, 866

Dwek E., 1998, ApJ, 501, 643

Eide M. B., Ciardi B., Graziani L., Busch P., Feng Y., Di Matteo T., 2020, MNRAS, 498, 6083

Eldridge J. J., Stanway E. R., 2009, MNRAS, 400, 1019

Endsley R., Stark D. P., Whitler L., Topping M. W., Chen Z., Plat A., Chisholm J., Charlot S., 2023, MNRAS, 524, 2312

Endsley R. et al., 2024, MNRAS, 533, 1111

Fan X., Carilli C. L., Keating B., 2006, Annu. Rev. Astron. Astrophys., 44, 415

Faucher-Giguère C.-A., 2018, Nat. Astron., 2, 368

Faucher-Giguère C.-A., Lidz A., Zaldarriaga M., Hernquist L., 2009, ApJ, 703, 1416

Faucher-Giguère C. A., Kereš D., Dijkstra M., Hernquist L., Zaldarriaga M., 2010, ApJ, 725, 633

Feldmann R., 2015, MNRAS, 449, 3274

Feldmann R., Gnedin N. Y., Kravtsov A. V., 2012, ApJ, 758, 127

Feldmann R., Quataert E., Hopkins P. F., Faucher-Giguère C.-A., Kereš D., 2017, MNRAS, 470, 1050

Feldmann R. et al., 2023, MNRAS, 522, 3831

Ferland G. J., Korista K. T., Verner D. A., Ferguson J. W., Kingdon J. B., Verner E. M., 1998, Publ. Astron. Soc. Pacific, 110, 761

Ferrara A., 2024, A&A, 684, 1

Ferrara A., Pallottini A., Dayal P., 2023, MNRAS, 522, 3986

Field G., 1958, Proc. IRE, 46, 240

Finkelstein S. L. et al., 2015, ApJ, 810, 71

Finkelstein S. L. et al., 2022, ApJ, 940, L55

Finkelstein S. L. et al., 2023, ApJ, 946, L13

Finkelstein S. L. et al., 2024, ApJ, 969, L2

Flores Velázquez J. A. et al., 2021, MNRAS, 501, 4812
Fudamoto Y. et al., 2020, A&A , 643, 1
Fujimoto S. et al., 2023, ApJ, 949, L25
Furlanetto S. R., Mirocha J., Mebane R. H., Sun G., 2017, MNRAS, 472, 1576
Gaikwad P. et al., 2023, MNRAS, 525, 4093
Gallerani S., Ferrara A., Fan X., Choudhury T. R., 2007, MNRAS, 386, 359
Garrison-Kimmel S. et al., 2019, MNRAS, 487, 1380
Gelli V., Mason C., Hayward C. C., 2024, ApJ, 975, 192
Gensior J., Feldmann R., Mayer L., Wetzel A., Hopkins P. F., Faucher-Giguère C. A., 2023, MNRAS., 518, L63
Ghara R., Mellema G., Giri S. K., Choudhury T. R., Datta K. K., Majumdar S., 2018, MNRAS, 476, 1741
Gill S. P. D., Knebe A., Gibson B. K., 2004, MNRAS, 351, 399
Glazebrook K. et al., 2024, Nature, 628, 277
Gnedin N. Y., 2000, ApJ, 535, 530
Gnedin N. Y., 2014, ApJ, 793, 1
Gnedin N. Y., Madau P., 2022, Living Rev. Comput. Astrophys., 8, 3
Gnedin N. Y., Tassis K., Kravtsov A. V., 2009, ApJ, 697, 55
Gorce A., Douspis M., Salvati L., 2022, A&A., 662, A122
Greig B., Mesinger A., Haiman Z., Simcoe R. A., 2017, MNRAS, 466, 4239
Greig B., Mesinger A., Davies F. B., Wang F., Yang J., Hennawi J. F., 2022, MNRAS, 512, 5390
Hahn O., Abel T., 2011, MNRAS, 415, 2101
Harikane Y. et al., 2016, ApJ, 821, 123
Harikane Y. et al., 2022, ApJS, 259, 20
Harikane Y. et al., 2023, ApJS, 265, 5
Harikane Y., Nakajima K., Ouchi M., Umeda H., Isobe Y., Ono Y., Xu Y., Zhang Y., 2024, ApJ, 960, 56
Hassan S. et al., 2023, ApJ, 958, L3
Hegde S., Wyatt M. M., Furlanetto S. R., 2024, J. Cosmol. Astropart. Phys., 2024, 025
Hills R., Kulkarni G., Meerburg P. D., Puchwein E., 2018, Nature, 564, E32
Hopkins P. F., 2015, MNRAS, 450, 53
Hopkins P. F., Keres D., Onorbe J., Faucher-Giguere C.-A., Quataert E., Murray N., Bullock J. S., 2014, MNRAS, 445, 581
Hopkins P. F. et al., 2018, MNRAS, 480, 800
Hsiao T. Y.-Y. et al., 2024, ApJ, 973, 8
Hunter J. D., 2007, Comput. Sci. Eng., 9, 90
Inayoshi K., Visbal E., Haiman Z., 2019, Annu. Rev. Astron. Astrophys., 58, 27
Inoue A. K., Shimizu I., Iwata I., Tanaka M., 2014, MNRAS, 442, 1805
Kannan R., Garaldi E., Smith A., Pakmor R., Springel V., Vogelsberger M., Hernquist L., 2022, MNRAS, 511, 4005
Kannan R. et al., 2023, MNRAS, 524, 2594
Katz N., Weinberg D. H., Hernquist L., 1996, ApJS, 105, 19
Katz H., Kimm T., Haehnelt M., Sijacki D., Rosdahl J., Blaizot J., 2018, MNRAS, 478, 4986
Katz H., Kimm T., Haehnelt M. G., Sijacki D., Rosdahl J., Blaizot J., 2019, MNRAS, 483, 1029
Kimm T., Cen R., 2014, ApJ, 788, 121
Knollmann S. R., Knebe A., 2009, ApJS, 182, 608
Koopmans L. et al., 2015, in Proc. Sci., Advancing Astrophysics with the Square Kilometre Array (AASKA14). Sissa, Trieste, PoS#001
Kravtsov A., Belokurov V., 2024, preprint (arXiv:2405.04578)
Kravtsov A. V., Berlind A. A., Wechsler R. H., Klypin A. A., Gottlober S., Allgood B., Primack J. R., 2004, ApJ, 609, 35
Krumholz M. R., Dekel A., 2012, ApJ, 753, 16
Krumholz M. R., Gnedin N. Y., 2011, ApJ, 729, 36
Kuhlen M., Faucher-Giguère C. A., 2012, MNRAS, 423, 862
Labbé I. et al., 2023, Nature, 616, 266
Leethochawalit N., Jones T. A., Ellis R. S., Stark D. P., Zitrin A., 2016, ApJ, 831, 152
Leroy A. K. et al., 2012, Flux, 99, 34
Lewis A., Challinor A., Lasenby A., 2000, ApJ, 538, 473
Lewis J. S. et al., 2020, MNRAS, 496, 4342
Lewis J. S. et al., 2022, MNRAS, 516, 3389
Li Q., Narayanan D., Davé R., 2019, MNRAS, 490, 1425
Li Z., Dekel A., Sarkar K. C., Aung H., Giavalisco M., Mandelker N., Tacchella S., 2024, A&A, 690, A108
Liang L., Feldmann R., Hayward C. C., Narayanan D., Çatmabacak O., Kereš D., Faucher-Giguère C.-A., Hopkins P. F., 2021, MNRAS, 502, 3210
Liang L. et al., 2024, MNRAS, 528, 499
Lilly S. J., Carollo C. M., Pipino A., Renzini A., Peng Y., 2013, ApJ, 772, 119
Lin Y.-h. et al., 2023, MNRAS, 527, 4173
Lovell C. C., Vijayan A. P., Thomas P. A., Wilkins S. M., Barnes D. J., Irodotou D., Roper W., 2020, MNRAS, 500, 2127
Lovell C. C., Harrison I., Harikane Y., Tacchella S., Wilkins S. M., 2023, MNRAS, 518, 2511
Ma X. et al., 2018, MNRAS, 478, 1694
Ma X. et al., 2019, MNRAS, 487, 1844
Ma X., Quataert E., Wetzel A., Hopkins P. F., Faucher-Giguère C. A., Kereš D., 2020, MNRAS, 498, 2001
Madau P., 2018, MNRAS, 480, L43
Madau P., Dickinson M., 2014, Annu. Rev. Astron. Astrophys., 52, 415
Madau P., Haardt F., Rees M. J., 1999, ApJ, 514, 648
Maity B., Choudhury T. R., 2022, MNRAS, 515, 617
Marszewski A., Sun G., Faucher-Giguère C.-A., Hayward C. C., Feldmann R., 2024, ApJ, 967, L41
Mascia S. et al., 2023, A&A, 672, A155
Mascia S. et al., 2024, A&A, 3, 1
Mason C. A., Trenti M., Treu T., 2015, ApJ, 813, 21
Mason C. A. et al., 2019, MNRAS, 485, 3947
Matthee J., Sobral D., Best P., Khostovan A. A., Oteo I., Bouwens R., Röttgering H., 2017, MNRAS, 465, 3637
McGreer I. D., Mesinger A., D'Odorico V., 2015, MNRAS, 447, 499
McLure R. J. et al., 2013, MNRAS, 432, 2696
Mellema G. et al., 2013, Exp. Astron., 36, 235
Mertens F. G. et al., 2020, MNRAS, 493, 1662
Meurer G. R., Heckman T. M., Calzetti D., 1999, ApJ, 521, 64
Mirocha J., Furlanetto S. R., 2023, MNRAS, 519, 843
Moster B. P., Naab T., White S. D. M., 2013, MNRAS, 428, 3121
Moster B. P., Naab T., White S. D. M., 2018, MNRAS, 477, 1822
Muñoz J. B., Qin Y., Mesinger A., Murray S. G., Greig B., Mason C., 2022, MNRAS, 511, 3657
Muñoz J. B., Mirocha J., Chisholm J., Furlanetto S. R., Mason C., 2024, MNRAS, 535, L37
Munshi S. et al., 2024, A&A, 687, 1
Murray S., 2014, Astrophysics Source Code Library, record ascl:1412.006
Murray S., Power C., Robotham A., 2013, Astron. Comput., 3–4, 23
Naidu R. P. et al., 2017, ApJ, 847, 12
Naidu R. P., Tacchella S., Mason C. A., Bose S., Oesch P. A., Conroy C., 2020, ApJ, 892, 109
Naidu R. P. et al., 2022, ApJ, 940, L14
Ocvirk P. et al., 2020, MNRAS, 496, 4087
Oesch P. A., Bouwens R. J., Illingworth G. D., Labbé I., Stefanon M., 2018, ApJ, 855, 105
Oke J. B., Gunn J. E., 1983, ApJ, 266, 713
Ouchi M. et al., 2010, ApJ, 723, 869
Pahl A. J., Shapley A., Steidel C. C., Chen Y., Reddy N. A., 2021, MNRAS, 505, 2447
Pallottini A., Ferrara A., 2023, A&A, 677, L4
Pandya V. et al., 2021, MNRAS, 508, 2979
Park J., Mesinger A., Greig B., Gillet N., 2019, MNRAS, 484, 933
Patil A. H. et al., 2017, ApJ, 838, 65
Peimbert A., Peimbert M., Luridiana V., 2016, Rev. Mex. Astron. Astrofis., 52, 419
Pérez-González P. G. et al., 2023, ApJ, 951, L1
Qin Y., Balu S., Wyithe J. S. B., 2023, MNRAS, 526, 1324
Rahmati A., Schaye J., Pawlik A. H., Raičevic M., 2013, MNRAS, 431, 2261
Reichardt C. L. et al., 2021, ApJ, 908, 199
Robertson B. E., 2022, Annu. Rev. Astron. Astrophys., 60, 121
Robertson B. E., Ellis R. S., Dunlop J. S., McLure R. J., Stark D. P., 2010, Nature, 468, 49
Robertson B. E. et al., 2013, ApJ, 768, 71

Robertson B. E., Ellis R. S., Furlanetto S. R., Dunlop J. S., 2015, ApJ, 802, L19

Robertson B. E. et al., 2023, Nat. Astron., 7, 611

Robertson B. et al., 2024, ApJ, 970, 31

Rodríguez-Puebla A., Behroozi P., Primack J., Klypin A., Lee C., Hellinger D., 2016, MNRAS, 462, 893

Rodríguez-Puebla A., Primack J. R., Avila-Reese V., Faber S. M., 2017, MNRAS, 470, 651

Rosdahl J. et al., 2018, MNRAS, 479, 994

Rosdahl J. et al., 2022, MNRAS, 515, 2386

Sabti N., Muñoz J. B., Blas D., 2022, Phys. Rev. D, 105, 043518

Saldana-Lopez A. et al., 2023, MNRAS, 522, 6295

Salpeter E. E., 1955, ApJ, 121, 161

Sawala T., Frenk C. S., Crain R. A., Jenkins A., Schaye J., Theuns T., Zavala J., 2013, MNRAS, 431, 1366

Schaeffer T., Giri S. K., Schneider A., 2023, MNRAS, 526, 2942

Schaller M. et al., 2015, MNRAS, 451, 1247

Schenker M. A., Ellis R. S., Konidaris N. P., Stark D. P., 2014, ApJ, 795, 20

Schroeder J., Mesinger A., Haiman Z., 2013, MNRAS, 428, 3058

Seeyave L. T. C. et al., 2023, MNRAS, 525, 2422

Shapley A. E., Steidel C. C., Strom A. L., Bogosavljević M., Reddy N. A., Siana B., Mostardi R. E., Rudie G. C., 2016, ApJ, 826, L24

Sharma M., Theuns T., Frenk C., Bower R., Crain R., Schaller M., Schaye J., 2016, MNRAS, 458, L94

Shen X., Vogelsberger M., Boylan-Kolchin M., Tacchella S., Kannan R., 2023a, MNRAS, 525, 3254

Shen X., Vogelsberger M., Boylan-Kolchin M., Tacchella S., Kannan R., 2023b, MNRAS, 525, 3254

Simmonds C. et al., 2023a, MNRAS, 523, 5468

Simmonds C. et al., 2023b, MNRAS, 527, 6139

Sims P. H., Pober J. C., 2020, MNRAS, 492, 22

Singh S., Subrahmanyan R., 2019, ApJ, 880, 26

Singh S. et al., 2022, Nat. Astron., 6, 607

Sipple J., Lidz A., 2024, ApJ, 961, 50

Smit R., Bouwens R. J., Franx M., Illingworth G. D., Labbé I., Oesch P. A., Van Dokkum P. G., 2012, ApJ, 756, 14

So G. C., Norman M. L., Reynolds D. R., Wise J. H., 2014, ApJ, 789 149

Sobacchi E., Mesinger A., 2015, MNRAS, 453, 1843

Song M. et al., 2016, ApJ, 825, 5

Springel V., 2005, MNRAS, 364, 1105

Springel V. et al., 2008, MNRAS, 391, 1685

Stanway E. R., Eldridge J. J., 2018, MNRAS, 479, 75

Stark D. P., 2016, Annu. Rev. Astron. Astrophys., 54, 761

Stark D. P., Schenker M. a., Ellis R., Robertson B., McLure R., Dunlop J., 2013, ApJ, 763, 129

Stefanon M., Bouwens R. J., Labbé I., Illingworth G. D., Gonzalez V., Oesch P. A., 2021, ApJ, 922, 29

Su K.-Y., Hopkins P. F., Hayward C. C., Faucher-Giguère C.-A., Kereš D., Ma X., Robles V. H., 2017, MNRAS, 471, 144

Sun G., Furlanetto S. R., 2016, MNRAS, 460, 417

Sun G., Faucher-Giguère C.-A., Hayward C. C., Shen X., 2023a, MNRAS, 526, 2665

Sun G., Mas-Ribas L., Chang T.-C., Furlanetto S. R., Mebane R. H., Gonzalez M. O., Parsons J., Trapp A. C., 2023b, ApJ, 950, 40

Sun G., Faucher-Giguère C.-A., Hayward C. C., Shen X., Wetzel A., Cochrane R. K., 2023c, ApJ, 955, L35

Tacchella S., Trenti M., Carollo C. M., 2013, ApJ, 768, L37

Tacchella S., Bose S., Conroy C., Eisenstein D. J., Johnson B. D., 2018, ApJ, 868, 92

Tacchella S. et al., 2023, ApJ, 952, 74

Tang M. et al., 2023, MNRAS, 526, 1657

Tinker J., Kravtsov A. V., Klypin A., Abazajian K., Warren M., Yepes G., Gottlöber S., Holz D. E., 2008, ApJ, 688, 709

Trenti M., Stiavelli M., Bouwens R. J., Oesch P., Shull J. M., Illingworth G. D., Bradley L. D., Carollo C. M., 2010, ApJ, 714, L202

Umeda H., Ouchi M., Nakajima K., Harikane Y., Ono Y., Xu Y., Isobe Y., Zhang Y., 2024, ApJ, 971, 124

Vale A., Ostriker J. P., 2004, MNRAS, 353, 189

Velliscig M., van Daalen M. P., Schaye J., McCarthy I. G., Cacciato M., Le Brun A. M., Vecchia C. D., 2014, MNRAS, 442, 2641

Verner D. A., Ferland G. J., 1996, ApJS, 103, 467

Villasenor B., Robertson B., Madau P., Schneider E., 2022, ApJ, 933, 59

Vogelsberger M. et al., 2020, MNRAS, 492, 5167

Wang Y.-Y., Lei L., Tang S.-P., Yuan G.-W., Fan Y.-Z., 2024, ApJ, 975, 285

Watson D., 2011, A&A, 533, A16

Weingartner J. C., Draine B. T., 2001, ApJ, 548, 296

Wetzel A. R., Hopkins P. F., Kim J.-h., Faucher-Giguère C.-A., Kereš D., Quataert E., 2016, ApJ, 827, L23

Wiersma R. P. C., Schaye J., Smith B. D., 2009, MNRAS, 393, 99

Wilkins S. M., Feng Y., Di-Matteo T., Croft R., Stanway E. R., Bouwens R. J., Thomas P., 2016, MNRAS, 458, L6

Wilkins S. M. et al., 2022, MNRAS, 519, 3118

Wise J. H., Demchenko V. G., Halicek M. T., Norman M. L., Turk M. J., Abel T., Smith B. D., 2014, MNRAS, 442, 2560

Wouthuysen S. A., 1952, AJ, 57, 31

Wu Z., Kravtsov A., 2024, The Open J. Astrophys., 7, 56

Yeh J. Y. et al., 2023, MNRAS, 520, 2757

Yung L. Y. A., Somerville R. S., Finkelstein S. L., Wilkins S. M., Gardner J. P., 2023, MNRAS, 527, 5929

Zackrisson E., Rydberg C. E., Schaerer D., Stlin G., Tuli M., 2011, ApJ, 740, 13

SUPPORTING INFORMATION

Supplementary data are available at *MNRAS* online.

UV_LF.txt

APPENDIX A: CALCULATION OF UV MAGNITUDES

As detailed in Section 2.2, this study uses two methods to determine the UV magnitudes of galaxies. The first method, which accounts for dust attenuation, involves running radiative transfer calculations with SKIRT and measuring fluxes within circular apertures centred on the respective galaxy. The resulting UV magnitude is thus in principle viewing-angle dependent. The second method, which is computationally cheaper and viewing angle-independent, ignores dust and calculates UV fluxes by summing contributions from all star particles within a given three-dimensional distance from the given galaxy. Fig. A1 compares the average difference in UV magnitude between the two methods for central galaxies residing in haloes of a given mass. As the figure demonstrates, the second method approximates the results of the full radiative transfer calculation in low-mass haloes, with a difference of less than 0.05 mag on average in haloes with masses below $\sim 3 \times 10^9\,\mathrm{M}_\odot$. The figure also shows that UV magnitudes are increasingly affected by dust absorption and scattering in more massive haloes, e.g. by ~ 0.2–0.3 mag on average in $\sim 3 \times 10^{10}\,\mathrm{M}_\odot$ haloes.

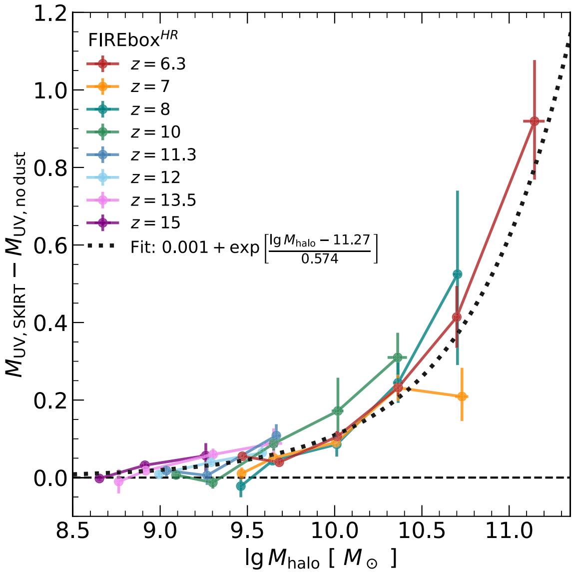

Figure A1. Dependence on halo mass of the average difference between the rest-frame UV magnitude obtained from a dust-radiative transfer computation with SKIRT and from a dust-free calculation obtained by adding the UV luminosities of all star particles in FIREbox^{HR} haloes. Error bars show confidence intervals (16th–84th percentiles) of the average difference obtained via bootstrapping. The dotted curve is the result of fitting an exponential function with variable offset to all shown data points and taking their uncertainties into account. The best-fitting parameters are provided in the legend. On average, the much faster, dust-free calculation is accurate to better than 0.05 mag for haloes with $M_{\rm halo} < 3 \times 10^9$ M$_\odot$. The importance of dust attenuation increases with halo mass but does not appear to strongly evolve with redshift over $z \sim 6$–15.

APPENDIX B: MASSES OF HALOES AND GALAXIES

Fig. B1 reports the average halo mass and the average stellar mass of FIREbox^{HR} galaxies in bins of their (dust-attenuated) UV magnitude at $z \sim 6$–15. On average, more UV luminous galaxies tend to have higher stellar masses and reside in more massive haloes, as expected. Both relations show a substantial scatter ($\sim$ 0.3–0.4 dex) that does not strongly depend on luminosity and redshift over $z = 6 - 8$. As a comparison, Song et al. (2016) report a scatter of 0.36, 0.40, 0.30 dex for $M_{\rm UV}$–$M_{\rm star}$ relation at $z = 6, 7, 8$ with no noticeable correlation of the scatter with redshift or UV luminosity.

Furthermore, the stellar and halo mass of galaxies of a given UV luminosity decreases with increasing redshift. The decrease in galaxy stellar mass with increasing redshift at fixed UV luminosity is consistent with observational findings (e.g. Stark et al. 2013; Song et al. 2016; Stefanon et al. 2021) and usually understood to reflect an evolution in the specific SFR. At $z > 10$, halo and stellar masses of UV faint galaxies with $M_{\rm UV} > -16$ decrease quickly with increasing redshift. We interpret this result as the lack of suppression of star formation in low-mass haloes during the pre-reionization era caused by the lack of a cosmic UV background.

The evolution of the average halo and stellar mass at fixed UV luminosity can be understood in the context of a non-evolving SFE–halo mass relation. A galaxy in a halo of any given mass will, on average, have a higher UV luminosity at a higher z because the specific halo growth rate increases with z at fixed mass (Behroozi & Silk 2015; Rodríguez-Puebla et al. 2016) and the UV luminosity is proportional to the halo growth rate and the SFE (equation 9). This observation combined with a comparably low and approximately mass and redshift independent scatter implies that the average halo mass hosting galaxies of a given UV luminosity will decrease with increasing redshift. Given that the stellar mass–halo mass

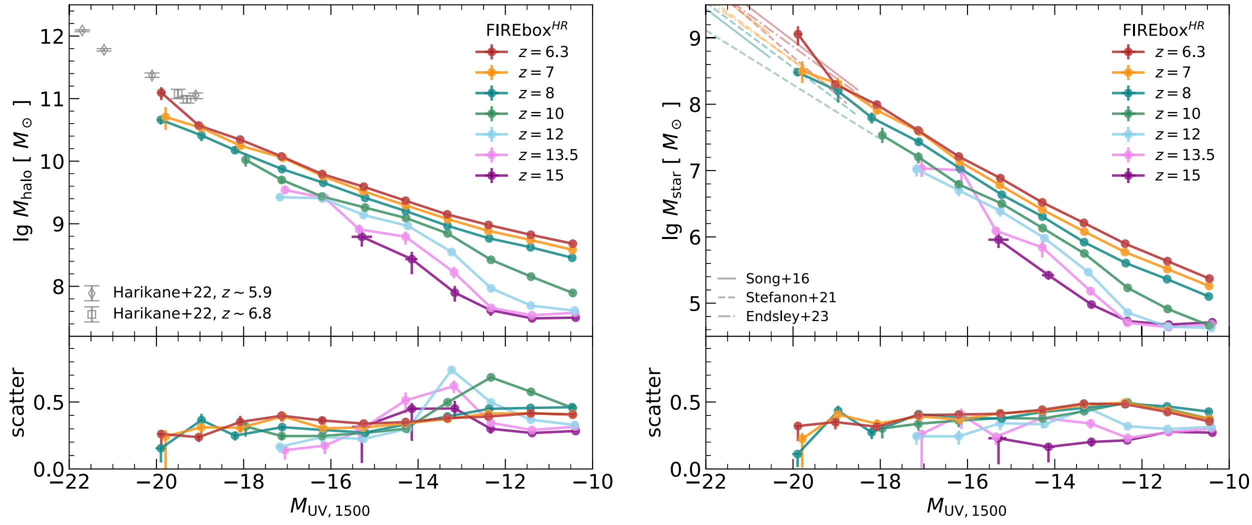

Figure B1. Halo mass (left panels) and stellar mass (right panels) in bins of UV magnitude for galaxies at $z \sim 6 - 15$ in FIREbox^{HR}. The larger panels at the top show the logarithm of the average mass in each UV magnitude bin while the smaller panels at the bottom show the corresponding scatter of the mass in dex. Filled symbols and thick lines show results for FIREbox^{HR} for different redshifts (see legend). Bins with less than 3 data points are not shown. The figure only includes haloes with at least 300 dark matter particles ($M_{\rm halo} \gtrsim 10^7$ M$_\odot$). UV magnitudes shown on the x-axis include the effects of dust attenuation. Uncertainties (16th–84th percentiles) are computed via bootstrapping. Empty squares and diamonds in the top left panel are observational estimates at $z \sim 6$–7 based on galaxy clustering by Harikane et al. (2022). Thin lines show the observed $M_{\rm UV}$–$M_{\rm star}$ relation at $z \sim 6$–10 (Song et al. 2016; Stefanon et al. 2021; Endsley et al. 2023a). The normalization of this relation is sensitive to the adopted star formation history (see e.g. Endsley et al. 2023a). On average, galaxies that are more UV luminous are more massive and reside in more massive haloes. Stellar and halo masses at fixed UV magnitude increase with decreasing redshift. The scatter ($\sim 0.3 - 0.4$ dex) in either relation is significant.

relation has low scatter and is approximately redshift independent at high z in FIRE-2 zoom-in simulation (Ma et al. 2018, 2019), the stellar mass will also decrease with increasing redshift at fixed UV magnitude.

APPENDIX C: SFE FOR DIFFERENT AVERAGING TIMES OF STAR FORMATION

Fig. C1 shows the SFE–halo mass relation for two alternative choices of the SFR averaging time (100 and 5 Myr). A longer averaging time of 100 Myr reduces the scatter of the relation but introduces a bias as many galaxies are growing quickly at high redshift and the SFRs are thus underestimated compared to those measured on shorter time-scales.

APPENDIX D: THE FAINT END SLOPE OF THE UV LF

Equation (16) expresses the UV LF in terms of the halo mass function (HMF) $\mathrm{d}n/\mathrm{d}M$ and the probability distribution $p(\mathcal{M}=m|M,z)$ of the UV magnitude $\mathcal{M}$ as function of halo mass M and redshift z. Following the discussion in Section 3.4, we model $p(\mathcal{M}=m|M,z)$ as a normal distribution with the mean $\langle\mathcal{M}\rangle$ and standard deviation $\sigma_{\mathcal{M}}$ given by equation (12). The UV LF can thus be written as

$$\phi(m,z)=\int_0^{\infty}\mathrm{d}M\,\frac{\mathrm{d}n}{\mathrm{d}M}\,\frac{1}{\sqrt{2\pi}\sigma_{\mathcal{M}}}\exp\left[-\frac{(\mathscr{M}+\frac{c}{2}\sigma_{\mathcal{M}}^2-m)^2}{2\sigma_{\mathcal{M}}^2}\right], \tag{D1}$$

with $\mathscr{M}=\mathrm{Mag}(\langle\mathcal{S}\rangle\dot{M}/\kappa)$ and $c=\ln(10)/2.5$.

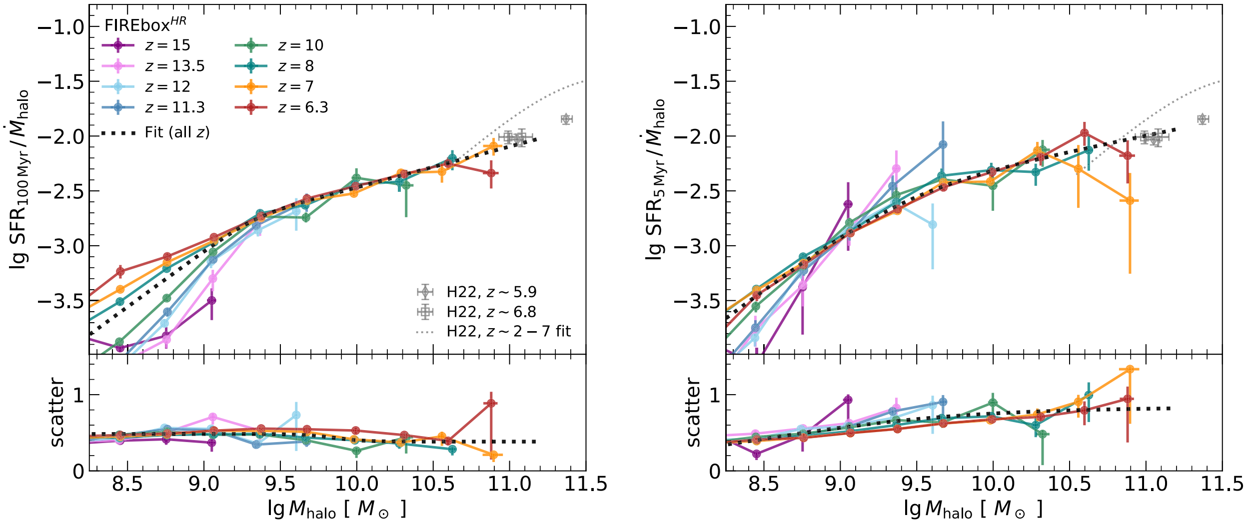

Figure C1. Same as the bottom left panel in Fig. 4 except for different SFR averaging times: 100 Myr (left panel) and 5 Myr (right panel).

We can solve equation (D1) analytically if the halo mass function, the SFE, and the halo growth rate are all power-law functions of the halo mass, and $\sigma_{\mathcal{M}}$ is a constant, i.e. if

$$\frac{\mathrm{d}n}{\mathrm{d}M} = \left(\frac{\mathrm{d}n}{\mathrm{d}M}\right)_0 \tilde{M}^{\alpha_M}, \langle\mathcal{S}\rangle = \langle\mathcal{S}\rangle_0 \tilde{M}^{\beta}, \dot{M} = \dot{M}_0 \tilde{M}^{\gamma}, \tag{D2}$$

where $\tilde{M} = M/M_0$, M_0 is a chosen reference halo mass, and prefactors with the subscript 0 do not depend on halo mass but potentially on other quantities such as redshift. Inserting equation (D2) into equation (D1) and integrating over M results in

$$\phi(m, z) = c\phi_* 10^{-0.4(1+\alpha)(m-m_*)}, \tag{D3}$$

with

$$\alpha = \frac{1+\alpha_M}{\beta+\gamma} - 1 \tag{D4}$$

$$m_* = \mathrm{Mag}(\langle\mathcal{S}\rangle_0 \dot{M}_0/\kappa) \tag{D5}$$

$$\phi_* = \left(\frac{\mathrm{d}n}{\mathrm{d}M}\right)_0 M_0 \frac{1}{\beta+\gamma} \exp\left(\frac{c^2}{2}(1+\alpha)(2+\alpha)\sigma_{\mathcal{M}}^2\right). \tag{D6}$$

According to equation (D3), the UV LF is then a power law with respect to UV luminosities. Moreover, since equation (D3) has the same functional form as the faint magnitude limit of a traditional Schechter or double power law function, we can identify the following parameters: α represents the faint-end slope, m_* corresponds to the characteristic magnitude, and ϕ_* is the normalization of the LF. Due to the scale-free nature of a power law, either m_* or ϕ_* (but not both independently) can be freely adjusted by selecting an appropriate value for M_0. Multiplying the normalization $\langle\mathcal{S}\rangle_0$ of the SFE–halo mass relation by a factor f increases m_* by $-2.5\lg f$, i.e. it amounts to a horizontal shift by this amount. Alternatively, such a shift may be interpreted as a vertical increase of $\lg\phi$ by $-(1+\alpha)\lg f$. Equation (D4) shows that the faint-end slope α of the UV LF is directly related to the combination of α_M and $\beta+\gamma$. Provided the scatter σ_M is mass independent as assumed in the derivation above or small enough to be ignored, we can directly infer the low-mass slope of the SFE–halo mass relation (denoted by β here and by α_1 in the main text) from measurements of the faint-end slope of the UV LF for a given cosmological model with well constrained α_M and γ. Alternatively, if β can be measured independently by other means, the faint end of the UV LF may be used to constrain the growth properties of haloes (α_M and γ) and perhaps even test alternative dark matter models.

The faint-end slope also determines how a larger scatter in the SFE, given by std(lg $\mathcal{S}$) = $\sigma_{\mathcal{M}}/2.5$, affects the normalization of the faint end of the UV LF. According to equation (D6), an increase in the scatter of the SFE will raise the normalization of the UV LF when $\alpha < -2$ or $\alpha > -1$ and decrease ϕ_* when $-2 < \alpha < -1$. These considerations clarify how the UV LFs shown in the right panel of Fig. 7 are affected by the scatter in the SFE. At sufficiently faint magnitudes, a power-law approximation of the UV LF results in a slope α that is shallower than -2 because of the modest turn-over at faint magnitudes seen in FIREbox^{HR}. As a result, a larger scatter reduces the UV LF at the faintest magnitudes. In contrast, at brighter UV magnitudes, the UV LF has a local slope steeper than -2, leading to an increase in number density with increasing scatter. The scatter has little impact on the UV LF when the local slope is near -2. This condition is met around $M_{\mathrm{UV}} \sim -18$ at $z = 6$, and $M_{\mathrm{UV}} \sim -15$ at $z = 14$ for the model with a fixed scatter of 0.4 dex shown in Fig. 7. This result explains why the UV luminosity density integrated down to $M_{\mathrm{UV}} = -17$ is only weakly dependent on the scatter of the SFE as shown in the left panel of Fig. 9.

APPENDIX E: FITTING PARAMETERS FOR THE UV LFS

Table E1 presents the parameters derived from fitting a modified Schechter function (as described in Bouwens et al. 2017) to the UV LFs predicted by the theoretical model of Section 3.4 and shown in Fig. 8. Additionally, Table E2 displays the parameters obtained when employing a double power law to fit the UV LFs (e.g. Harikane et al. 2022). The scatter in the SFE–halo mass relation is modelled in two ways: its mass dependence is either inferred directly from FIREbox^{HR} (denoted as ‘fiducial’) or it is assumed to be a constant value between 0.2 and 0.6 dex. All fits were performed using the SCIPY.OPTIMIZE.CURVE_FIT routine in PYTHON, spanning UV magnitudes from -21.5 to -13 with a uniform spacing of 0.36 mag. The double power law generally provides as superior fit to the UV LFs of the theoretical model (see Section 3.5).

Table E1. Parameters derived from fitting a modified Schechter function to the UV LF predicted by the theoretical model for a non-evolving SFE–halo mass relation with different choices of the scatter. Columns 1–5 list the redshift z, the characteristic UV magnitude M_{UV}^{*}, the common logarithm of the LF normalization ϕ^{*} in units of $\mathrm{mag}^{-1}\,\mathrm{cMpc}^{-3}$, the faint-end slope α, and the roll-over parameter δ of the modified Schechter function parametrization. The roll-over parameter equals zero for the traditional Schechter function. The final column provides the UV magnitude $M_{\mathrm{UV,T}}$ at which the LF is expected to reach its maximum based on the modified Schechter parametrization. The theoretical model predicts a decrease in α (steepening) with increasing redshift and a slight deviation from a traditional Schechter function at the faintest magnitudes.

z	M_{UV}^{*}	$\lg\phi^{*}$	α	δ	$M_{\mathrm{UV,T}}$
Mass-dependent scatter (fiducial)					
6	−20.52	−3.17	−1.95	0.17	−13.24
8	−20.11	−3.36	−1.99	0.16	−12.90
10	−19.82	−3.74	−2.04	0.14	−12.28
12	−19.63	−4.27	−2.09	0.11	−11.24
14	−19.59	−4.98	−2.16	0.09	−9.79
16	−19.71	−5.91	−2.27	0.09	−8.61
18	−19.91	−7.01	−2.40	0.09	−7.99
20	−20.13	−8.21	−2.54	0.09	−7.61
Constant scatter (0.2 dex)					
6	−20.54	−3.23	−1.98	0.14	−12.39
8	−20.20	−3.53	−2.08	0.15	−12.41
10	−19.96	−4.04	−2.20	0.16	−12.29
12	−19.78	−4.72	−2.33	0.17	−12.12
14	−19.43	−5.32	−2.42	0.15	−11.40
16	−19.33	−6.25	−2.59	0.16	−11.15
18	−19.05	−7.09	−2.71	0.15	−10.21
20	−18.81	−8.03	−2.84	0.13	−9.14
Constant scatter (0.4 dex)					
6	−20.73	−3.26	−1.93	0.12	−11.97
8	−20.48	−3.58	−2.01	0.12	−11.90
10	−20.32	−4.10	−2.11	0.13	−11.66
12	−20.22	−4.79	−2.23	0.13	−11.36
14	−20.16	−5.62	−2.35	0.14	−11.02
16	−20.13	−6.57	−2.50	0.14	−10.68
18	−20.11	−7.64	−2.65	0.15	−10.35
20	−19.88	−8.59	−2.76	0.13	−9.34
Constant scatter (0.6 dex)					
6	−20.99	−3.32	−1.88	0.09	−11.27
8	−20.83	−3.65	−1.94	0.10	−11.07
10	−20.75	−4.18	−2.02	0.10	−10.68
12	−20.71	−4.86	−2.12	0.10	−10.21
14	−20.71	−5.67	−2.22	0.10	−9.71
16	−20.71	−6.59	−2.34	0.10	−9.20
18	−20.73	−7.61	−2.46	0.10	−8.70
20	−20.74	−8.71	−2.59	0.10	−8.23

Table E2. Parameters derived from fitting a double power law function to the UV LF predicted by the theoretical model for a non-evolving SFE–halo mass relation with different choices of the scatter. Columns 1–5 list the redshift z, the characteristic UV magnitude $M^*_{\rm UV}$, the common logarithm of the LF normalization ϕ^* in units of mag^{-1} cMpc^{-3}, the faint-end slope α, and the bright-end slope β. The theoretical model predicts a decrease (i.e. steepening) of both the faint-end and the bright-end slope of the UV LFs with increasing redshift.

z	$M^*_{\rm UV}$	$\lg \phi^*$	α	β
Mass-dependent scatter (fiducial)				
6	−17.25	−1.55	−1.42	−2.61
8	−17.86	−2.11	−1.56	−2.99
10	−18.29	−2.81	−1.71	−3.41
12	−18.63	−3.62	−1.86	−3.82
14	−18.88	−4.52	−2.00	−4.09
16	−18.98	−5.42	−2.13	−4.08
18	−18.97	−6.33	−2.25	−3.94
20	−18.86	−7.24	−2.36	−3.81
Constant scatter (0.2 dex)				
6	−17.75	−1.80	−1.59	−2.69
8	−18.00	−2.26	−1.70	−3.04
10	−18.14	−2.86	−1.82	−3.38
12	−18.23	−3.58	−1.96	−3.72
14	−18.11	−4.31	−2.09	−3.90
16	−18.12	−5.23	−2.25	−4.19
18	−17.93	−6.09	−2.39	−4.28
20	−17.70	−7.00	−2.53	−4.35
Constant scatter (0.4 dex)				
6	−17.79	−1.84	−1.58	−2.57
8	−18.02	−2.27	−1.68	−2.81
10	−18.15	−2.83	−1.78	−3.02
12	−18.21	−3.50	−1.90	−3.22
14	−18.23	−4.27	−2.03	−3.39
16	−18.22	−5.13	−2.16	−3.56
18	−18.20	−6.08	−2.31	−3.72
20	−17.97	−6.95	−2.43	−3.78
Constant scatter (0.6 dex)				
6	−17.87	−1.91	−1.58	−2.43
8	−18.07	−2.30	−1.65	−2.58
10	−18.17	−2.82	−1.74	−2.71
12	−18.21	−3.45	−1.84	−2.83
14	−18.22	−4.16	−1.95	−2.93
16	−18.19	−4.94	−2.06	−3.04
18	−18.14	−5.80	−2.17	−3.15
20	−18.08	−6.71	−2.29	−3.26

This paper has been typeset from a TEX/LATEX file prepared by the author.